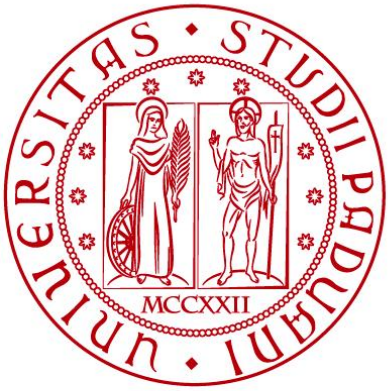

UNIVERSITÀ
DEGLI STUDI
DI PADOVA

Università degli Studi di Padova

DIPARTIMENTO DI INGEGNERIA INDUSTRIALE DII

Corso di Laurea in Ingegneria Aerospaziale

Electromagnetic full-wave analysis of radio-frequency antennas for magnetized plasma sources

Relatore:
Chia.mo Prof. Daniele Pavarin

Correlatori:
Chia.mo Prof. Vito Lancellotti
Dott. Davide Melazzi

Laureando:
Michele Fadone
Matricola 1084011

Anno Accademico 2015–2016

CONTENTS

LIST OF FIGURES

ABSTRACT

Helicon Plasma Thrusters are electric propulsion systems in which the plasma is ionised and heated by a radio frequency antenna and then it is exhausted through a divergent magnetic nozzle. The first part of these devices is composed by the Helicon Plasma Source, which is composed of a feeding system, a plasma cylinder, a Radio Frequency antenna and a magnetic coil.

In this thesis, we continue the study on this problem with the same approach proposed through the ADAMANT code, a solver based on a system of coupled surface and volume integral equations. The differences with the previous approaches consist of considering a 2D geometry antenna instead of a thin-wire one and of setting the antenna current density as an unknown variable of the electromagnetic and not as an input.

To compare these analysis techniques, it is necessary to transfer the problem into the spectral domain: an algorithm to determine this variable from the 2D antenna current density distribution, available among ADAMANT outputs, was developed.

We have analysed the spectral functions of the antenna current density, available for the Single-Loop, Nagoya III and Fractional Helix antennas[24]. Considerations about the influence of the discharge parameters have been made: the electron temperature and the background pressure do not affect the spectrum, whilst the magnetic field intensity and the plasma density cause little variations. A direct confront of the spectrum with those used for the previous approach showed that for the Single-Loop and the Nagoya III antennas there are huge differences whilst for the Fractional Helix the functions are really similar.

Successively, the radial power profiles of deposition into the plasma cylinder for a set of azimuthal and axial wave numbers were obtained through SPIREs, a Finite-Difference Frequency-Domain electromagnetic solver. The plots showed how the most influencing parameter is the azimuthal wave-number, followed by the axial one and the spectral intensity.

Finally, trying to optimize the antenna current density spectrum, two new antenna configurations have been analysed, first with ADAMANT and then with SPIREs. For the first one, which is a geometrical attempt, the power deposited into the plasma is comparable with the ones related to the other antenna configurations; moreover, the spectrum shows contribution for $m = 0$ and $m = \pm 1$. As for the second one, the study is done on the influence of the excitation phase of two separated loops. High power deposited values are guaranteed for the whole plasma density range considered according to the phase. In addition, the phase makes the spectral function shift along the axial wave-number axis, optimizing the spectral values analysed in the operative interval.

ABSTRACT ITALIANO

Gli Helicon Plasma Thrusters sono dei propulsori elettrici nei quali il plasma viene ionizzato e riscaldato da una antenna in radio frequenza, per poi essere scaricato per mezzo di un ugello magnetico divergente. La prima parte di questi dispositivi è composta dalla sorgente di plasma Helicon che è definita da sistema di rifornimento, da un cilindro di plasma, da una antenna in radio frequenza e da una bobina.

In questa tesi, si continua lo studio di questo problema con lo stesso approccio proposto attraverso il codice ADAMANT, un risolutore basato su un sistema di equazioni integrali di superficie e di volume. Le differenze con il vecchio metodo consistono nel considerare una geometria 2D dell'antenna invece che una sottile e nel porre la densità di corrente dell'antenna come incognita del problema elettromagnetico e non come input.

Per confrontare questi approcci, è necessario trasferire il problema nel dominio spettrale: è stato sviluppato un algoritmo per ricavare lo spettro della distribuzione 2D della densità di corrente, accessibile tra gli output di ADAMANT.

Abbiamo analizzato le funzioni spettrali di densità di corrente già disponibili per le antenne Single-Loop, Nagoya III e Fractional Helix. Sono state fatte delle considerazioni riguardo all'effetto dei parametri di scarica: la temperatura elettronica e la pressione non influenzano lo spettro, mentre l'intensità del campo magnetico e la densità del plasma causano leggere variazioni. Un confronto diretto dello spettro con quello utilizzato dal vecchio metodo dimostra che per la Single-Loop e la Nagoya III ci sono evidenti differenze mentre per la Fractional Helix le funzioni sono molto simili.

Successivamente, i profili radiali di deposizione di potenza nel cilindro di plasma sono stati ottenuti per certi valori di numeri d'onda azimutali e assiali attraverso SPIREs, un risolutore alla differenze finite nel campo delle frequenze. I grafici mostrano come il parametro più influente sia il numero d'onda azimutale, seguito da quello assiale e dall'intensità dello spettro.

Infine, provando ad ottimizzare lo spettro della densità di corrente di una antenna, due nuove configurazioni sono state analizzate, prima attraverso ADAMANT e poi con SPIREs. Per la prima antenna, che consiste in un tentativo più geometrico, la potenza assorbita dal plasma è comparabile con quella ottenuta per le altre antenne; inoltre, lo spettro evidenzia contributi sia per $m = 0$ che $m = \pm 1$. Per la seconda antenna, lo studio riguarda l'influenza dello sfasamento nell'eccitazione fra due loop separati. Elevati valori di potenza assorbita dal plasma sono stati registrati per tutto il range di densità di plasma considerato potendo variare la fase. Inoltre, la fase fa traslare lo spettro lungo l'asse del numero d'onda assiale, ottimizzando così i valori spettrali analizzati nell'intervallo operativo di interesse.

LIST OF ACRONYMS

ECR	Electron Cyclotron Resonance
FDFD	Finite-Difference Frequency-Domain
H	Helicon
HDLT	Helicon Double Layer Thruster
HPHCOM	Helicon Plasma Hydrazine COmbined Micro
HPS	Helicon Plasma Source
HPT	Helicon Plasma Thruster
ODE	Ordinary Differential Equation
RIE	Reactive Ion Etching
RF	Radio Frequency
RFI	Radio-Frequency Inductive
RWG	Rao-Wilton-Glisson
SIE	Surface Integral Equation
TCP	Transformer Coupled Plasma
TE	Transverse Electric
TF	Fourier Transform
TG	Trivelpiece-Gould
TM	Transverse Magnetic
VASIMR	VAriable Specific Impulse Magnetoplasma Rocket
VIE	Volume Integral Equation

1 INTRODUCTION

1.1 STATE OF ART OF HELICON PLASMA THRUSTERS

The Helicon Plasma Thruster (HPT) is an electromagnetic propulsion device whose technology is based on Helicon Plasma Source (HPS) know-how: the efficiency and the optimization obtained in the industrial material processes are not observed in the space propulsion field due to spatial restriction requirements [1] and this is why it is still under development.

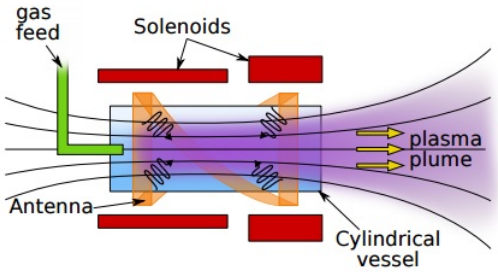

Figure 1.1: HPT operating principle. The gas is injected through a cylinder surrounded by an antenna and a system of solenoids: the former generates and heats the plasma while the latter confines it. At the end of the cylinder, there is the plasma exhaust flow which can be accelerated through a magnetic nozzle in order to obtain thrust.

In Fig.1.1, it is possible to understand the general composition of a HPT:

- a feeding system which comprehends a gas tank and a pressure injector;
- a plasma cylinder;
- a Radio Frequency (RF) Antenna;
- a magnetic coil;
- an electromagnetic divergent nozzle.

The feeding system injects a neutral gas into a dielectric cylindrical system where plasma is produced. The RF antenna, which surrounds the flow, emits in the MHz range and the absorption of the generated waves is the responsible of the plasma formation. Thanks to the magnetic coils, a quasi-axial magnetic field is imposed on the system, confining the plasma and guaranteeing the wave propagation. In closing, the magnetic nozzle expands the gas which acquires a certain velocity, therefore an acceleration and, consequently, a thrust.

HPT prototypes are usually divided according to the magnetic circuit they use and the power range in which they operate. Among those which use electromagnets, there is the Helicon Double Layer Thruster (HDLT) developed by

the Australian National University. It works in the low-to-mid power range, 200-800W, with a magnetic strength of 10-20mT and the Radio-Frequency antenna emits at the frequency of 13.25MHz. The thrust efficiency of this device is not higher than 3%, due to the low utilization efficiency η_u =25-35%, which means that only a small amount of neutral gas is ionized. Direct measurements of thrust suggests that the HDLT delivers up to 6mN of thrust and 800s of specific impulse using argon as a propellant.

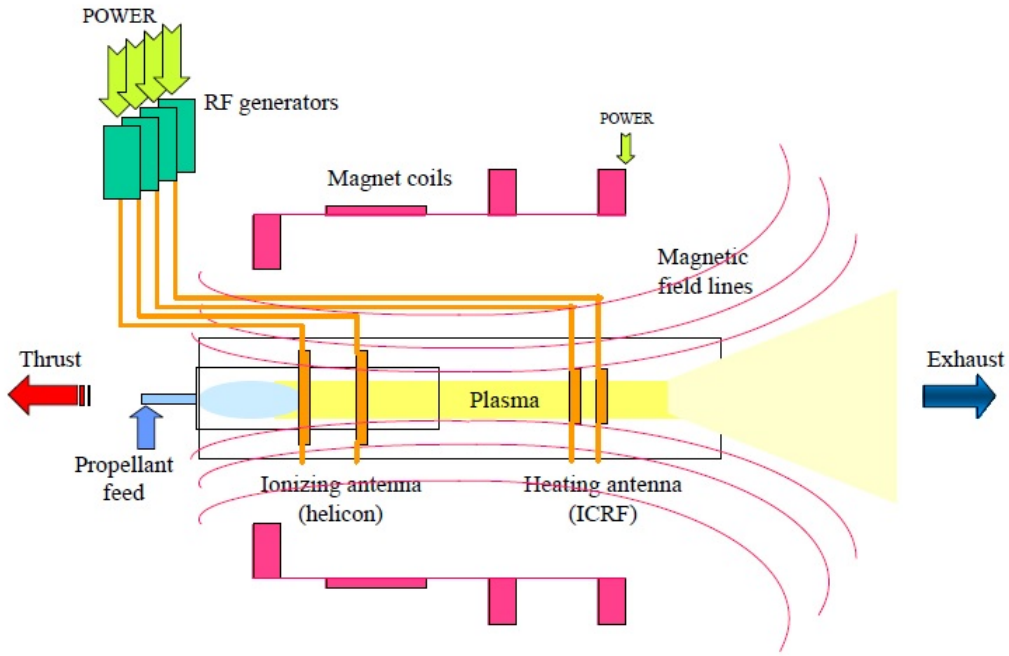

Figure 1.2: VASIMR: in the first part of the device there is the HPS stage where the plasma is generated. At the end of the cylinder the ICRF energies the plasma in order to gain the maximum thrust possible in the final magnetic nozzle [2].

Another prototype is the VAriable Specific Impulse Magnetoplasma Rocket (VASIMR), developed and patented by the Ad Astra Rocket Co. This device has an additional stage compared to a normal HPT: the Ion Cyclotron Resonance Heating system energizes the plasma which is finally accelerated along a magnetic nozzle, producing thrust. The complete engine presents a nominal power of 200kW, reaching a thrust efficiency over 50%, providing a thrust higher than 3N and specific impulses above 3000s. The disadvantage of this engine is the necessity of having ionized ions, so large magnetic fields, with its negative consequences, or light propellants are required: the magnetic field strength in the HPS stage is below 170mT, and provides 0.5N of thrust and 1600s of specific impulse, coupling up to 28kW of RF power to the plasma. The plasma ejected by the HPS is almost full ionized, with a propellant efficiency of 95%.

Finally, among the devices which use a permanent magnets, there is the Helicon Plasma Hydrazine COmbined Micro (HPHCOM)[3], funded by the European 7^{th} FrameWork Program and shown in Fig.1.3. The thruster class is 1.5 mN-50W, with a target specific impulse of 1200s employing Argon as propel-

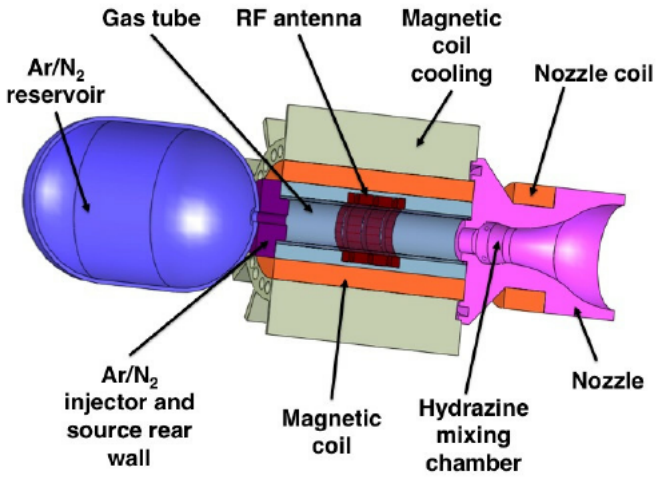

Figure 1.3: Helicon Plasma Hydrazine combined micro. It is composed of a gas tank followed by an injection system. The plasma stage is determined by a cylinder, an antenna and a magnetic coil system. Before the magnetic nozzle, a Hydrazine mixing chamber is situated in order to guarantee the two mode operations: low thrust-high efficiency and high thrust-low efficiency.

lant [4]. Compared to the other prototypes, in HPHCOM there is the possibility to activate two operation modes thanks to the Hydrazine mixing chamber: if in the magnetic nozzle only the plasma is accelerated, then the high efficiency-low thrust is on; if the mixing chamber is used, a low efficiency-high thrust mode is available.

The design of this particular device presented similar problems to those faced for sources applied in industrial applications: the main difference, though, is to maximize high specific impulses, which are influenced by the ionization efficiency and electron temperature, always remembering that a low electric power is available [5]. With the reminder that in a propulsion system a HPT can be thought as composed by a plasma source stage and an acceleration one, the design of HPHCOM was done knowing that energy deposited in the plasma is caused by the propagation of two coupled waves, the Helicon and the Trivelpiec-Gould. Thanks to analysis realized by D. Pavarin *et al.*[5], it was possible to understand the best combination of parameters to let the plasma absorb these waves. However, the important aspect still not fully fathomed is the dynamics of plasma acceleration at the exit section of a HPT: one conclusion obtained through an in-house code, the 3D Particle-in-Cell F3MPIC, was that the efficiency rises as the electron temperature rises.

1.2 HELICON PLASMA SOURCE OVERVIEW

The Helicon Plasma Source (HPS) is the stage in which the plasma production takes place. By definition, its components are the same for the HPT except for the magnetic nozzle. In Fig.1.4, there is an example of an experimental apparatus used to compare the results with other plasma production techniques.

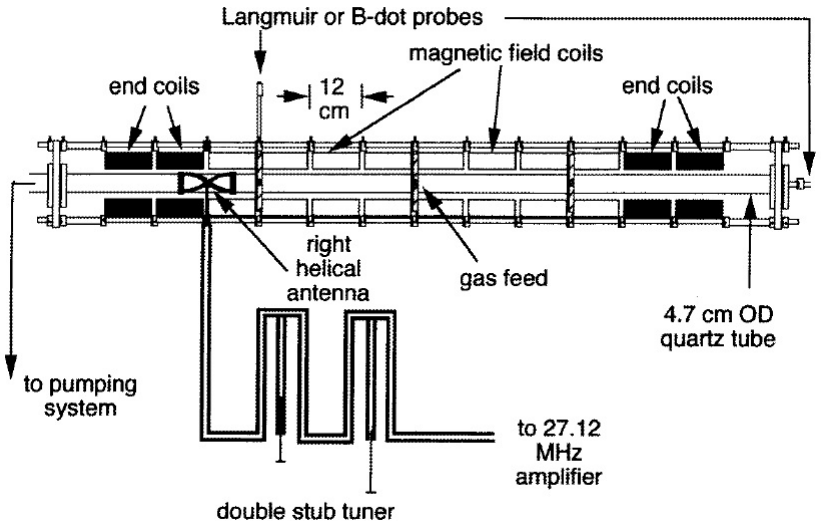

Figure 1.4: A schematic diagram of a helicon plasma source experimental apparatus. It is possible to see the four components: the gas feed system, the antenna, the plasma cylinder and the magnetic coils.

Generally, a helicon source consists of a dielectric tube surrounded by coils which generate a weak magnetostatic field (up to 0.15 T) and an RF antenna working in the range of frequencies $\omega_{ci} \ll w_{lh} \ll w \ll \omega_{ce}$, where $\omega_{ci}(\omega_{ci})$ is the ion(electron) cyclotron angular frequency, and w_{lh} is the lower-hybrid frequency.

Helicon plasma sources were first investigated by Boswell, who found that the absorption of radio-frequency energy by the plasma could not be explained by only collisional theory since there was a huge discrepancy between analytical and experimental results [6]. The mechanism behind the plasma production is always the same: giving energy to a neutral gas in order to create the formation of charge carriers. It is possible to understand that the ways to maximize the efficiency of this process are still under analysis. F. F. Chen *et al.* in 1995[7] figured out that Landau damping could play an important role in the plasma formation: they added, therefore, a collisionless mechanism since the charged particles are accelerated or damped according to the narrowness with the phase velocity with the exciting wave. Varying the operative parameters, such as magnetic field intensity or background pressure, it was still unknown the behaviour of the results obtained by the helicon sources: D. Arnush in 2000[8] underlined the role of Trivelpiece-Gould (TG) waves coupled with helicon (H) ones. An important characteristic about this coupling is that the former waves have a short radial wavelength compared to the latter ones: TG waves damp really fast and deposit their energy in the near edge of the plasma cylinder, whilst H waves penetrate until its center. As for the other mechanism of energy deposition, the two main parameters which control the efficiency of this process are, as already written, the magnetic field intensity and the background pressure.

Although everything was not so clear about the physics in HPS, the interest toward this new technology was caused by the advantages in confront to the previous plasma production systems, such as Reactive Ion Etching (RIE)

discharge, Electron Cyclotron Resonance (ECR) source, the Radio-frequency Inductive (RFI) or Transformer Coupled Plasma (TCP) discharge [9]:

- *High density*: using general gases or higher powers than normally used, there is a gain in density of a factor 10; if Argon with a 2 KW of rf power is considered, there is a gain of two orders of magnitude.
- *High efficiency*: thanks to the high densities obtained through the previous mechanism mentioned, there is a rapid transfer of wave energy to the primary electrons.
- *No internal electrodes*: since the antenna is outside the vacuum chamber, the possibility of contamination or sputtering from the electrodes producing the plasma is eliminated.
- *Low pressure operation*: in etching applications, it is possible to operate in low pressure field since the efficiency of plasma production does not depend uniquely by the collisional mechanism.

1.3 PREVIOUS APPROACHES AND A NEW PROPOSAL

With the interest about helicon sources, a grow push was made for the developing of plasma codes in order to simulate the coupling between the antenna and the gas.

The most recent algorithms which deal this electromagnetic problem are the Mouzoris and Scharer's ANTENA2[10], the Chen and Arnush's HELIC[11][12] and Melazzi *et al.*'s SPIREs (plaSma Padova Inhomogeneous Radial Electromagnetic solver)[13]. The first one is a modified version of ANTENA[14][15]: the

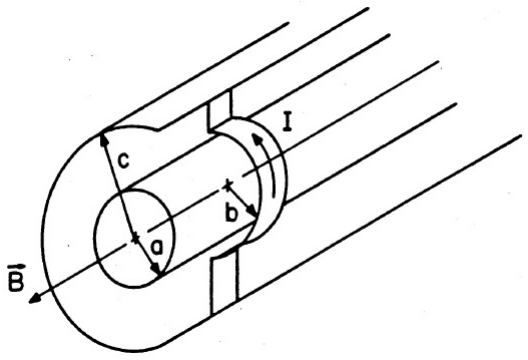

Figure 1.5: A schematic representation of the problem faced by ANTENA. a is the plasma radius, b is the inside radius of coil and c is the vacuum tank radius.

original one consists of a procedure in which the induction theorem helps to substitute the antenna and the coils with sinusoidal current sheets.

In this way, it is possible to reduce the three dimensional antenna boundary problem to that of one dimension, the radial one, with the spatial variation in the other directions expressed through complex exponentials $e^{im\phi+ik_z z}$: it must be remembered that the code considers the apparatus as the one shown

in Fig.1.5, a cylindrical hot magnetized plasma surrounded by an RF inductive coil, both enclosed in a metal conducting tube. In addition, the radial variation of the plasma parameters are approximated by a stratified model and the plasma response is characterised by the plasma equivalent dielectric tensor[16].

With ANTENA2, the vacuum electromagnetic fields in the cylindrical tube are still expanded into waveguide modes that are transverse electric(TE) and transverse magnetic(TM); the modification consists in the adaptation of the code for helical coils, since the previous version deals only with simple geometries.

All in all, both calculate the vacuum fields as well as the linear, inductive, self-consistent 3D electromagnetic fields, giving radial power deposition profiles, radial power flow and antenna impedance as response.

On the other hand, through HELIC it is possible to reduce Maxwell's equations, with the divergence constraints, to a fourth-order ordinary differential equation (ODE) for any field component, dealing separately the helicon and Trivelpiece-Gould dispersion modes.

However, these codes present singularity issues; therefore, SPIREs was developed. It is a Finite-Difference Frequency-Domain (FDFD) electromagnetic solver, using a Yee mesh along the radial direction of the cylinder in order to reduce computational time.

All this types of approach share common hypothesis and simplifications. First of all, Fourier transforms are applied to the Maxwell's equation in order to reduce them to a coupled set of ordinary differential relations simplifying, thereby, the electromagnetic problem. Secondly, the assumption of a thin-wire antenna helps considering the antenna current density as dependant only by the azimuthal and axial coordinates. Thirdly, the antenna current is imposed to the problem: although it is useful to analyse the plasma response, it does not allow to study the mutual interaction between plasma and antenna.

Finally, all these works dug up an important observation: remembering that TF introduces m and k_z excitation modes as variables in the equations, it was possible to notice that $m = 0$ or $m = \pm 1$ modes were the main factors of the power deposition, since the other modes excite the waves lesser than 10 times.

In order to avoid the previous issues, a full-wave numerical tool which solves coupled and volume integral equations, ADAMANT: the unknown quantities of the problem are the surface electric current density on the antenna and the volume polarization current within the plasma.

This code works avoiding the last two assumptions and without taking advantage of Fourier transforms; in addition, it was already used to find the power deposition in the plasma for some antenna configurations.

To proceed on this kind of study, it is necessary to confront analogous data between the two approaches explained until now: the first logical variable is the antenna current density spectrum. Since the antenna current is thought as uniform and imposed in the previous analysis, its spectrum has the same characteristics. On the other hand, in this thesis a new algorithm is developed in order to apply the Fourier transform to the antenna current density ADAMANT output, which is a 2D distribution function.

In this way, it is possible to understand whether there are potential new modes of excitation not considered with the "imposition" and "thin-wire" hypothesis.

Moreover, ADAMANT does not have the possibility to obtain the radial plasma power deposition profile in relation to a specific spectra value of the antenna current density function for a particular $m - k_z$ combination. Through SPIREs, the spectra derived by the new algorithm can be elaborated in order to define these profiles: the comparison with the previous analysis will be the final step of this thesis.

2

THE SPECTRAL ANALYSIS TOOL

In this chapter, the antenna current density will be examined as it is used in the previous approach. The imposed current and the thin-wire approximation will be linked to spectral relations: the excitation modes are variables of these equations and, thank to these ones, it is possible to see how the intensity of the current density, and consequently the power deposition into the plasma, is affected by these parameters.

Successively, the definition of the new code, which interfaces with ADAMANT, will be explained: the Fourier transform of the 2D current density function is implemented in order to obtain its spectra, which depends on the azimuthal and axial coordinates. Obviously, there is also a section in which the ADAMANT role is explained since it is the code which started this new approach.

In closing, there is a description of how it is possible to compare the new results with the previous ones derived by the earlier path: through a modified version of SPIREs, a further comparison can be done thanks to the new power deposition profiles obtained with the antenna current density spectra derived by ADAMANT.

2.1 HELIC CODE APPROACH

The thin-wire approximation and the imposed antenna current are the main hypothesis of the HELIC plasma code by Chen [11]-[12]: an example of the geometries analysed is tackled in Fig.2.1.

The power deposition into the plasma is related to the magnitude of the antenna current density spectrum; therefore, it is possible to find a relation between the excitation modes and the spectra function.

The general form of this physical quantity is $\vec{J}(r, \phi, z) = \delta(r - b) \cdot \vec{K}(\phi, z)$, where:

- $\vec{J}$ is the current density;
- r,ϕ and z are the radial, azimuthal and axial directions, with z parallel to the magnetic field B;

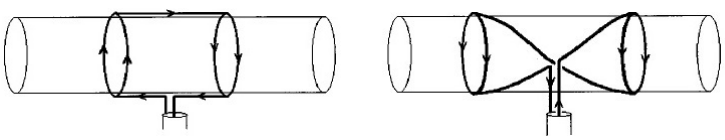

(a) *NagoyaIII (N3) antenna.* (b) *Half Helical (HH) antenna.*

Figure 2.1: Two of the antennas analysed by Chen[11][12] through the thin-wire hypothesis: the problem is faced considering a simplified 1-D antenna surrounding the plasma cylinder.

- b is the antenna radius;
- $\vec{K}$ is the radius independent function of $\vec{J}$.

Another assumption made is to consider the electrostatic fields shielded by the plasma, obtaining in this way the following relation:

$$\vec{\nabla} \cdot \vec{J} = 0 \tag{2.1}$$

If we introduce $\vec{K}(m, k_z)$ as the $\vec{K}(\phi, z)$ Fourier transform, with m the azimuthal mode and k_z the wave number, it is possible to determine another important relation through Eq.(2.1):

$$K_z(m, k_z) = -\frac{m}{b \cdot k_z} \cdot K_\phi(m, k_z) \tag{2.2}$$

Eq.(2.2) allows us to look only for the azimuthal component of the Fourier transform of $\vec{K}(\phi, z)$. Moreover, thanks to the thin-wire hypothesis, it is possible to find a general analytical solution for K_ϕ considering the two antenna examples:

$$K_\phi = -\frac{2}{\pi} I_0 \frac{k_z L}{2m} \frac{\sin(\frac{k_z L}{2} - m\theta)}{\frac{k_z L}{2} - m\theta} \tag{2.3}$$

where L is the antenna length, I_0 is the current expressed in Ampere and θ is the half the twist angle from one end to the other. Eq.(2.3) will be recalled in the next sections as a confrontation element with the ones obtained without the simplifications on the antenna geometry.

2.2 A SPECTRAL TOOL FOR 3D ANTENNAS

To solve the electromagnetic problem, the ADAMANT code applies the Fourier transforms on Rao, Wilton, Glisson (RWG) functions, taking into account in this way the finite dimension along the z-axis. The antenna current density is described in the following form:

$$\vec{J} \approx \sum_n \vec{f}_n(\vec{r})\, I_n \tag{2.4}$$

where $\vec{J}$ is the current density, n is the $n-th$ triangle couple considered, I_n is the complex coefficient of the current density and $\vec{f}$ is the RWG function, which is defined as follows

$$\vec{f}_n = \begin{cases} \pm \frac{l_{3n}}{2A_n^{\pm}} (\vec{r} - \vec{r}_{3n}^{\pm}) & \text{if } \vec{r} \in T_n^{\pm} \\ 0 & \text{otherwise} \end{cases} \tag{2.5}$$

in which $T_n^{\pm}$ is the triangle considered, $A_n^{\pm}$ is the area of the triangle, l_{3n} is the length of the common side of the triangles, and the other variables are deducible from Fig.A.1.

Hence, together with the antenna mesh files, it is possible to calculate the spectral response of the device.

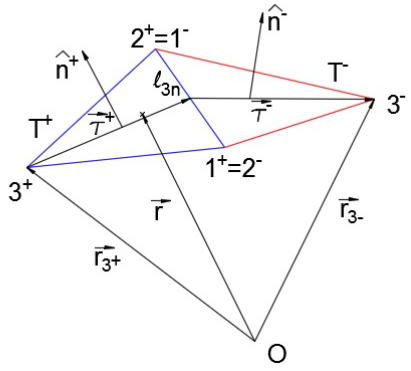

Figure 2.2: Nomenclature on a couple of triangles for RWG definition

Thanks to the "*rwg_ft*" sub-routine, the following integral can be computed:

$$\int_T \int dS \; e^{j\vec{K}\cdot\vec{r}} \; \vec{f}(\vec{r}) \tag{2.6}$$

where, referring to V. Lancellotti *et al.*[17]:

- **T** is the surface domain defined by the triangles and which refers to a specific RWG function;
- **dS** is the surface area element;
- $\vec{K}$ is the wave vector;
- $\vec{r}$ is the reference position vector;
- $\vec{f}$ is the RWG function.

Eq.(2.6) represents the spectral response of a specific RWG function, though the algorithm used in [17] is valid only if Cartesian coordinates are inserted as input. Since all the antenna configurations are axial-symmetric, it is logical to analyse the data through a cylindrical reference system.

In Fig.2.3 it is possible to see two coordinate systems: the Cartesian one $(\hat{x}, \hat{y}, \hat{z})$ and the cylindrical one $(\hat{\rho}, \hat{\phi}, \hat{z})$. In this way, a triad of unit vectors $\hat{n}, \hat{\tau}$ and $\hat{z}$ can be defined in order to guarantee the conversion of the wave vector $\vec{K}$ between the reference frames previously mentioned:

$$\vec{K} = K_z\hat{z} + K_\tau\hat{\tau} = K_z\hat{z} + \underbrace{K_\tau\hat{\tau}\cdot\hat{x}}_{K_x}\hat{x} + \underbrace{K_\tau\hat{\tau}\cdot\hat{y}}_{K_y}\hat{y} \tag{2.7}$$

In Eq.(2.7) almost all the spectral variables have been used:

- K_x is the wave-number along $\hat{x}$;
- K_y is the wave-number along $\hat{y}$;
- K_z is the wave-number along $\hat{z}$;
- K_τ is the wave-number along $\hat{\tau}$.

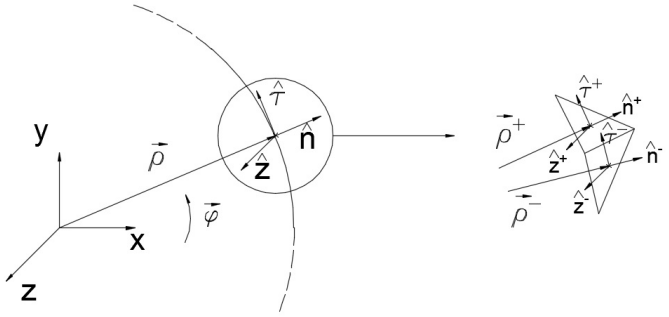

Figure 2.3: Spectral analysis versors scheme. On the left there is a global view with part of the antenna. On the right there are the versors on the triangles which define the RWG function domain.

K_τ would not be the correct variable to use in Eq.2.7, but the relation $K_\phi = \vec{K} \cdot \hat{\phi} \approx \vec{K} \cdot \hat{\tau} = K_\tau$ can be considered valid: in this way, the exciting mode m is introduced in order to define K_ϕ as $\frac{m}{a}$, with a the main radius of the antenna.

Since the current density on the antenna surface can be thought as Eq.(2.4), the code gives its spectral representation as follows:

$$\tilde{J} = \sum_n \int_{S_n} \int dS e^{jK_z z + jK_\tau s} \vec{f}_n(\vec{r})\ I_n \tag{2.8}$$

where $\vec{f}_n$ is the n^{th} RWG function, associated with the mesh, and I_n is the $n-th$ current coefficient, belonging to the list already quoted. Moreover, in Eq.(2.8) it is possible to recognize Eq.(2.6), although with $e^{jK_z z + jK_\tau s}$ instead of $e^{j\vec{K}\cdot\vec{r}}$, in which s stands for the arc length.

According to the cylindrical coordinate system, $\vec{J}$ and $\tilde{J}$ have two components: azimuthal(ϕ) and longitudinal(z).
Knowing that, for the former one, $J_\phi = \vec{J} \cdot \hat{\phi} \approx \vec{J} \cdot \hat{\tau} = \sum_n \vec{f}_n(\vec{r}) \cdot \hat{\tau}_n\ I_n$, it is easy to find the related one for the spectral variable:

$$\tilde{J}_\tau(K_z, K_\tau) = \sum_n \int_{S_n} \int dS e^{jK_z z + jK_\tau s} \vec{f}_n(\vec{r}) \cdot \hat{\tau}_n\ I_n \tag{2.9}$$

Proceeding in the same way, it is intuitive how to extract the longitudinal component, seeing that $J_z = \vec{J} \cdot \hat{z} = \sum_n \vec{f}_n \cdot \hat{z}\ I_n$:

$$\tilde{J}_z(K_z, K_\tau) = \sum_n \int_{S_n} \int dS e^{jK_z z + jK_\tau s} \vec{f}_n(\vec{r}) \cdot \hat{z}_n\ I_n \tag{2.10}$$

Recalling that RWG functions are defined for every couple of triangles sharing an edge, it is important how to specify the variables above the surface S_n, support of f_n. Looking at Fig.2.3, the unit vector $\hat{\tau}$ is taken as the aver-

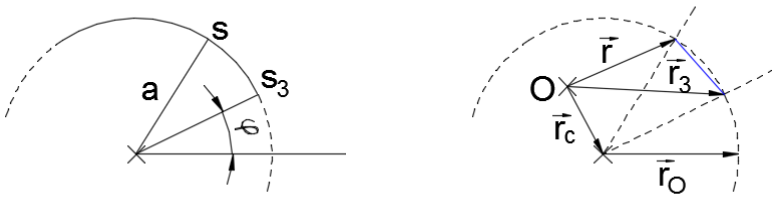

Figure 2.4: Phase explanation scheme. With this representation it is possible to take in account the contribution due to the phase respect to an arbitrary starting point.

age between $\hat{\tau}^+$ and $\hat{\tau}^-$, where $\hat{\tau}^\pm = \hat{z} \times \hat{n}^\pm$. Regarding the Fourier Transform computed by the sub-routine, $\tilde{f}_n^+$ and $\tilde{f}_n^-$ can be considered as:

$$\tilde{f}_n^+ = \int_{T^+} \int dS_n^+ e^{j\vec{K}\cdot\vec{r}} \, \vec{f}_n^+(\vec{r}) \tag{2.11}$$

$$\tilde{f}_n^- = \int_{T^-} \int dS_n^- e^{j\vec{K}\cdot\vec{r}} \, \vec{f}_n^-(\vec{r}) \tag{2.12}$$

where $T^\pm$ stands for the triangles domain.

The elaboration of the formulas is not finished because $K_z z + K_\tau s \neq \vec{K}\cdot\vec{r}$; therefore, with the aid of Fig.2.4, the following passages will explain the right equivalence:

$$K_z z + K_\tau s = \vec{K}\cdot(z\hat{z} + s\hat{\tau}) = \vec{K}\cdot[(z-z_3)\hat{z} + (s-s_3)\hat{\tau}] + \vec{K}\cdot(z_3\hat{z} + s_3\hat{\tau}) \tag{2.13}$$

where

- z_3 is the z-coordinate of the third vertex 3^+, belonging to the triangle couple examined;
- s_3 arc length delineated by the 3^+ point, that is, $a \cdot \phi_3$ with a the antenna radius and ϕ_3 the angle swept by s_3.

Thanks to the right picture in Fig.2.4, these simplifications can be made:

- $s - s_3 \simeq (\vec{r} - \vec{r}_3)\cdot\hat{\tau}$
- $z - z_3 = (\vec{r} - \vec{r}_3)\cdot\hat{z}$
- $\cos\phi_3 = \dfrac{(\vec{r}_3 - \vec{r}_C)\cdot(\vec{r}_O - \vec{r}_C)}{|\,\vec{r}_3 - \vec{r}_C\,|\,|\,\vec{r}_O - \vec{r}_C\,|}$

Recalling Eq.(2.13), it is possible to obtain the final equivalence:

$$\begin{aligned} K_z z + K_\tau s &\simeq \vec{K}\cdot(\vec{r} - \vec{r}_3) + K_z z_3 + K_\tau s_3 = \\ &= \vec{K}\cdot\vec{r} - K_\tau(\hat{\tau}\cdot\vec{r}_3 - s_3) \end{aligned} \tag{2.14}$$

In closing, Eq.(2.9) is described by the next relation:

$$\tilde{J}_\tau(K_z, K_\tau) \approx \sum_n \underbrace{\int_{S_n} \int dS\ e^{j\vec{K}\cdot\vec{r}}\ \vec{f}_n(\vec{r})}_{\text{as Eq.(2.11–2.12)}} \cdot\hat{\tau}\ \underbrace{e^{-jK_\tau(\hat{\tau}\cdot\vec{r}_3 - s_3)}}_{\text{phase factor}} \tag{2.15}$$

and Eq.(2.10) is as:

$$\tilde{J}_z(K_z, K_\tau) \approx \sum_n \underbrace{\int_{S_n} \int dS\ e^{j\vec{K}\cdot\vec{r}}\ \vec{f}_n(\vec{r})}_{\text{as Eq.(2.11–2.12)}} \cdot\hat{z}\ \underbrace{e^{-jK_\tau(\hat{\tau}\cdot\vec{r}_3 - s_3)}}_{\text{phase factor}} \tag{2.16}$$

where the phase contribution will be $\neq 1$, since generally $\hat{\tau}\cdot\vec{r}_3 \neq s_3$.

The last form of the previous equations, which have been used to implement the final code, is:

$$\tilde{J}_\tau(K_z, K_\tau) = \sum_n (\tilde{f}_n^+ + \tilde{f}_n^-)\cdot\hat{\tau}\ I_n\ e^{-jK_\tau(\hat{\tau}\cdot\vec{r}_3 - s_3)} \tag{2.17}$$

$$\tilde{J}_z(K_z, K_\tau) = \sum_n (\tilde{f}_n^+ + \tilde{f}_n^-)\cdot\hat{z}\ I_n\ e^{-jK_\tau(\hat{\tau}\cdot\vec{r}_3 - s_3)} \tag{2.18}$$

2.3 THE ADAMANT TOOL

One of the aim of this thesis is to find differences between the thin-wire antenna hypothesis, used by F.F.Chen[11][12], and the real antenna analysis studied thanks to the ADAMANT code [18]: it is a FORTRAN code devised to study the antenna-plasma interaction through a system of coupled surface (SIE) and volume (VIE) integral equations [19]. The former ones govern the boundary condition of the total tangential electric field on the perfect electric conductor antenna [20], whilst the latter ones are related to the behaviour of the total electric field inside the excited plasma[21]. The unknowns are, therefore, the surface electric current density on the antenna and the volume polarization current within the plasma: the Method of Moments in the form of Galerkin with subsectional basis and test functions is applied on unstructured meshes, namely triangles for the surface functions and tetrahedra for the volume ones[22][23].

With ADAMANT, only an analysis on the antenna impedance, and consequently on the power deposition response, was done [24], not allowing, in this way, a formulation about the relation between the current density spectrum and the power deposited in the plasma.

As written before, among ADAMANT outputs, the ones of interest are the imaginary and real coefficients of the current density on the antenna surface.

In Fig2.5, it is possible to observe the disposition of the data: the first column states the voltage gap port excited; the second represents the RWG function interested, and the last two are the coefficients.

In addition, the structure of the FORTRAN code was really helpful in order to develop, in a rapid and safe way, the code to calculate the spectra and the one to perform the test of the uniform current imposed: precisely, for the former case, Eq.2.17 and Eq.2.18 were computed thanks also to the pre-existing sub-routines previously mentioned; on the other hand, for the latter code, Eq.A.9 was the principal issue.

```
%%% Port #   Fnc #      real(Ia) [A/m]      imag(Ia) [A/m]
%%%
        1        1       0.90445E-01       0.21094E+00
        1        2      -0.14892E+00      -0.34731E+00
        1        3       0.13876E+00       0.52326E+00
        1        4      -0.22847E+00      -0.86154E+00
        1        5      -0.13517E+00      -0.53202E+00
        1        6       0.22256E+00       0.87597E+00
        1        7      -0.94044E-01      -0.20238E+00
        1        8       0.15485E+00       0.33321E+00
        1        9      -0.15791E+00      -0.50592E+00
        1       10       0.18868E+00       0.60453E+00
        1       11      -0.15792E+00      -0.50600E+00
        1       12       0.18869E+00       0.60461E+00
```

Figure 2.5: Example of the output file in which the real and imaginary coefficients of the current density antenna are listed

2.4 CODES COMPARISON

In order to understand the concreteness of the results obtained after this stage, it is necessary to compare analogous variables of the new and old approach.

The latter one studies the electromagnetic problem imposing the antenna current and considering the geometry with the thin-wire hypothesis: within the HELIC and ANTENA codes, the TF is applied to the current in order to calculate the radial plasma power deposition and the other electromagnetic variables.
On the other hand, the former one does not use these simplifications and derives an antenna current density function over a surface, obtained studying the mutual interaction between the antenna and the plasma during the elaboration.

To compare these two thinking lines, it is necessary to extract the spectra information from the 3D antenna current density distribution derived by ADAMANT: the algorithm described before helps in doing this through the TF application, all adapted to the RWG functions.

In addition, since now a real antenna current density profile is available, it is possible to use the SPIREs code[13].

It is a a Finite-Difference Frequency-Domain (FDFD) electromagnetic solver in one dimension for the rapid calculation of the electromagnetic fields and the deposited power of a large variety of cylindrical plasma problems.

The input could be either the electric current function or its spectra: since the second one is available, the further step consists of analysing the radial plasma power deposition and comparing it with the ones determined through the old approach.

3

THE CODE VALIDATION

This chapter deals with the preliminary analysis of simple antenna configurations for which it is possible to obtain an analytical reference function of the current density spectrum.

The first part consists of a benchmark in which the algorithm in order to impose a uniform current on an antenna is explained: this was necessary since all the current density functions for these kind of configurations are described as $\vec{J}(\rho, \phi, z) = J_0 \, f(\rho, \phi, z)$, where J_0 is the constant current density assumed.

The second part describes how to calculate an analytical reference function of an antenna configuration: a Fourier transform is applied in the same way used by Chen[12], though without the thin-wire approximation an without the axial connections between the loops. In addition, there is a comparison between this type of result and the one obtained by applying the code to the same configuration.

Finally, the mesh precision on other three antenna configurations will be varied in order to understand its influence on the spectra functions.

3.1 VALIDATION

The section deals with the validation approach used for the code described in the Chapter 2.

Three simple antenna configurations will be analysed: they are similar to the single Loop, Nagoya III and the Fractional Helix. Although the thin-wire hypothesis is still valid, the axial connections are not considered and the two antenna extremities are surfaces and not filamentary.

Through the procedure explained by Chen[12], it is possible to apply the Fourier transform to simple current density functions corresponding to the configurations studied.

The final aim is to verify that the results obtained by the previous equations, which are a consequence of Eq.(2.2) and Eq.(2.3), and the ones derived by the application of the code are the same.

3.1.1 *Single-Loop*

The "*Single-Loop*" antenna has the following characteristics:

- antenna radius a = 0.05m;
- antenna width w=0.005m.

From Fig.3.1, it is possible to define the ideal function of the current density $\vec{J}$:

$$\vec{J}(\rho, \phi, z) = J_0 \, \delta(r - a) \, u_\phi(0; 2\pi) \, u_z(-\frac{w}{2}; \frac{w}{2}) \tag{3.1}$$

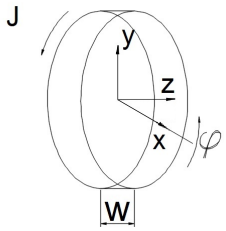

Figure 3.1: Single-Loop scheme

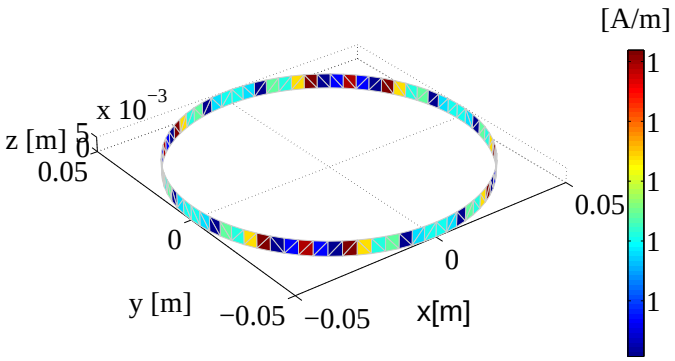

Figure 3.2: Single Loop plot with an imposed uniform density current of $1\frac{A}{m}$

where:

- J_0 is the density current magnitude;
- u_ϕ and u_z are the Heaviside functions.

In the spectral domain, the expression changes into the following one:

$$\tilde{J}_\phi = \int_{-w/2}^{w/2} e^{-jK_z z} dz \int_0^{2\pi} a\, J_0(\phi, z) e^{-jm\phi} d\phi \tag{3.2}$$

Assuming $J_0(\phi, z)$ as constant and equals to $1\frac{A}{m}$, the previous relation becomes:

$$\tilde{J}_\phi = J_0(\phi, z)\, 2\frac{\sin(K_z \frac{w}{2})}{K_z}\, 2\pi\, a\, \delta(m) \tag{3.3}$$

The definition of J_0 is $\frac{I}{w}$, with I the electric current expressed in [A]; therefore, the analytical reference function can be written as:

$$\begin{aligned} \tilde{J}_\phi &= I\, \mathrm{sinc}(K_z \frac{w}{2})\, 2\pi\, a\, \delta(m) = \\ &= J_0\, w\, \mathrm{sinc}(K_z \frac{w}{2})\, 2\pi\, a\, \delta(m) = \\ &= \mathrm{sinc}(K_z \frac{w}{2})\, 2\pi\, a\, w\, \delta(m) \end{aligned} \tag{3.4}$$

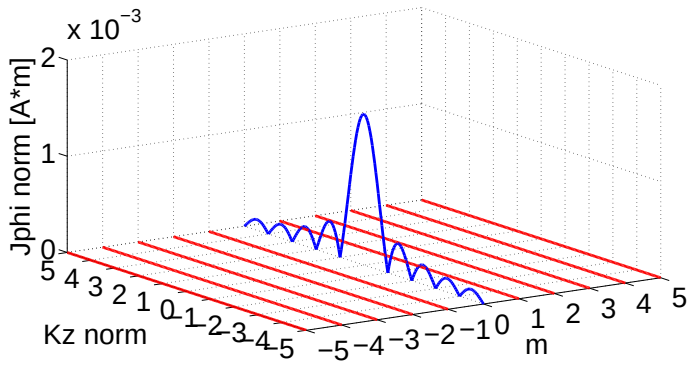

(a) J_ϕ *norm 3D plot*

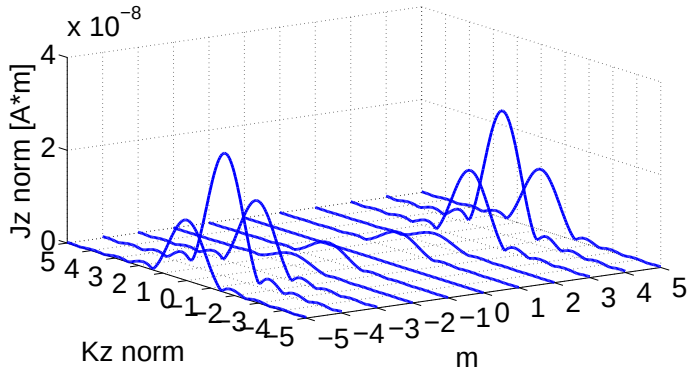

(b) J_z *norm 3D plot*

Figure 3.3: Spectral representation of the current density components with n°RWG=152 for the Single Loop antenna.

In Fig.3.2, it is possible to observe the plot of the imposed current density $\vec{J}$ together with the spectral analysis. It is evident that there is only a contribute in Fig.3.3a for m=0: this was expected, seeing that $\tilde{J}_\phi = 0$ for others m values in Eq,(3.4). On the other hand, there is not a $\tilde{J}_z$ function because $\vec{J}$ is parallel to $\hat{\phi}$: Fig.3.3b shows small contributions, which are the consequence of the approximation with the mesh and which can be considered irrelevant, since there are 3 orders of magnitude of difference between $\tilde{J}_\phi$ and $\tilde{J}_z$.

However, this is not enough to be sure about what obtained through the code; this is why in Fig.3.4, it is possible to observe as, for m=0, the two curves are coincident: this is the prove that the analysis on a Single-Loop antenna configuration are reliable.

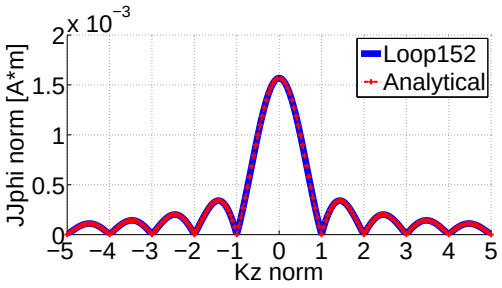

Figure 3.4: J_ϕ norm comparison between code and analytical result for m=0. k_z is the normalised axial wave-number, that is divided by $\frac{2\pi}{L}$.

3.1.2 *Nagoya*

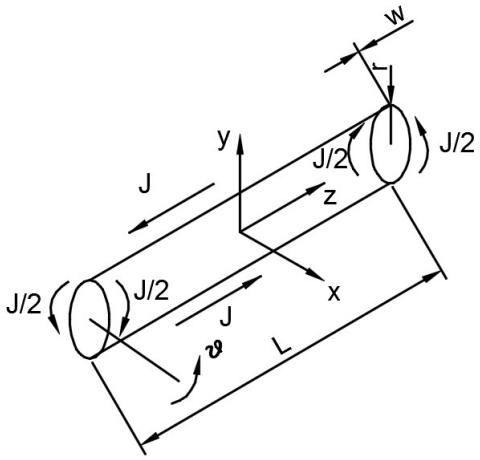

Figure 3.5: Approximation NagoyaIII scheme. The two loops at the extremities must be considered as surfaces with the normal vector pointing outwards and with a length equals to w. The axial connections are represented only to make understand the disposition of the current density $\vec{J}$.

It is difficult to determine an analytical reference function for a whole Nagoya antenna; therefore, it has been used a trick to simulate the same $\vec{J}$ behaviour, that is, studying 2 Loops configuration without the longitudinal links, but with a current density distribution as shown in Fig.3.5.

The geometrical dimensions of the new configuration are:

- antenna radius a = 0.05m;
- Loop width w=0.005m;
- whole antenna width L=0.05m.

The analytical reference function can be found out, knowing that the current density $\vec{J}$ is as follows:

$$J_\phi(r,\phi,z) = \frac{J_0}{2}\,\delta(r-a)\big[u_\phi(-\frac{\pi}{2};\frac{\pi}{2}) - u_\phi(\frac{\pi}{2};\frac{3\pi}{2})\big] \\ \big[u_z(\frac{L-w}{2};\frac{L-w}{2}) - u_z(\frac{-L-w}{2};\frac{-L+w}{2})\big] \tag{3.5}$$

where

- J_0 is the current density modulus, which is equal to $1\frac{A}{m}$;
- u_ϕ and u_z are the Heaviside functions.

Transferring the analysis into the spectral domain, the previous equation changes to:

$$\begin{aligned}
&\hat{J}_\phi = \frac{J_0}{2}\Big[\int_{\frac{L-w}{2}}^{\frac{L-w}{2}} e^{-jK_z z}\,dz - \int_{\frac{-L-w}{2}}^{\frac{-L+w}{2}} e^{-jK_z z}\,dz\Big] \\
&\Big[\int_{-\frac{\pi}{2}}^{\frac{\pi}{2}} b\,d\phi\,e^{-jm\phi} - \int_{\frac{\pi}{2}}^{\frac{3\pi}{2}} b\,d\phi\,e^{-jm\phi}\Big] = \\
&= \frac{J_0}{2}\,\frac{e^{-jK_z(\frac{L+w}{2})} - e^{-jK_z(\frac{L-w}{2})} - e^{-jK_z(\frac{-L+w}{2})} + e^{-jK_z(\frac{-L-w}{2})}}{-jK_z}\,b \\
&\frac{e^{-jm\frac{\pi}{2}} - e^{+jm\frac{\pi}{2}} - e^{-jm\frac{3\pi}{2}} + e^{-jm\frac{\pi}{2}}}{-jm} = \\
&= \frac{J_0}{2}\,2\Big[\cos\big(K_z(\frac{L+w}{2})\big) - \cos\big(K_z(\frac{L-w}{2})\big]\frac{1}{-jK_z}\,b\,\frac{-2e^{jm\frac{\pi}{2}} + 2e^{-jm\frac{\pi}{2}}}{-jm} = \\
&= -8(-1)^m\frac{J_0\,b}{K_z m}\Big[\sin(\frac{L}{2}K_z)\sin(K_z\frac{w}{2})\Big]
\end{aligned} \tag{3.6}$$

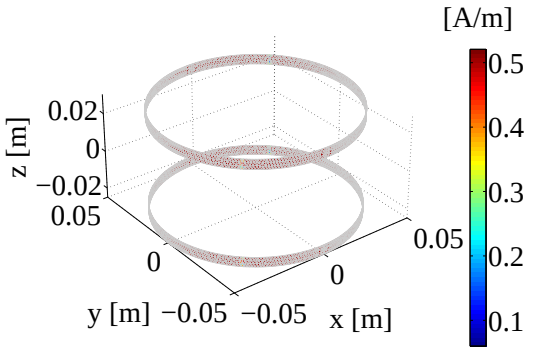

Figure 3.6: Mesh representation and current density distribution of the antenna similar to the Nagoya III. It is possible to see how $\vec{J}$ has been divided in two as concern for its magnitude(the only non red triangles are the limit of this division): in this way the same Nagoya behaviour has been reproduced.

From Fig.3.6, it is possible to understand that J_0 has been split in two parts as wanted: there are only a few triangles which are influenced by the division

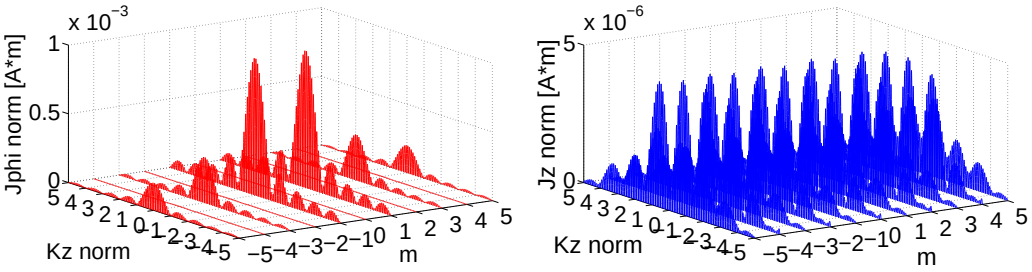

(a) J_ϕ *norm 3D plot* (b) J_z *norm 3D plot*

Figure 3.7: Spectral representation of the current density components with n°RWG=3000 for the Nagoya antenna approximation. k_z is the normalised axial wave-number: it is divided by $\frac{2\pi}{L}$.

area; nevertheless, they don't cause perturbation to the data because of the thick mesh.

As was the case for the Loop configuration, in Fig.3.7b, J_z is clearly smaller than J_ϕ and it can be considered null. About Fig.3.7a, J_ϕ is not null only for odd m, as expected by Eq.(3.6).

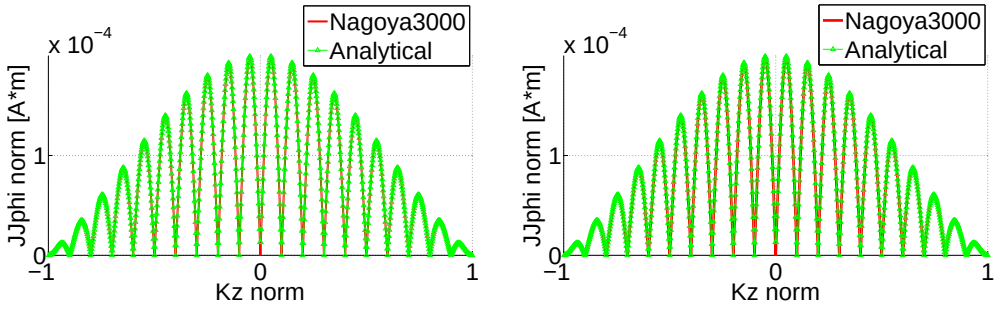

(a) J_ϕ *spectrum for m=-5* (b) J_ϕ *spectrum for m=+5*

Figure 3.8: Spectrum comparison of J_ϕ for m=±5

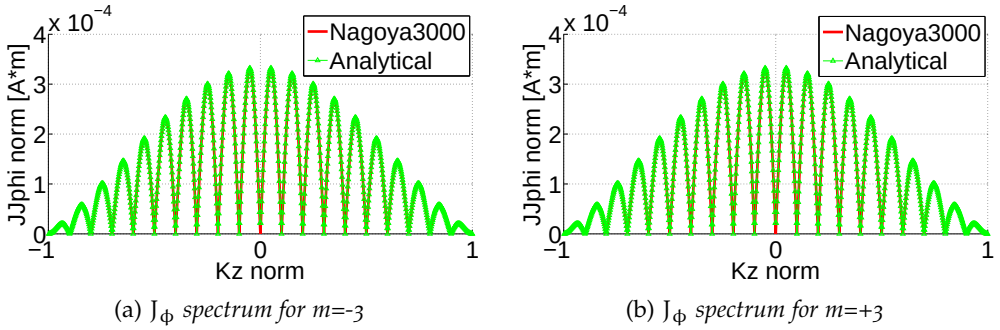

(a) J_ϕ *spectrum for m=-3* (b) J_ϕ *spectrum for m=+3*

Figure 3.9: Spectrum comparison of J_ϕ for m=±3

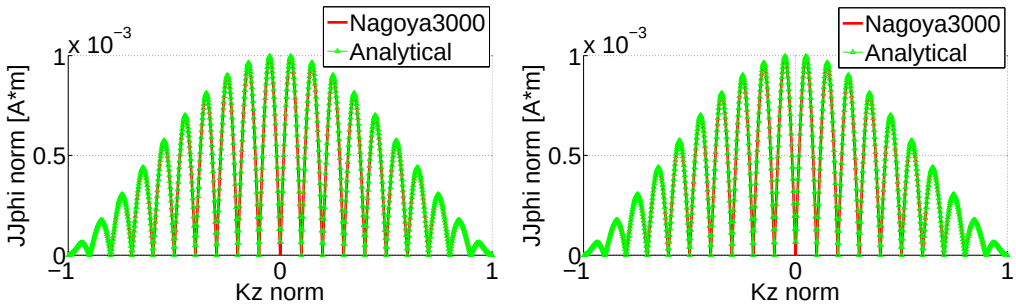

(a) J_ϕ *spectrum for m=-1* (b) J_ϕ *spectrum for m=+1*

Figure 3.10: Spectrum comparison of J_ϕ for m=$\pm$1

Howbeit, it is possible to ascertain the soundness of these results only analysing figures 3.8-3.9-3.10: the two curves are coincident and, therefore, it is reasonable to proceed with the test on a real Nagoya antenna.

3.1.3 *Fractional Helix*

Analogously to the Nagoya case, it is possible to see the approximative representation in Fig.3.11: two Loops with the same $\vec{J}$ distribution in order to simulate the same behaviour of a Helix antenna with a constant current density. Although the geometrical dimensions are the same as the Nagoya ones, the

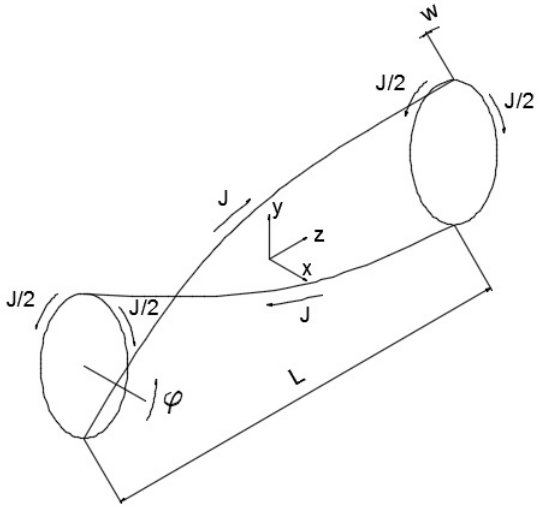

Figure 3.11: Approximation of the Fractional Helix antenna. As for the Nagoya, the axial links are represented only in order to justify the current density distribution in the two loops extremities.

analytical reference function is different, since $\vec{J}$ can be taken as:

$$J_\phi(r,\phi,z) = \frac{J_0}{2}\,\delta(r-a)\big[u_\phi(-\frac{\pi}{2};\frac{\pi}{2}) - u_\phi(\frac{\pi}{2};\frac{3\pi}{2})\big] \big[u_z(\frac{L-w}{2};\frac{L-w}{2}) + u_z(\frac{-L-w}{2};\frac{-L+w}{2})\big] \tag{3.7}$$

where

- J_0 is the constant current density whose value is $1\ \frac{A}{m}$;
- a is the antenna radius;
- u_ϕ e u_z are the Heaviside functions;
- L is the antenna width;
- w is the Loop width.

Working in the spatial spectral domain, it is easy to obtain the following expression:

$$\begin{aligned}
\tilde{J}_\phi &= \frac{J_0}{2}\Big[\int_{\frac{L-w}{2}}^{\frac{L-w}{2}} e^{-jK_z z}\,dz + \int_{\frac{-L-w}{2}}^{\frac{-L+w}{2}} e^{-jK_z z}\,dz\Big] \\
&\Big[\int_{-\frac{\pi}{2}}^{\frac{\pi}{2}} b\,d\phi\,e^{-jm\phi} - \int_{\frac{\pi}{2}}^{\frac{3\pi}{2}} b\,d\phi\,e^{-jm\phi}\Big] = \\
&= \frac{J_0}{2}\,\frac{e^{-jK_z(\frac{L+w}{2})} - e^{-jK_z(\frac{L-w}{2})} + e^{-jK_z(\frac{-L+w}{2})} - e^{-jK_z(\frac{-L-w}{2})}}{-jK_z}\,b \\
&\frac{e^{-jm\frac{\pi}{2}} - e^{+jm\frac{\pi}{2}} - e^{-jm\frac{3\pi}{2}} + e^{-jm\frac{\pi}{2}}}{-jm} = \\
&= \frac{J_0}{2}\,2\Big[\sin\big(K_z(\frac{L+w}{2})\big) - \sin\big(K_z(\frac{L-w}{2})\big]\frac{1}{-jK_z}\,b\,\frac{-2e^{jm\frac{\pi}{2}} + 2e^{-jm\frac{\pi}{2}}}{-jm} = \\
&= -8(-1)^m\frac{J_0\,b}{K_z m}\Big[\cos(\frac{L}{2}K_z)\sin(K_z\frac{w}{2})\Big]
\end{aligned} \tag{3.8}$$

The description of Fig.3.12 is similar to that analogue of the Nagoya antenna: it is possible to see the division of the current density J_0 even though not its direction; thanks to Fig.3.13, we can see that J_z is lower of 3 order of magnitude than J_ϕ, which is not null only for odd values of m.

From Fig.3.14, Fig.3.15 and Fig.3.16, it is reasonable to claim again that the code is valid for this particular antenna configuration.

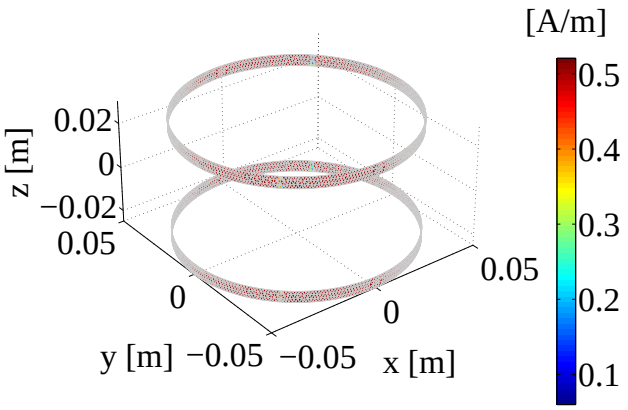

Figure 3.12: Mesh representation and current density distribution of the Fractional Helix approximation. The non red triangles highlight the division area of the current density in order to reproduce the Fractional Helix current distribution.

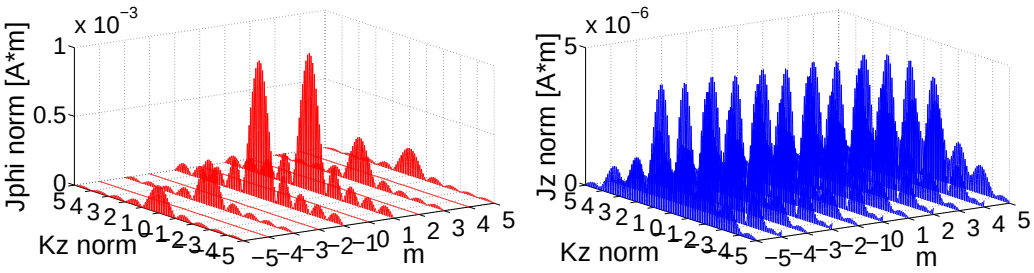

(a) J_ϕ *norm 3D plot* (b) J_z *norm 3D plot*

Figure 3.13: Spectral representation of current density components with n°RWG=3000 for the Fractional Helix antenna approximation. k_z is the normalised axial wave-number, that is divided by $\frac{2\pi}{L}$.

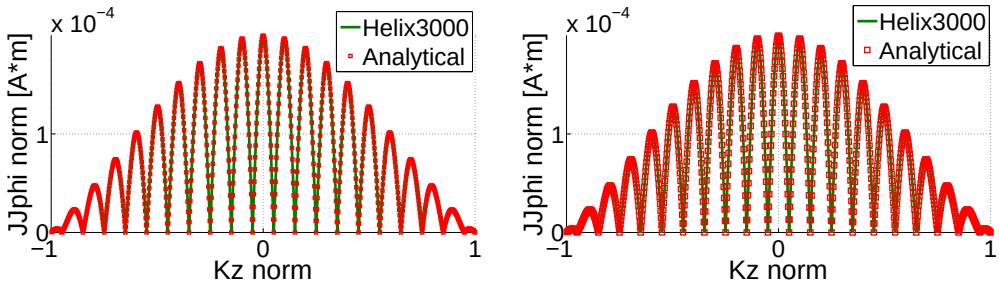

(a) J_ϕ *spectrum for m=-5* (b) J_ϕ *spectrum for m=+5*

Figure 3.14: Spectrum of J_ϕ for m=±5

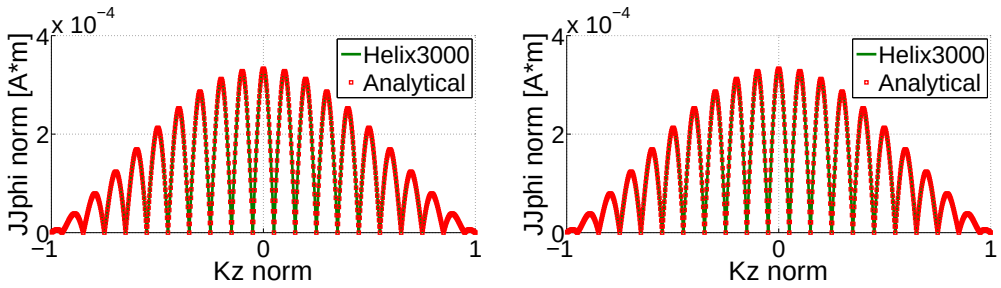

(a) J_ϕ *spectrum for m=-3* (b) J_ϕ *spectrum for m=+3*

Figure 3.15: Spectrum of J_ϕ for m=±3

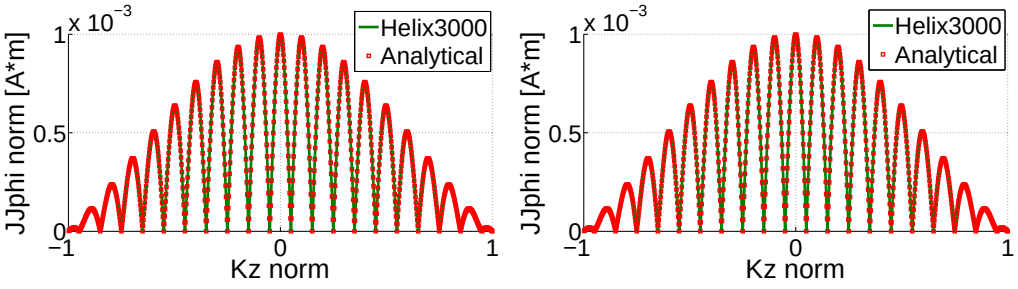

(a) J_ϕ *spectrum for m=-1* (b) J_ϕ *spectrum for m=+1*

Figure 3.16: Spectrum of J_ϕ for m=±1

3.2 MESH INFLUENCE ANALYSIS

This section topic concerns the relation between the spectrum of the current density and the mesh precision of the antenna configuration.

ADAMANT simulations have been launched to study a real set of Single Loop, Nagoya III and Fractional Helix antennas in order to obtain the complex coefficients of the current density function. Successively, the code elaborates these inputs so it is possible to analyse the spectral functions.

This kind of analysis has been made in order to find potential instabilities due to the number of RWG functions used for the simulations. In addition, as the number of triangles is increased, the current density distribution changes, so it is interesting whether this behaviour influences the spectrum function or not.

3.2.1 *Single-Loop*

In Fig.3.17, Fig.3.18, Fig.3.19 and Fig.3.20 the plots for different meshes are shown in order to have a quick look on the possible differences of the data. Only in Fig.3.19b there aren't null contributions for $m \neq 0$: this can be explained since the mesh is not uniform in the loop. It is possible to see zones in which

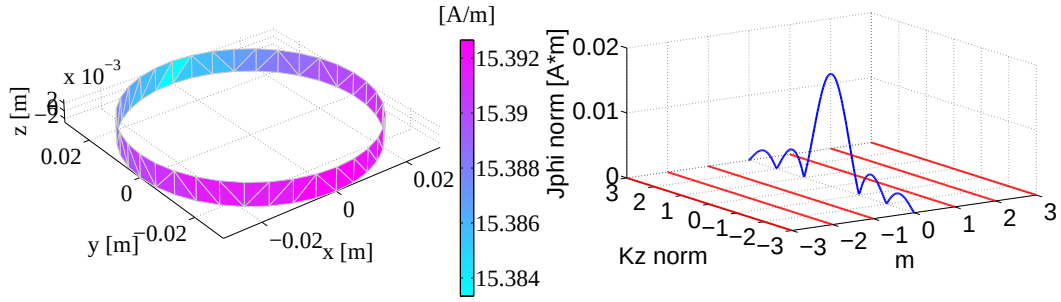

(a) *Loop mesh and current density distribution with n°RWG=72*

(b) *3D J_ϕ spectrum for B=10mT, T=3eV, p=15mTorr, $n=5 \cdot 10^{17} m^{-3}$*

Figure 3.17: Single-Loop output plot with n°RWG=72

the antenna width is characterised by 3 triangles and others by 2: this causes a perturbation in the vector $\vec{J}$, which is not more parallel to $\hat{\phi}$ in those regions.

In Fig.3.21, J_ϕ is illustrated for each case studied: for n°RWG equals to 268, the curve is coincident with the original one(n°RWG=72). As the number of triangles raises, the maximum value doesn't change much, but it is possible to observe how the secondary oscillations are higher than the main ones: maybe, the higher magnitude value of $\vec{J}$ can influence the shape of the curve.

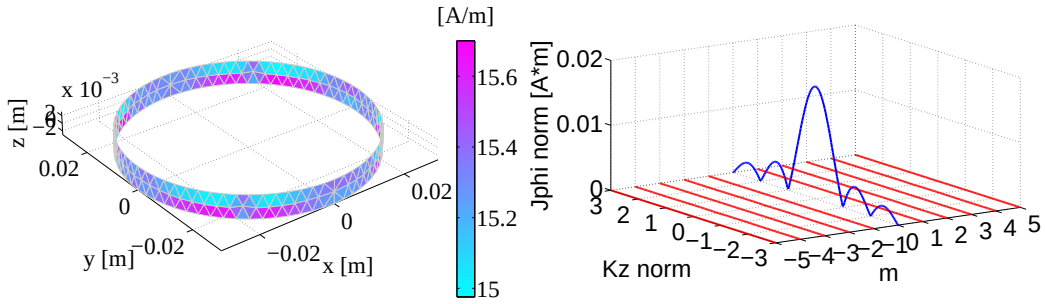

(a) *Loop mesh and current density distribution with n°RWG=268*

(b) *3D J_ϕ spectrum for B=10mT, T=3eV, p=15mTorr, $n=5 \cdot 10^{17} m^{-3}$*

Figure 3.18: Single-Loop output plot with n°RWG=268

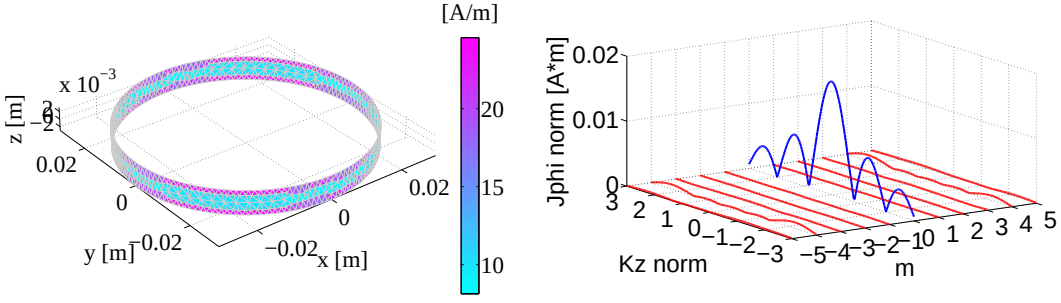

(a) *Loop mesh and current density distribution with n°RWG=972*

(b) *3D J_ϕ spectrum for B=10mT, T=3eV, p=15mTorr, $n=5 \cdot 10^{17} m^{-3}$*

Figure 3.19: Single-Loop output plot with n°RWG=972

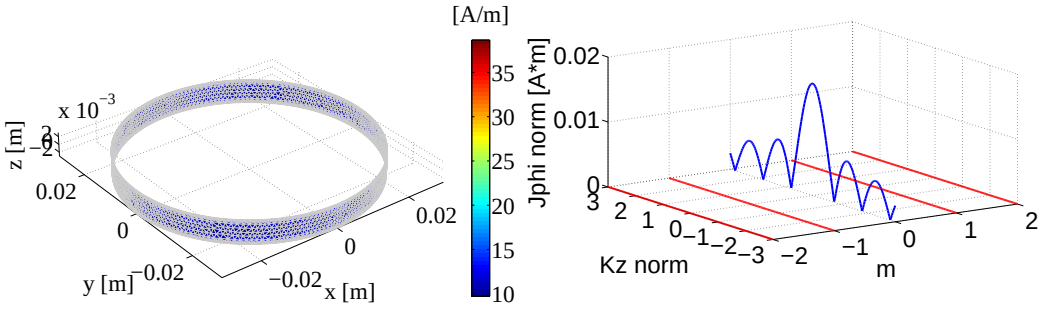

(a) *Loop mesh and current density distribution with* $n°RWG=4000$ (b) *3D* J_ϕ *spectrum for B=10mT, T=3eV, p=15mTorr,* $n=5 \cdot 10^{17} m^{-3}$

Figure 3.20: Single-Loop output plot with n°RWG=4000

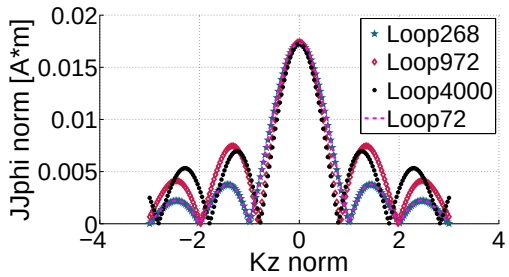

Figure 3.21: J_ϕ spectrum comparison with B=10mT, T=3eV, p=15mTorr, $n=5 \cdot 10^{17} m^{-3}$. k_z is the normalised axial wave-number, that is divided by $\frac{2\pi}{L}$.

3.2.2 *Nagoya*

In Fig.3.22, it is possible to observe the Nagoya current density distribution for different meshes: Fig.3.22a shows the original antenna, whilst Fig.3.22b has the same characteristics, but it was obtained from an another simulation, in order to verify, one more time, the soundness of the results. As expected, they are identical.

On the other hand, with n°RWG=2772, $\vec{J}$ tends to raise at the borders of the antenna, and to decrease within its surface.

However, Fig.3.23 shows how this different of the distribution doesn't affect the general behaviour of the curves: it is still underlined the different amplitude of the secondary oscillations.

3.2.3 *Fractional Helix*

It is possible to see in Fig.3.24 how different results for $\vec{J}$ can be obtained with the same number of triangles not disposed in the same way: Fig.3.24a and Fig.3.24b show this peculiarity, although the final consideration, together with Fig.3.24c, about $\vec{J}$ distribution is always the same. In the last figure, it is difficult to see the peak values of the current density since the triangles are so little that only a row of them is needed to represent them at the boundary of the helical links.

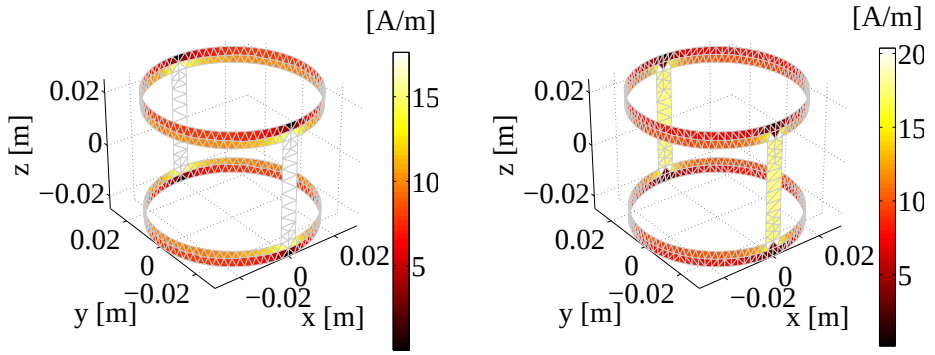

(a) *Nagoya mesh and current density distribution with n°RWG=770*

(b) *Nagoya mesh and current density distribution with n°RWG=772*

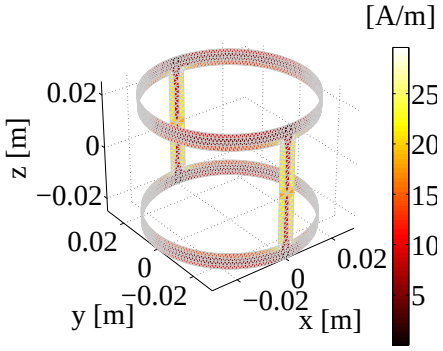

(c) *Nagoya mesh and current density distribution with n°RWG=2772*

Figure 3.22: Nagoya current density distribution comparison for different meshes.

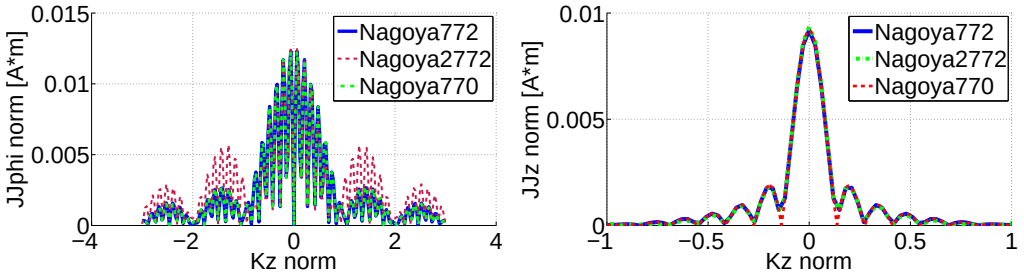

(a) J_ϕ *comparison*

(b) J_z *comparison*

Figure 3.23: Spectrum comparison for m=+1 between different meshes with B=10mT, T=3eV, p=15mTorr, n=$1 \cdot 10^{16} m^{-3}$. k_z is the normalised axial wave-number, that is divided by $\frac{2\pi}{L}$.

From Fig.3.25, it is possible to notice more differences than those observed for the other antenna configurations: the maximum values for n°RWG=700 or n°RWG=4000 are slightly lower than the one belonging to the original simulation. Moreover, the period of the functions in Fig.3.25a seems different: all these disparities can be cause by little variations of the geometry between the origi-

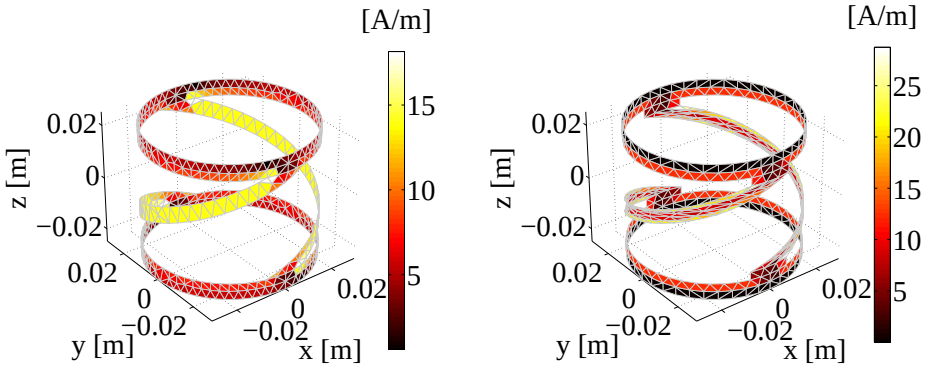

(a) *Fractional Helix mesh and current density distribution with n°RWG=770*

(b) *Fractional Helix mesh and current density distribution with n°RWG=772*

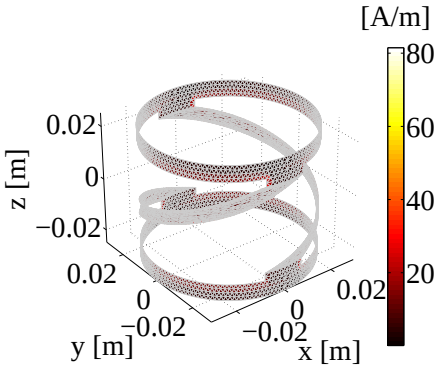

(c) *Fractional Helix mesh and current density distribution with n°RWG=2772*

Figure 3.24: Current density distribution comparison for different Fractional Helix meshes.

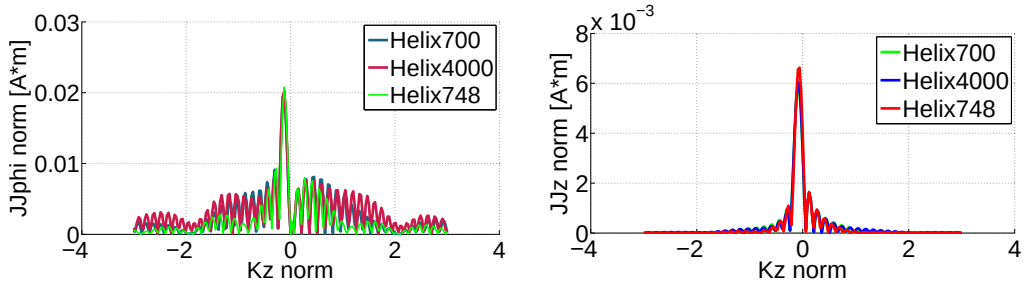

(a) J_ϕ *comparison*

(b) J_z *comparison*

Figure 3.25: Spectrum comparison for m=+1 between different meshes with B=20mT, T=7eV, p=15mTorr, n=$1 \cdot 10^{17}\,m^{-3}$. k_z is the normalised axial wave-number, that is divided by $\frac{2\pi}{L}$.

nal antenna and the later ones; furthermore, it is not easy to choose the same triangles which define the antenna port.

3.3 CONCLUSION

For the Single-Loop and the Nagoya III antennas, it is possible to observe a little difference in the phase of the functions as the number of triangles rises. Moreover, the secondary oscillations are much higher than the main ones, which is probably due to the high peak reached by the current density functions at the borders of the antennas: with a thick mesh, it is possible to define at least three triangle rows along the loop surfaces, observing in this way how the current density presents a "valley" behaviour with peak values at the borders of antenna.

The Fractional Helix test is influenced by a slightly different geometry; however, only a difference in the phase has been detected.

All in all, from this quick analysis it is possible to affirm that, although the spatial distribution of $\vec{J}$ varies with the mesh, the latter has little effect on the spectrum response.

4

ANTENNA CONFIGURATIONS ANALYSIS

In this chapter, the spectrum of the antenna current density spectrum will be studied by varying the discharge parameters, such as the field magnetic intensity, the background pressure, the electronic temperature and the plasma density.

A similar work was done by Melazzi and Lancellotti[24] with ADAMANT. Thanks to this code, it is possible to analyse the power deposition into the plasma by determining the antenna input impedance: since for RF frequencies the power radiated by the antenna into free space is negligible, the power entering the antenna is entirely absorbed by the plasma.

The aim is to understand if the variations caught with ADAMANT simulations will appear again analysing the spectral functions.

In addition, there will be a comparison between the plots obtained through the new algorithm and the formulas utilised by Chen[12] in the HELIC code: since from the ADAMANT analysis it was observed that the current density distribution on the surface is not uniform, as assumed for the previous approach typologies, the possibility that higher m modes are excited cannot be discarded.

4.1 SINGLE-LOOP

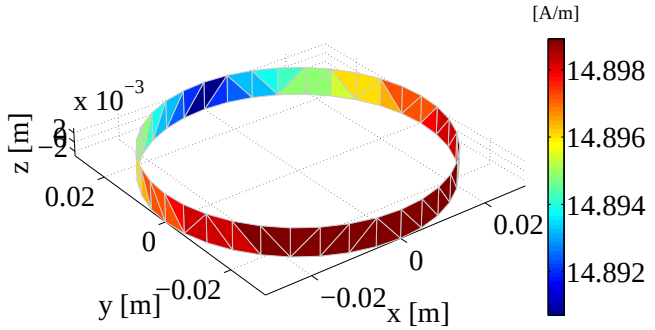

Figure 4.1: Single-Loop mesh and current density distribution plot for B= 50mT, n= $3 \cdot 10^{17} m^{-3}$, T= 7eV, p= 30mTorr. k_z is the normalised axial wave-number, that is divided by $\frac{2\pi}{L}$.

Fig.4.1 and Fig.4.2 show an example of the plot results obtained by the code, applied to a Single-Loop antenna with a general combination of discharge parameters: despite the large amount of data, all the pictures acquired are similar; hence, we choose to illustrate only a particular case.

In Fig.4.1, it is possible to see the constant distribution of the current density $\vec{J}$, whilst in Fig.4.2a there is a contribution in J_ϕ for only m=0. All in all, in Fig.4.2b, J_z can be considered null compared to J_ϕ.

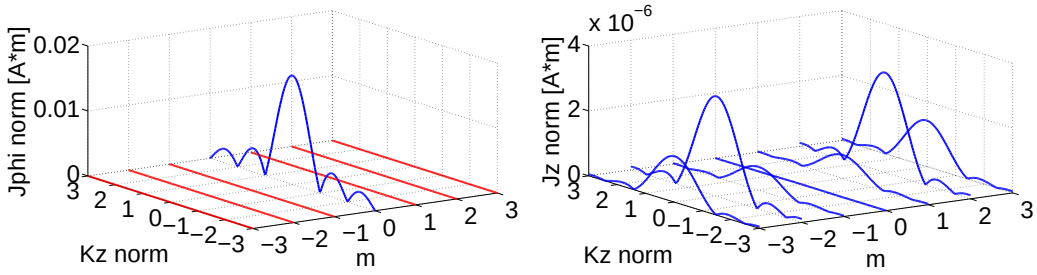

(a) J_ϕ *norm 3D representation.*

(b) J_z *norm 3D representation.*

Figure 4.2: Spectrum current density components representation for B= 50mT, n= $3 \cdot 10^{17} m^{-3}$, T= 7eV, p= 30mTorr. k_z is the normalised axial wave-number, that is divided by $\frac{2\pi}{L}$.

For the remaining discharge parameters, as a consequence of the previous considerations, only data for m=0 will be analysed and exclusively for J_ϕ spectrum.

In Fig.4.3, it is possible to observe how the electronic temperature does not affect J_ϕ so much. However, for different values of the magnetic field B, for a plasma density n in the order of 10^{17} and for a background pressure p of 30mTorr, the 3eV curve is greater than the 7eV one; conversely, for other values of p or n, as shown in Fig.4.3e,there is no difference at all between the two curves. A similar behaviour, regarding the deposition power, for a particular density interval was noticed in [24].

Fig.4.4 shows how the pressure p does not influence much J_ϕ, although there are some variations according to the temperature and plasma density. For lower values of B, the curve of 7eV emphasizes, better than the 3eV one, the higher maximum value of J_ϕ at a pressure of 1mTorr; this happens only for n belonging to an interval of low values in the order of 10^{17}. Increasing the magnetic field, in Fig.4.4c and Fig.4.4d, there is the same behaviour, even though for higher values of n in the same order of magnitude. A similar trend is reported in [24] regarding the power deposition, but with a direct proportionality between pressure and power.

Fig.4.5 shows two particular cases where B influences a bit J_ϕ: outside this plasma density interval, which will be considered further on, J_ϕ isn't subject to any perturbation. In Fig.4.5a and Fig.4.5b, it is possible to observe that, as B increases up to 50mT, J_ϕ diminishes and then it keeps a constant trend: this happens only in a particular interval of the density plasma, precisely when n$\in [7 \cdot 10^{18} \div 2 \cdot 10^{19}]$; further more, this behaviour returns for every value of the other parameters.

On the other hand, in Fig.4.5c and Fig.4.5d, J_ϕ decreases only for B over than 50mT, without being affected for previous values: this is found when n$\in [3 \cdot 10^{19} \div 4 \cdot 10^{19}]$ and always without restriction regarding the other variables.

The last parameter to analyse is the plasma density, which has the strongest influence, as it has been determined until now.

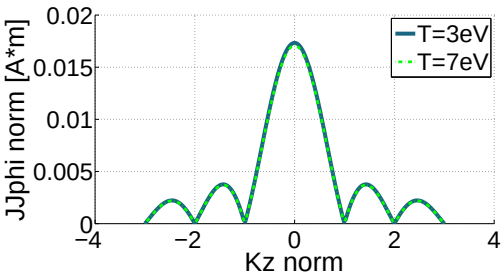

(a) *Spectrum of* J_ϕ *for B=20mT, p=30mTorr, n=7* · $10^{17} m^{-3}$.

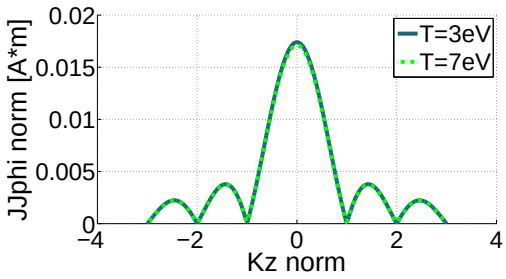

(b) *Spectrum of* J_ϕ *for B=20mT, p=30mTorr, n=8* · $10^{17} m^{-3}$.

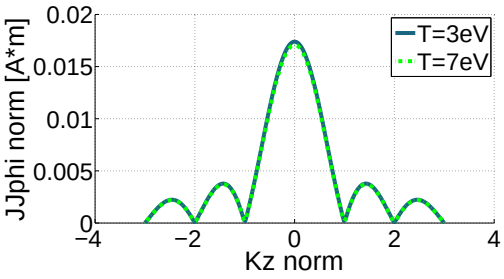

(c) *Spectrum of* J_ϕ *for B=100mT, p=30mTorr, n=8* · $10^{17} m^{-3}$.

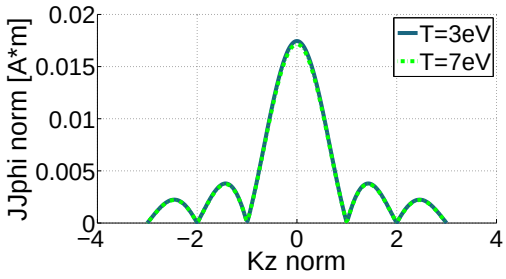

(d) *Spectrum of* J_ϕ *for B=100mT, p=30mTorr, n=9* · $10^{17} m^{-3}$.

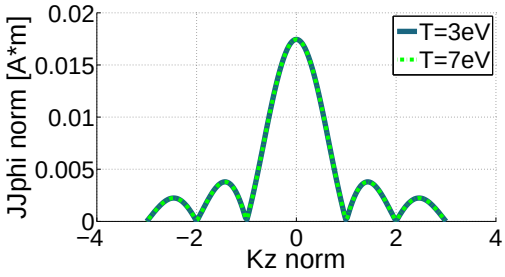

(e) *Spectrum of* J_ϕ *for B=40mT, p=1mTorr, n=6* · $10^{17} m^{-3}$.

Figure 4.3: Spectrum of J_ϕ for a Single-Loop antenna: influence of T.

There have been illustrated two cases of studying about the influence of n: one for B=10mT and the other for B=100mT. Both exhibit a similar trend in certain intervals of the plasma density:

- for n$\sim 10^{16}$ there is no variation even for other combinations of the remaining variables(Fig.4.6a, Fig.4.6b, Fig.4.10a, Fig.4.10b);
- for n$\sim 10^{17}$ J_ϕ presents a 4% increasing as B intensifies (Fig.4.7a, Fig.4.7b, Fig.4.11a, Fig.4.11b);
- for n$\in [1 \div 5] \cdot 10^{18} m^{-3}$ it is possible to detect a growth of J_ϕ equals to 7.5% (Fig.4.8a, Fig.4.12a);
- in Fig.4.8b and Fig.4.12b there is nothing to point out;

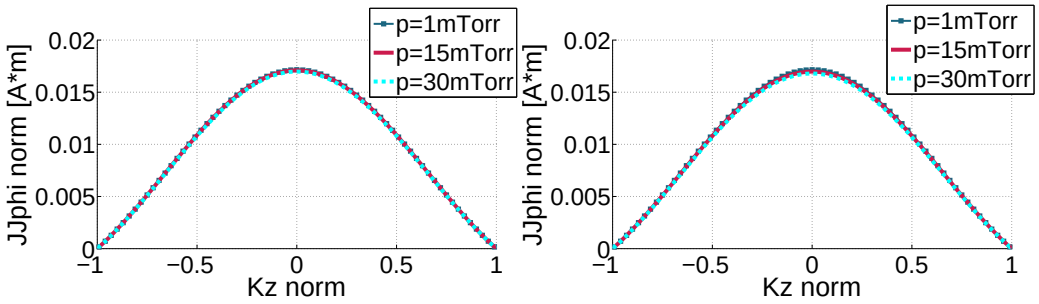

(a) *Spectrum of* J_ϕ *for B=20mT, T=3eV,* $n=3 \cdot 10^{17} m^{-3}$.

(b) *Spectrum of* J_ϕ *for B=20mT, T=7eV,* $n=3 \cdot 10^{17} m^{-3}$.

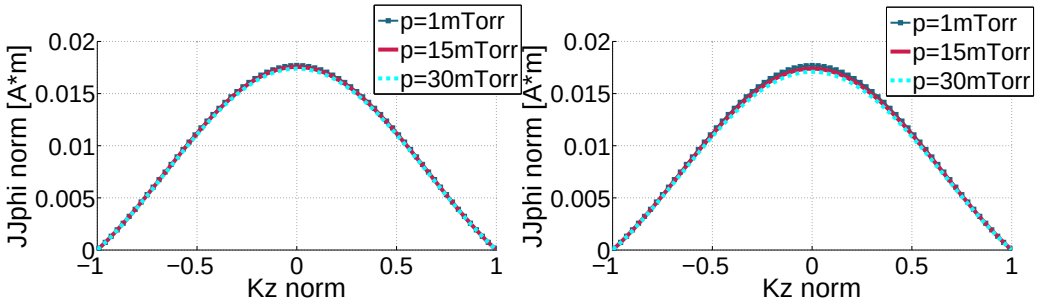

(c) *Spectrum of* J_ϕ *for B=100mT, T=3eV,* $n=8 \cdot 10^{17} m^{-3}$.

(d) *Spectrum of* J_ϕ *for B=100mT, T=7eV,* $n=8 \cdot 10^{17} m^{-3}$.

Figure 4.4: Spectrum of J_ϕ for a Single-Loop Antenna: influence of p.

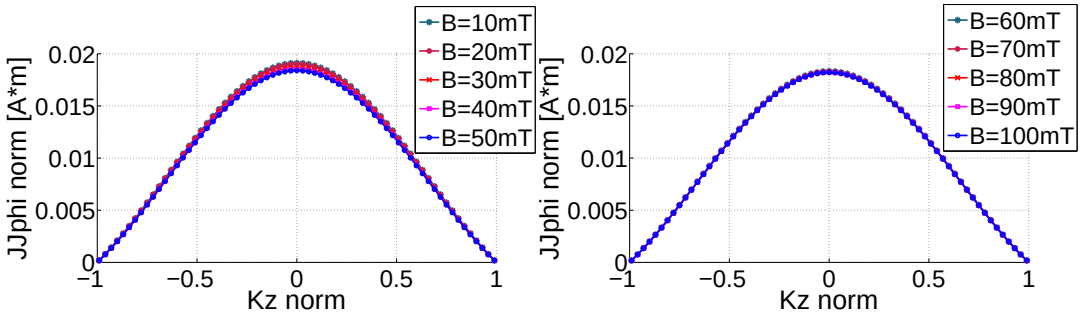

(a) *Spectrum of* J_ϕ *for p=30mTorr, T=3eV,* $n=1 \cdot 10^{19} m^{-3}$.

(b) *Spectrum of* J_ϕ *for p=30mTorr, T=3eV,* $n=1 \cdot 10^{19} m^{-3}$.

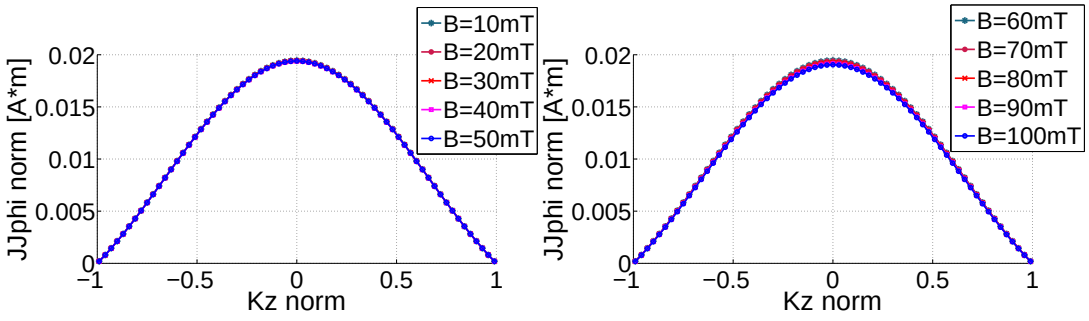

(c) *Spectrum of* J_ϕ *for p=30mTorr, T=3eV,* $n=4 \cdot 10^{19} m^{-3}$.

(d) *Spectrum of* J_ϕ *for p=30mTorr, T=3eV,* $n=4 \cdot 10^{19} m^{-3}$.

Figure 4.5: Spectrum of J_ϕ for a Single-Loop antenna: influence of B.

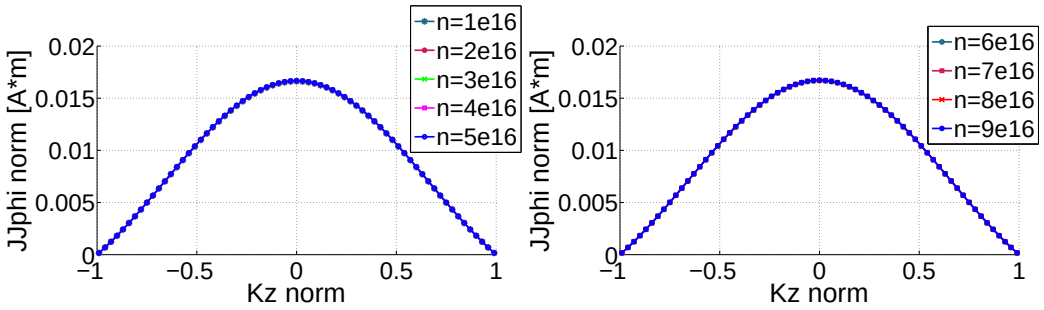

(a) J_ϕ *spectrum.* (b) J_ϕ *spectrum.*

Figure 4.6: Spectrum of J_ϕ for B=10mT, T=3eV, p=30mTorr for a Single-Loop Antenna: influence of n in the range $1 \cdot 10^{16} \div 9 \cdot 10^{16} m^{-3}$.

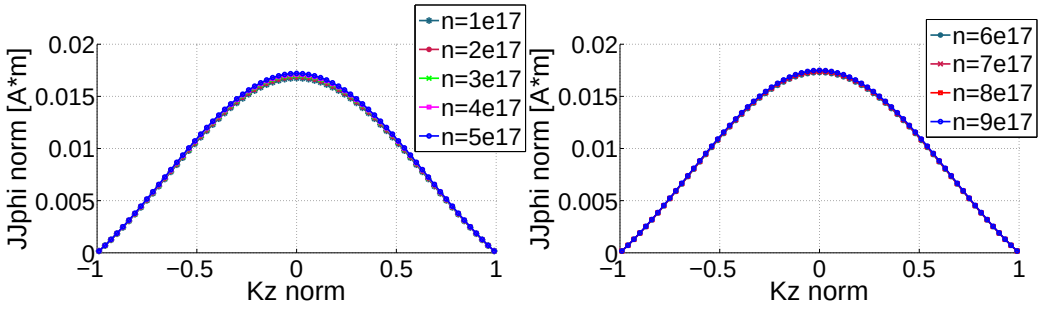

(a) J_ϕ *spectrum.* (b) J_ϕ *spectrum.*

Figure 4.7: Spectrum of J_ϕ for B=10mT, T=3eV, p=30mTorr for a Single-Loop Antenna: influence of n in the range $1 \cdot 10^{17} \div 9 \cdot 10^{17} m^{-3}$.

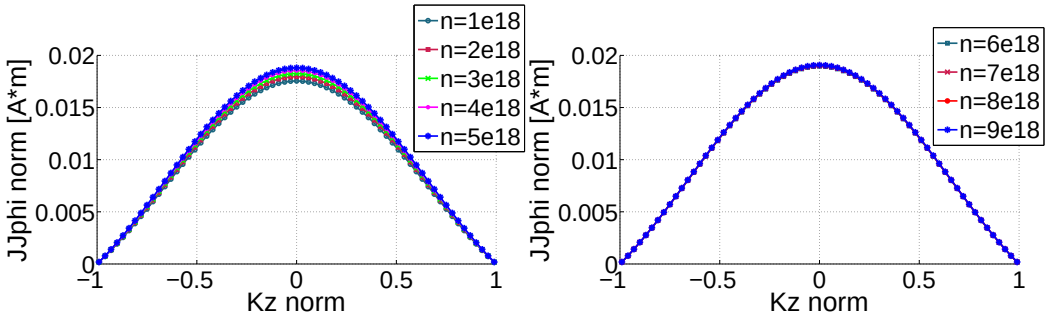

(a) J_ϕ *spectrum.* (b) J_ϕ *spectrum.*

Figure 4.8: Spectrum of J_ϕ for B=10mT, T=3eV, p=30mTorr for a Single-Loop antenna: influence of n in the range $1 \cdot 10^{18} \div 9 \cdot 10^{18} m^{-3}$.

- for $n \sim 10^{19}$ there is a 2% growth of J_ϕ as n increases looking at Fig.4.9, whilst in Fig.4.13 it rises to 6%.

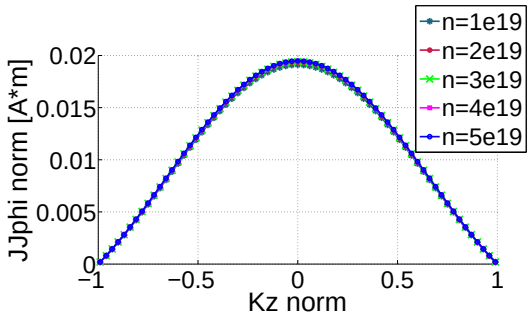

Figure 4.9: Spectrum of J_ϕ for B=10mT, T=3eV, p=30mTorr for a Single-Loop antenna: influence of n in the range $1 \cdot 10^{19} \div 5 \cdot 10^{19} m^{-3}$.

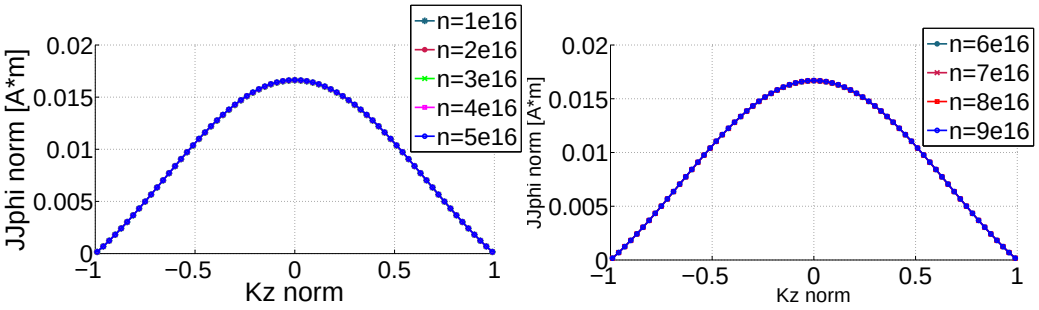

(a) J_ϕ *spectrum.* (b) J_ϕ *spectrum.*

Figure 4.10: Spectrum of J_ϕ for B=100mT, T=3eV, p=30mTorr for a Single-Loop antenna: influence of n in the range $1 \cdot 10^{16} \div 5 \cdot 10^{16} m^{-3}$.

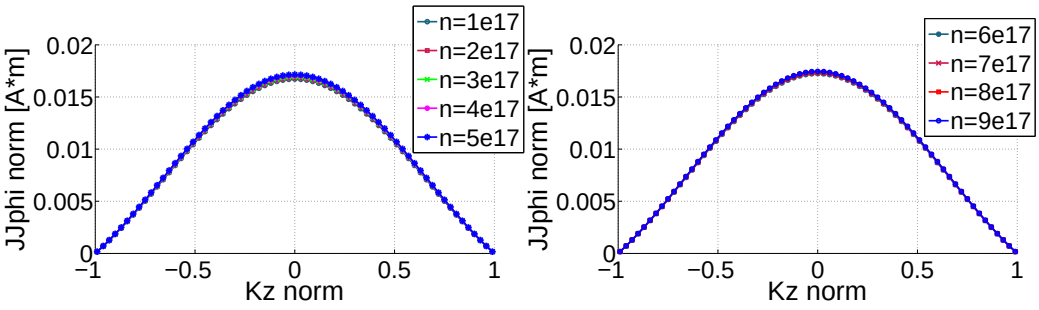

(a) J_ϕ *spectrum.* (b) J_ϕ *spectrum.*

Figure 4.11: Spectrum of J_ϕ for B=100mT, T=3eV, p=30mTorr for a Single-Loop antenna: influence of n in the range $1 \cdot 10^{17} \div 5 \cdot 10^{17} m^{-3}$.

All in all, the general conclusion is that J_ϕ grows as n increases, in contradiction with what observed in [24] concerning the influence of n on the plasma deposition power.

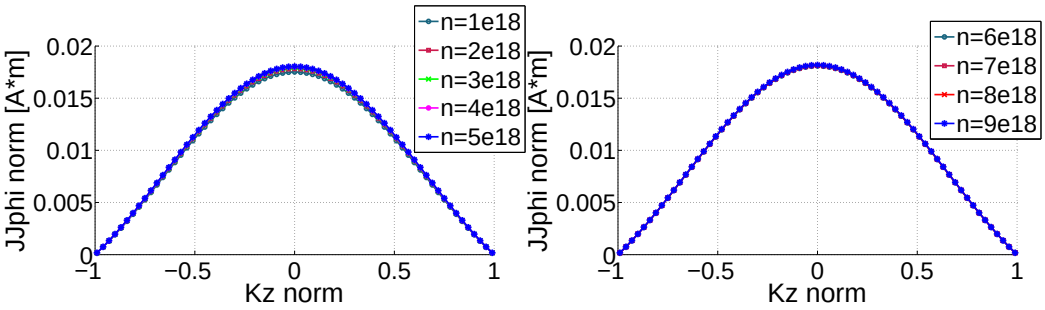

(a) J_ϕ *spectrum.* (b) J_ϕ *spectrum.*

Figure 4.12: Spectrum of J_ϕ for B=100mT, T=3eV, p=30mTorr for a Single-Loop antenna: influence of n in the range $1 \cdot 10^{18} \div 5 \cdot 10^{18} m^{-3}$.

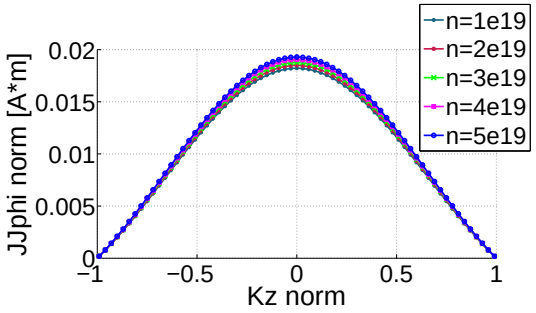

Figure 4.13: Spectrum of J_ϕ for B=100mT, T=3eV, p=30mTorr for a Single-Loop antenna:influence of n in the range $1 \cdot 10^{19} \div 5 \cdot 10^{19} m^{-3}$.

4.2 NAGOYA

As explained for the Loop case, in Fig.4.14 it is possible to summarize the general trend of J_ϕ and J_z for every combination of parameters.

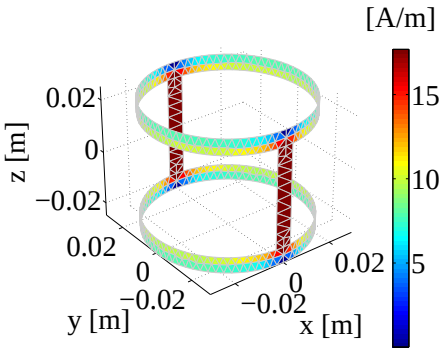

Figure 4.14: Nagoya Mesh and current density distribution for B= 40mT, n= $1 \cdot 10^{18} m^{-3}$, T= 3eV, p= 15mTorr.

In Fig.4.14, $\vec{J}$ reaches its maximum value along the longitudinal links; furthermore it maintains a higher magnitude in the inner side of the two loops. The latter behaviour could justify why in Fig.4.15a there are contributions for

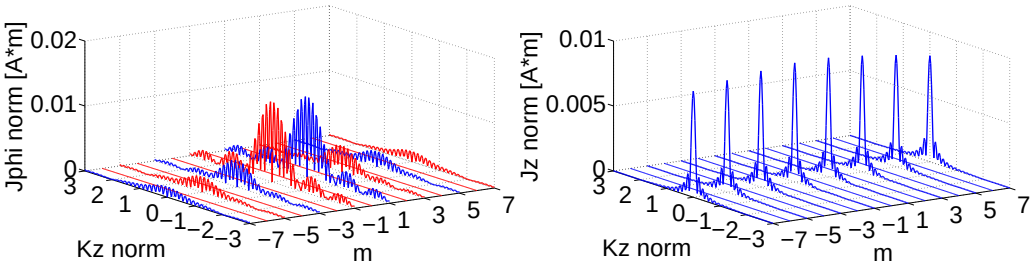

(a) J_ϕ *norm 3D plot* (b) J_z *norm 3D plot*

Figure 4.15: Current density spectrum components representation for a Nagoya III antenna for B= 40mT, n= $1 \cdot 10^{18} m^{-3}$, T= 3eV, p= 15mTorr. k_z is the normalised axial wave-number, that is divided by $\frac{2\pi}{L}$.

J_ϕ only for odd m, with interesting values also for $m = \pm 7$. In closing, in Fig. 4.15b, J_z is comparable with J_ϕ because of the two longitudinal bridges.

For the next discharge parameters, as a consequence of the previous considerations, only data for odd m up to 7 will be analysed, both for J_ϕ and J_z: since the evident symmetry along m, only its positive values will be analysed.

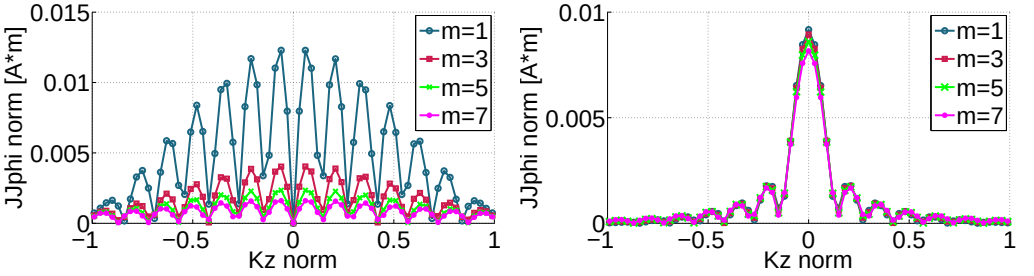

(a) J_ϕ *plot for m comparison.* (b) J_z *plot for m comparison.*

Figure 4.16: J_ϕ and J_z comparison between m modes for B= 100mT, n= $8 \cdot 10^{16} m^{-3}$, T= 3eV, p= 30mTorr of a Nagoya III antenna.

It is important to compare the curves obtained for each excitation mode m, in order to understand whether, further on, there will be a relation between the intensity of the spectrum and the plasma power deposition: in Fig4.16, it is possible to see that already with m=3 there is a drop of the 70% up to 85% for m=7. Moreover, the period of the curves increases as m does the same. Conversely, in Fig.4.16b, there is a regular decrease of J_z up to 15% for m=7. This general trend is maintained for every combination of parameters, hence the decision to illustrate only two pictures.

In Fig.4.17, it is easy to see how the electron temperature T does not affect J_ϕ and this is valid for each excitation mode. Looking at all possible combination of other parameters, it was impossible to notice other kinds of dependence: J_ϕ follows the same trend of the plasma deposition power as described in [24]. In Fig.4.18, nothing changes compared to J_ϕ behaviour but still it has to be

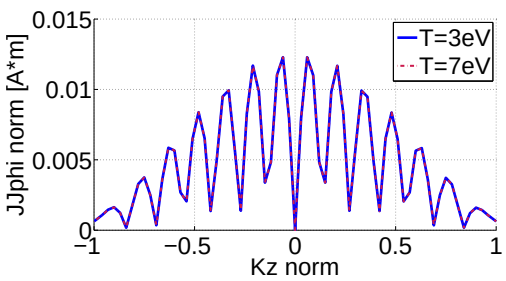

(a) *Spectrum of* J_ϕ *for B=100mT, p=15mTorr, n=5* · $10^{17}\,m^{-3}$ *with m=1.*

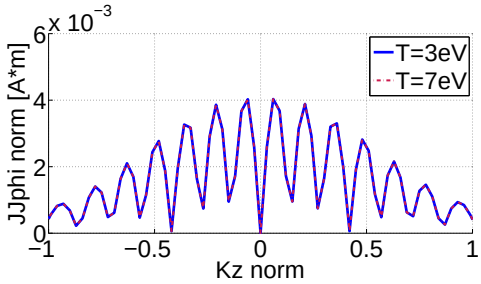

(b) *Spectrum of* J_ϕ *for B=100mT, p=15mTorr, n=5* · $10^{17}\,m^{-3}$ *with m=3.*

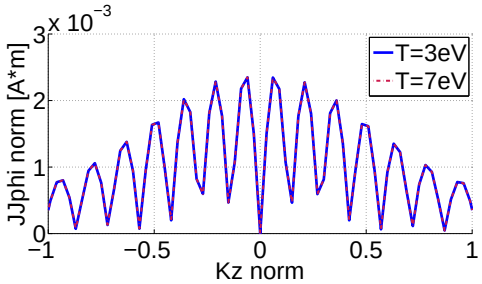

(c) *Spectrum of* J_ϕ *for B=100mT, p=15mTorr, n=5* · $10^{17}\,m^{-3}$ *with m=5.*

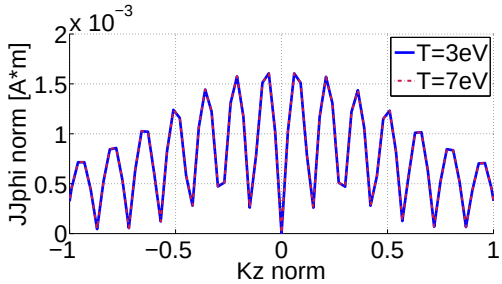

(d) *Spectrum of* J_ϕ *for B=100mT, p=15mTorr, n=5* · $10^{17}\,m^{-3}$ *with m=7.*

Figure 4.17: Spectrum of J_ϕ for a Nagoya III antenna: influence of T.

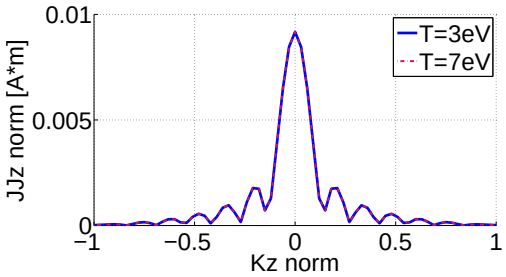

(a) *Spectrum of* J_z *for B=100mT, p=15mTorr, n=5* · $10^{17}\,m^{-3}$ *with m=1.*

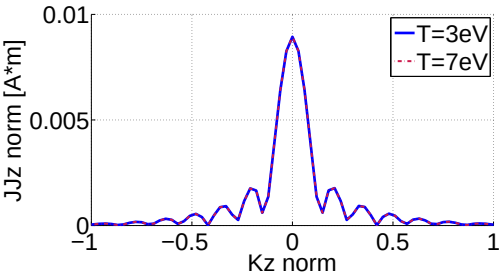

(b) *Spectrum of* J_z *for B=100mT, p=15mTorr, n=5* · $10^{17}\,m^{-3}$ *with m=3.*

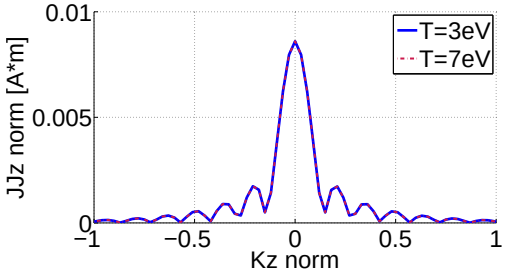

(c) *Spectrum of* J_z *for B=100mT, p=15mTorr, n=5* · $10^{17}\,m^{-3}$ *with m=5.*

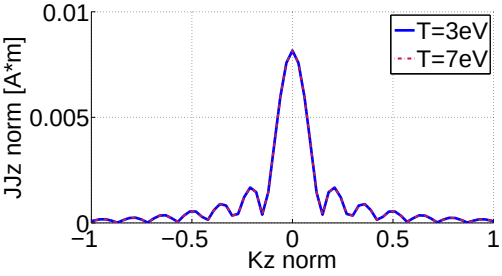

(d) *Spectrum of* J_z *for B=100mT, p=15mTorr, n=5* · $10^{17}\,m^{-3}$ *with m=7.*

Figure 4.18: Spectrum of J_z for a Nagoya III antenna: influence of T.

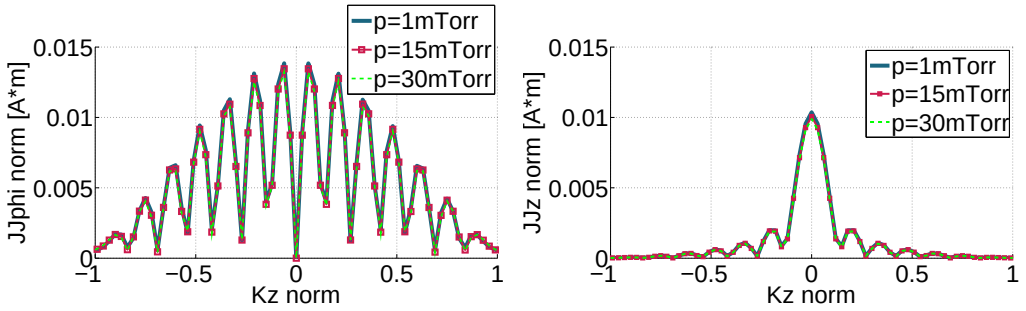

(a) *Spectrum of* J_ϕ *for B=20mT, T=7eV, n=4* $\cdot 10^{18} m^{-3}$.

(b) *Spectrum of* J_z *for B=20mT, T=7eV, n=4* $\cdot 10^{18} m^{-3}$.

Figure 4.19: Spectrum of J_ϕ and J_z for a Nagoya III antenna: influence of p.

highlighted the fact that there are important contributions also for m equals to 5 or 7.

In Fig.4.19, it is clear that there is no particular relation between the spectral variables and the pressure p: a slight drop with the pressure is underlined when the magnetic field is low and when the plasma density n belongs to the interval of $[3 \div 7] \cdot 10^{18} m^{-3}$. As for the remaining cases, J_ϕ and J_z do not change. The curves for the other excitation modes are not presented since they give the same information as those for m=1 do.

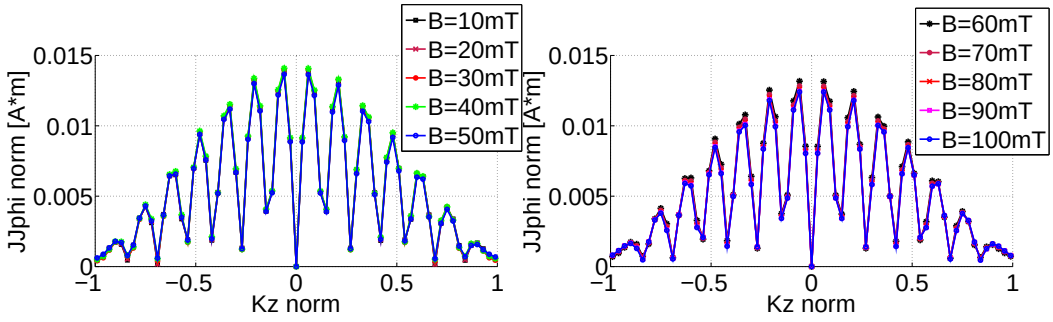

(a) *Spectrum of* J_ϕ *for p=1mTorr, T=3eV, n=1* $\cdot 10^{19} m^{-3}$.

(b) *Spectrum of* J_ϕ *for p=1mTorr, T=3eV, n=1* $\cdot 10^{19} m^{-3}$.

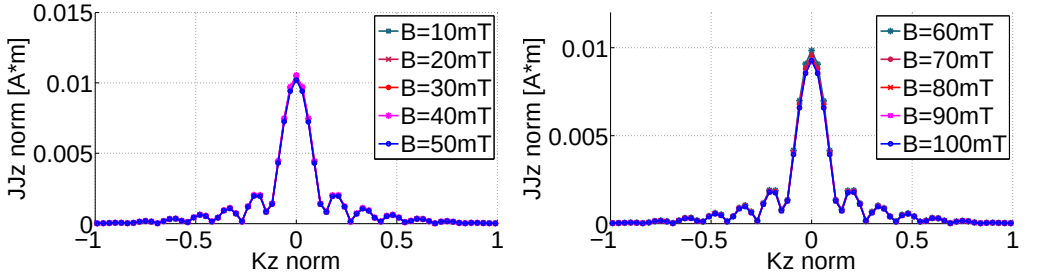

(c) *Spectrum of* J_z *for p=1mTorr, T=3eV, n=1* $\cdot 10^{19} m^{-3}$.

(d) *Spectrum of* J_z *for p=1mTorr, T=3eV, n=1* $\cdot 10^{19} m^{-3}$.

Figure 4.20: Spectrum of J_ϕ and J_z for a Nagoya III antenna: influence of B.

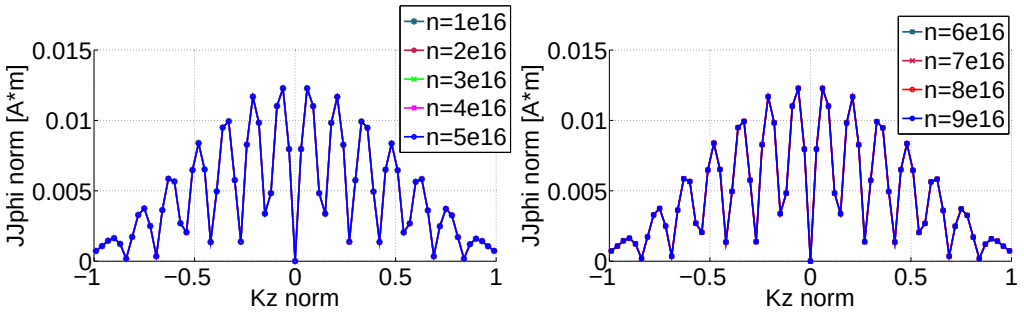

(a) J_ϕ *spectrum.* (b) J_ϕ *spectrum.*

Figure 4.21: Spectrum of J_ϕ for B=20mT, T=7eV, p=1mTorr for a Nagoya III antenna: influence of n in the range $1 \cdot 10^{16} \div 9 \cdot 10^{16} m^{-3}$.

In [24], the deposition power for a Nagoya antenna does not change with the magnetic field B: the same affirmation can be done for both J_ϕ and J_z spectrum. In Fig.4.20 it is possible to notice a slight variation which recurs when the plasma density $n \in [3 \div 10] \cdot 10^{18} m^{-3}$: in detail, there is a maximum for B=40mT and this is valid for every combination of the remaining parameters and for both components of the spectrum.

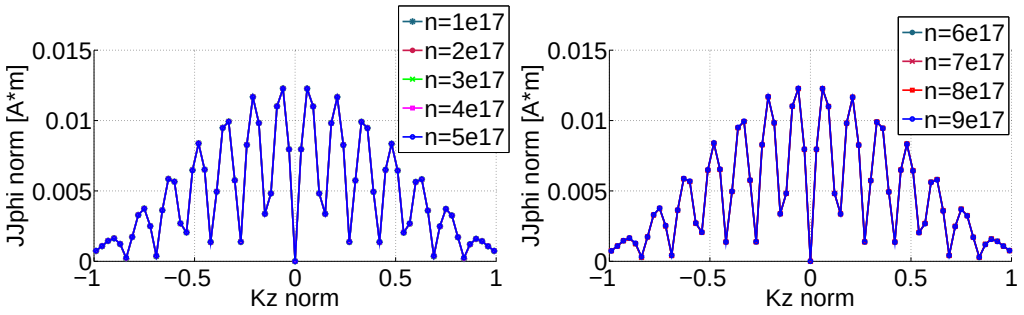

(a) J_ϕ *spectrum.* (b) J_ϕ *spectrum.*

Figure 4.22: Spectrum of J_ϕ for B=20mT, T=7eV, p=1mTorr for a Nagoya III antenna: influence of n in the range $1 \cdot 10^{17} \div 9 \cdot 10^{17} m^{-3}$.

Observing all the figures about the plasma density n, it is possible to see that J_ϕ is subjected to a slow growth as n increases. However, when the pressure is 1mTorr and the magnetic intensity field is 20mT, it should be easy to observe these characteristics about J_ϕ and J_z:

- for $n \sim 10^{16}$ or $n \sim 10^{17}$ there is no variation even for other combinations of the remaining variables(Fig.4.21a, Fig.4.21b, Fig.4.22a, Fig.4.22b, Fig.4.25a, Fig.4.25b, Fig.4.26a, Fig.4.26b);
- for $n \in [1 \div 5] \cdot 10^{18} m^{-3}$ it is possible to see a 15% growth of J_ϕ and J_z(Fig.4.8a, Fig.4.12a);
- in Fig.4.23b and Fig.4.27b, it can be noticed how the previous increasing stops, leaving space to a decreasing until reaching a stable value for $n \sim 10^{19} m^{-3}$(Fig.4.24 and Fig.4.28).

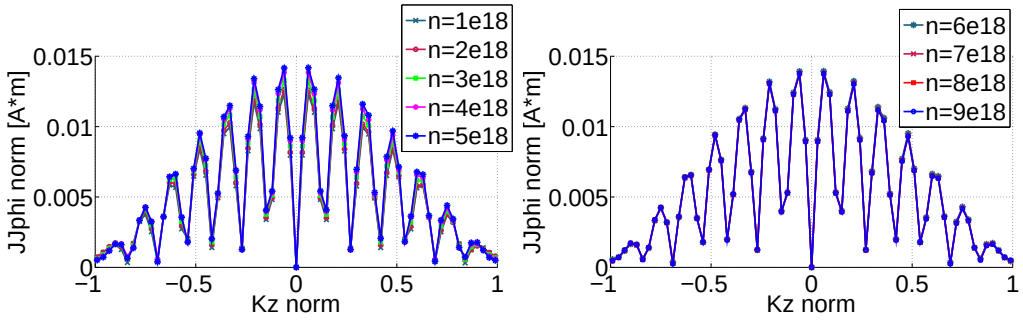

(a) J_ϕ *spectrum.* (b) J_ϕ *spectrum.*

Figure 4.23: Spectrum of J_ϕ for B=20mT, T=7eV, p=1mTorr for a Nagoya III antenna: influence of n in the range $1 \cdot 10^{18} \div 9 \cdot 10^{18} m^{-3}$.

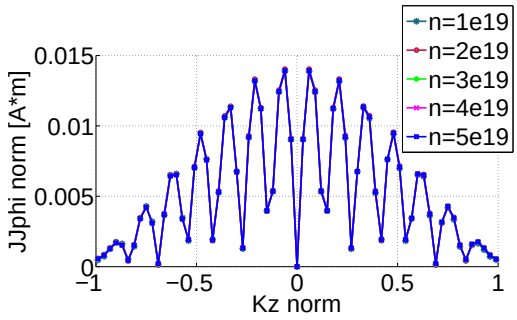

Figure 4.24: Spectrum of J_ϕ for B=20mT, T=7eV, p=1mTorr of a Nagoya III antenna:influence of n in the range $1 \cdot 10^{19} \div 5 \cdot 10^{19} m^{-3}$.

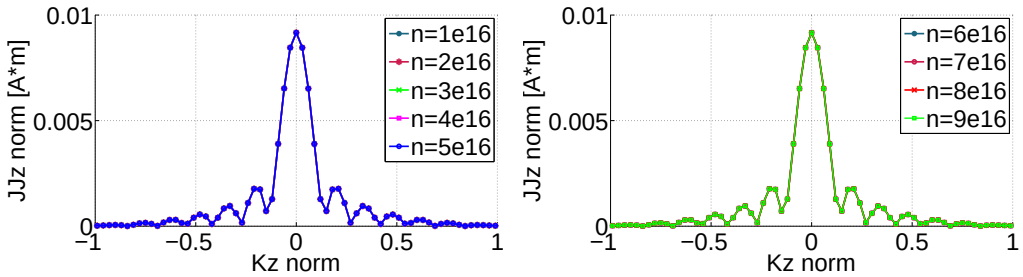

(a) J_z *spectrum.* (b) J_z *spectrum.*

Figure 4.25: Spectrum of J_z for B=20mT, T=7eV, p=1mTorr for a Nagoya III antenna: influence of n in the range $1 \cdot 10^{16} \div 9 \cdot 10^{16} m^{-3}$.

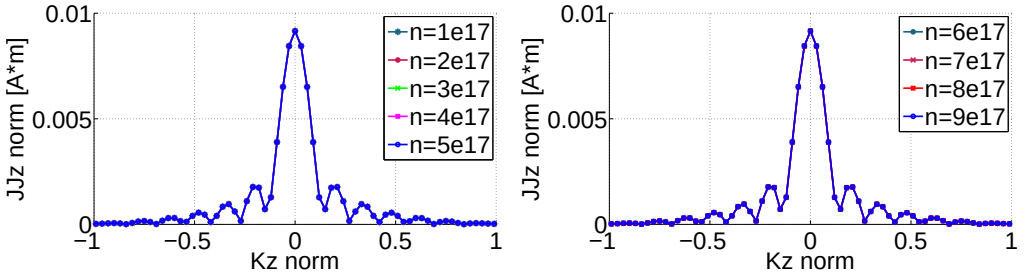

(a) J_z *spectrum.* (b) J_z *spectrum.*

Figure 4.26: Spectrum of J_z for B=20mT, T=7eV, p=1mTorr for a Nagoya III antenna: influence of n in the range $1 \cdot 10^{17} \div 9 \cdot 10^{17} m^{-3}$.

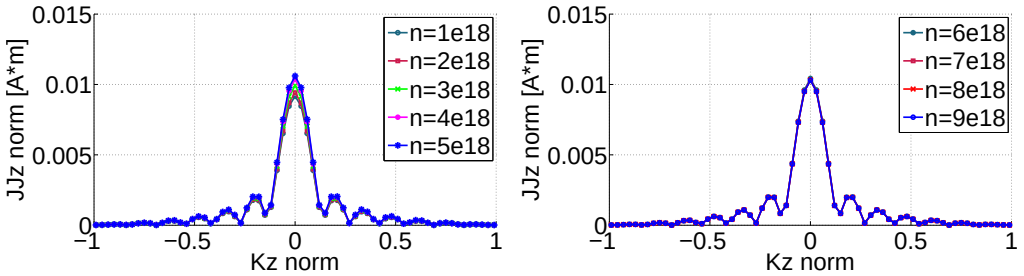

(a) J_z *spectrum.* (b) J_z *spectrum.*

Figure 4.27: Spectrum of J_z for B=20mT, T=7eV, p=1mTorr for a Nagoya III antenna: influence of n in the range $1 \cdot 10^{18} \div 9 \cdot 10^{18} m^{-3}$.

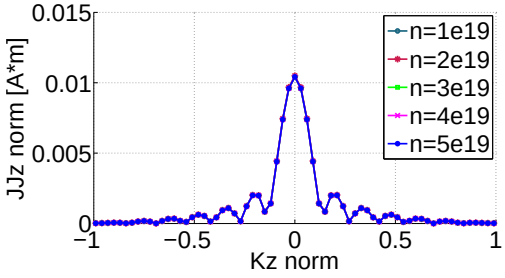

Figure 4.28: Spectrum of J_z for B=20mT, T=7eV, p=1mTorr for a Nagoya III antenna:influence of n in the range $1 \cdot 10^{19} \div 5 \cdot 10^{19} m^{-3}$.

4.3 FRACTIONAL HELIX

In Fig.4.29-4.30, there is a general example of the results obtained for an Fractional Helix antenna: as for the previous cases, this figure represents the general output determined by the code.

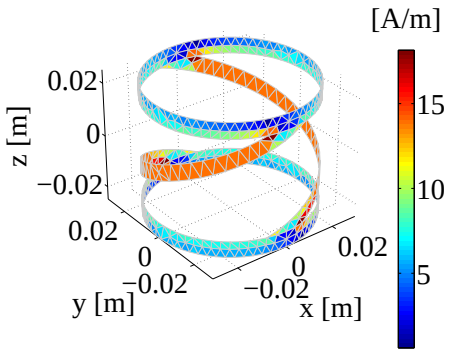

Figure 4.29: Fractional Helix mesh and current density distribution for B= 20mT, n= $1 \cdot 10^{17} m^{-3}$, T= 7eV, p= 15mTorr.

Fig.4.29 shows the distribution of the current density $\vec{J}$: it has its maximum along the helical links and, as for the Nagoya antenna, it maintains an higher magnitude in the inner side of the two loops. It is evident how the curves, in Fig.4.30a and Fig.4.30b, are not symmetric any more respect to the excitation mode m: thanks to Fig.4.31, it is possible to confirm that this is an effect caused by only the geometry of the antenna and not by the magnetic field B.

For the next discharge parameters, as a consequence of the previous considerations, only data for odd m up to 5 will be analysed, both for J_ϕ and J_z.

In Fig4.32, it is possible to see that with m=3 there is a drop of the 30% up to 50% for m=5. Moreover, the single curves are not symmetric to the longitudinal wave-number K_z too. On the other hand, in Fig.4.32b there is a regular decrease of J_z, from 10% for m=3 up to 35% for m=5. Since the curves for m positive are specular to the negative ones, it is easier to report only the results for m=1

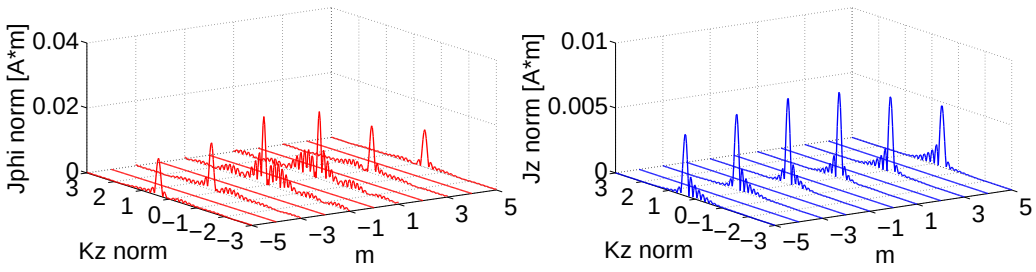

(a) J_ϕ *norm 3D plot.*

(b) J_z *norm 3D plot.*

Figure 4.30: Current density spectral components representation of a Fractional Helix antenna for B= 20mT, n= $1 \cdot 10^{17} m^{-3}$, T= 7eV, p= 15mTorr. k_z is the normalised axial wave-number, that is divided by $\frac{2\pi}{L}$.

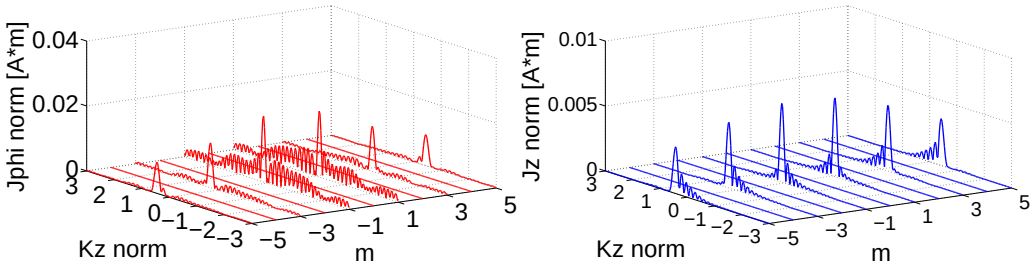

(a) J_ϕ *norm 3D plot.* (b) J_z *norm 3D plot.*

Figure 4.31: J_ϕ and J_z spectrum from general simulation without magnetic field of a Fractional Helix antenna.

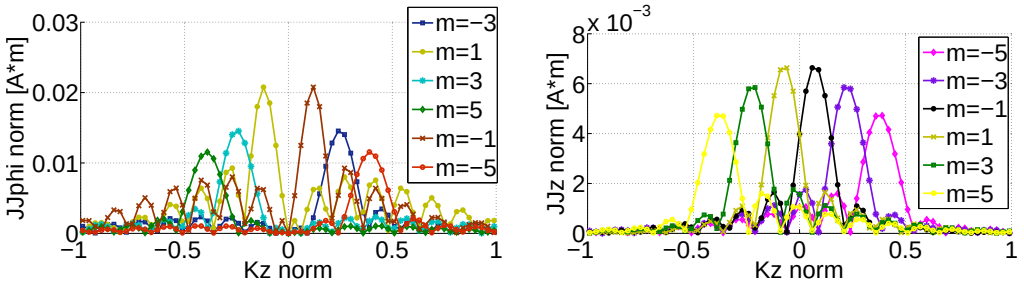

(a) J_ϕ *comparison.* (b) J_z *comparison.*

Figure 4.32: J_ϕ and J_z comparison between m modes for B= 20mT, n= $7 \cdot 10^{17} m^{-3}$, T= 7eV, p= 30mTorr of a Fractional Helix antenna.

in the following analysis: the variation on a certain excitation mode m are the same for the others, therefore the results are no shown.

Although until now the electron temperature has proved to be a minor factor of influence on the spectrum, it is right to report at least an example.

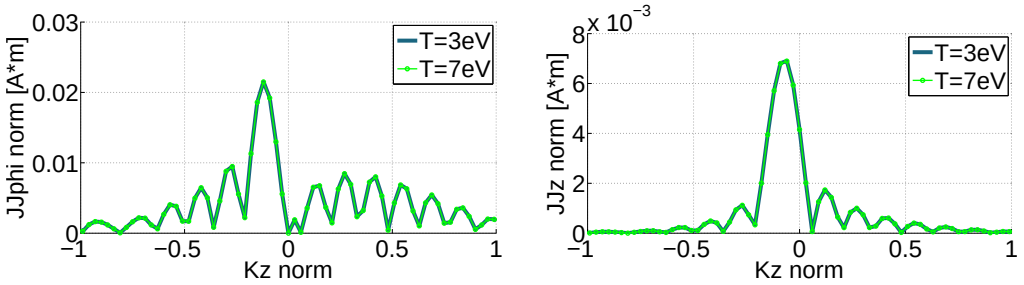

(a) *Spectrum of* J_ϕ *for B=20mT, p=15mTorr, n=6* $\cdot 10^{18} m^{-3}$ *with m=1.* (b) *Spectrum of* J_z *for B=20mT, p=15mTorr, n=6* $\cdot 10^{18} m^{-3}$ *with m=1.*

Figure 4.33: J_ϕ and J_z spectrum for a Fractional Helix antenna: influence of T.

As expected, from Fig.4.33, it is clear that the effect of the electron temperature is negligible and this is true for all the parameters considered.

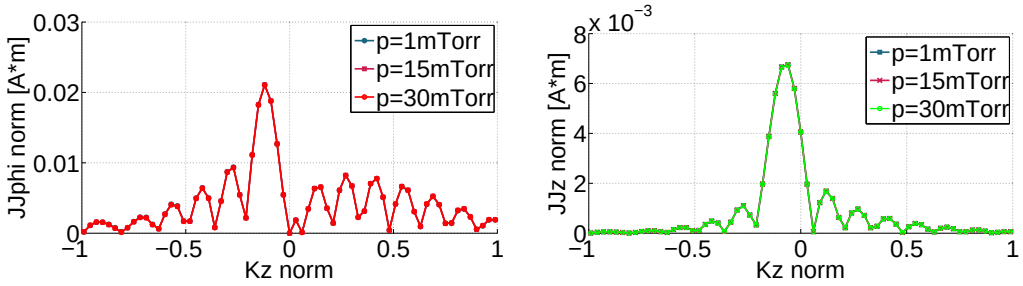

(a) *Spectrum of* J_ϕ *for B=20mT, T=7eV, n=3* · $10^{18} m^{-3}$. (b) *Spectrum of* J_z *for B=20mT, T=7eV, n=3* · $10^{18} m^{-3}$.

Figure 4.34: Spectrum of J_ϕ and J_z for a Fractional Helix antenna: influence of p.

Fig.4.34, shows how there is no relation between the neutral background pressure and J_ϕ or J_z: this comment can be extended to the remaining cases.

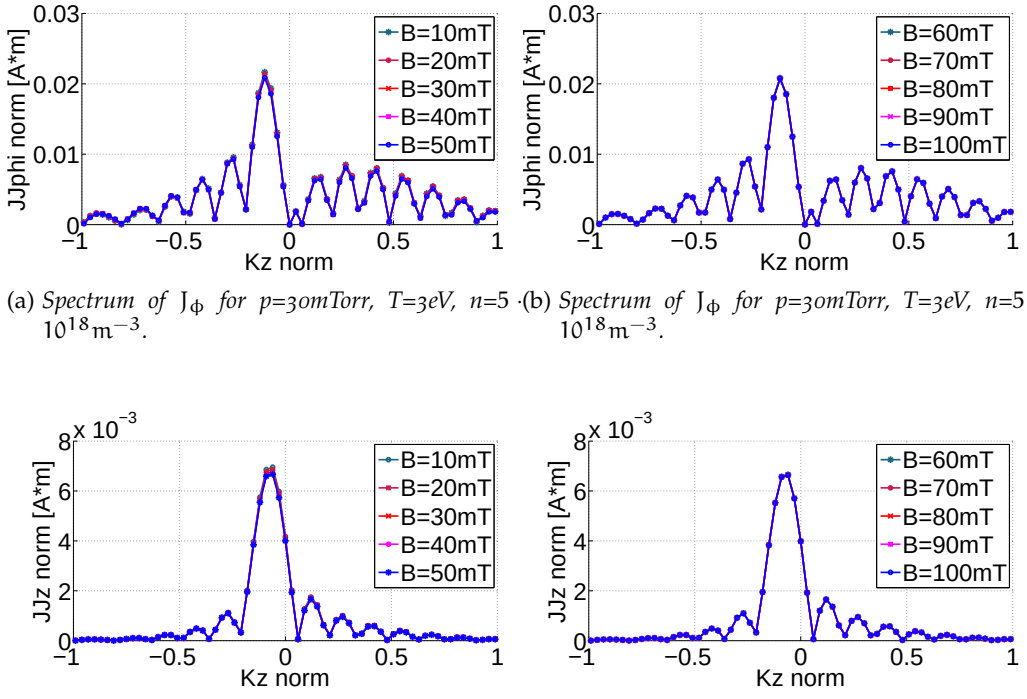

(a) *Spectrum of* J_ϕ *for p=30mTorr, T=3eV, n=5* · $10^{18} m^{-3}$. (b) *Spectrum of* J_ϕ *for p=30mTorr, T=3eV, n=5* · $10^{18} m^{-3}$.

(c) *Spectrum of* J_z *for p=30mTorr, T=3eV, n=5* · $10^{18} m^{-3}$. (d) *Spectrum of* J_z *for p=30mTorr, T=3eV, n=5* · $10^{18} m^{-3}$.

Figure 4.35: Spectrum of J_ϕ and J_z for a Fractional Helix antenna: influence of B.

Analysing all the plots obtained with the code, it is possible to affirm that, generally, there is no correlation between the magnetic field B and the spectrum of the current density. In Fig.4.35, an exception is reported since there is a decreasing as B increases when the plasma density is in the range of $10^{18} m^{-3}$. This trend is visible in Fig.4.35a and Fig.4.35c, where only magnetic field values

up to 50mT are considered; for higher values the curves do not change as it seems they found a kind of stability.

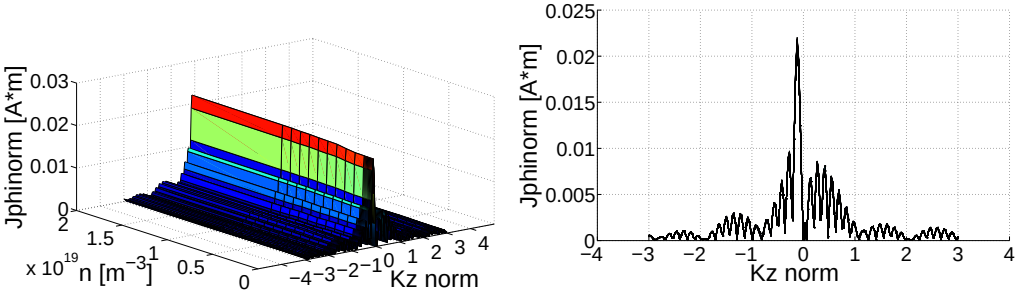

(a) *3D* J_ϕ *spectrum for B=20mT, T=3eV, p=1mTorr.* (b) J_ϕ *spectrum projected to the X-Z plane for B=20mT, T=3eV, p=1mTorr.*

Figure 4.36: 3D Spectrum of J_ϕ with X-Z projection in relation to n for a Fractional Helix antenna.

It is fruitless to report the 2D representation of the influence of the plasma density on J_ϕ and J_z: from those pictures, it would appear there is no variation with n. Conversely, Fig.4.36 and Fig.4.37 show how there is a small but constant growth of the spectrum along the plasma density, without any maximum value found as happened for the Nagoya antenna: specifically, through Fig.4.36b and Fig.4.37b it is possible to notice a total growth of 5%.

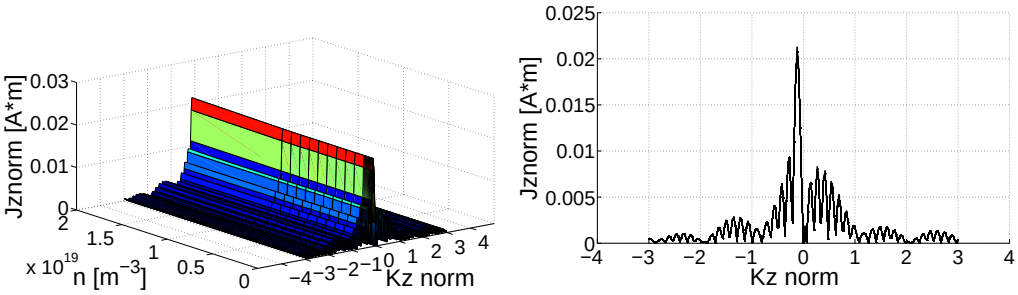

(a) *3D* J_z *spectrum for B=20omT, T=3eV, p=1mTorr.* (b) J_z *spectrum projected to the X-Z plane for B=20omT, T=3eV, p=1mTorr.*

Figure 4.37: 3D Spectrum of J_z with the X-Z projection in relation to n for a Fractional Helix antenna.

4.4 COMPARISON AGAINST ANALYTICAL RESULTS

In this section, there is the intent to compare the spectra obtained with the code with the ones used by Chen[12] to analyse the plasma problem through the HELIC code.

The aim is to understand if modelling an antenna with surfaces leads to current density spectrum different than that obtained through the thin-wire

hypothesis, calling, therefore, into question the reasoning about the studies on HPS conducting so far.

4.4.1 *Single-Loop*

It is meaningless to compare the data derived by the Single-Loop configuration since the spectrum obtained with the code is represented, as an example, in Fig.4.3a; on the other hand, not considering the width w of the antenna leads to a constant spectrum.

The difference is obvious and only the following analysis can make us understand how it can influence the power deposition into the plasma.

4.4.2 *Nagoya*

Since Chen[12] considered the thin-wire hypothesis, a constant magnitude of the current density was considered. For this reason, the analytical formula obtained for the Nagoya case is the Eq.2.3 with $\theta = 0$ since the axial links are straight and they do not twist.

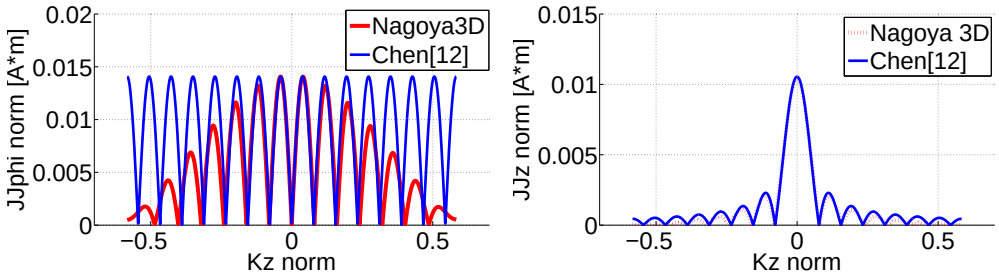

(a) J_ϕ *comparison with Chen[12] analytical formula with m=+1 for the Nagoya case.*

(b) J_z *comparison with Chen[12] analytical formula with m=+1 for the Nagoya case.*

Figure 4.38: Spectrum comparison with Chen's analytical formula with m=+1 for the Nagoya case.

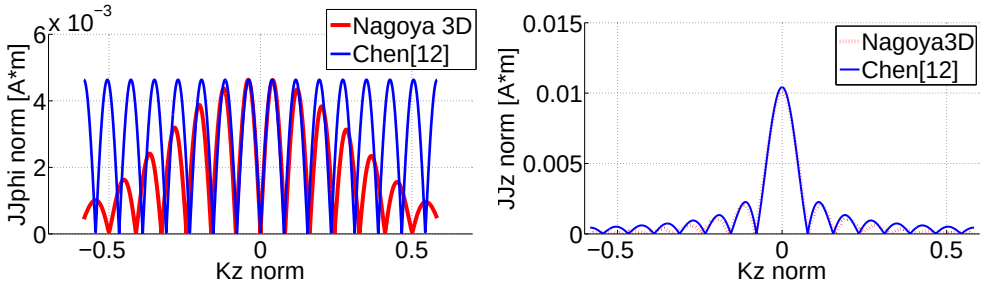

(a) J_ϕ *comparison with Chen[12] analytical formula with m=+3 for the Nagoya case.*

(b) J_z *comparison with Chen[12] analytical formula with m=+3 for the Nagoya case.*

Figure 4.39: Spectrum comparison with Chen's analytical formula with m=+3 for the Nagoya case.

In Fig.4.38 and Fig.4.39, there is a direct comparison between the reference curve and the one obtained by the code.

As concerns J_ϕ, it is evident how the functions are different, although the period is almost the same.

On the other hand, for J_z we must remember the solenoidal condition of this problem, that is $\vec{\nabla} \cdot \vec{J} = 0$, which leads to Eq.2.2: in this case, the two curves are almost coincident although the spectrum predicted by our approach decays faster than the reference one.

4.4.3 *Fractional Helix*

In the Fractional Helix instance, in the Eq.2.3, $\theta = \frac{\pi}{2}$ and this does not allow the elimination of the *sinc* factor as happened for the Nagoya III. In Fig.4.40

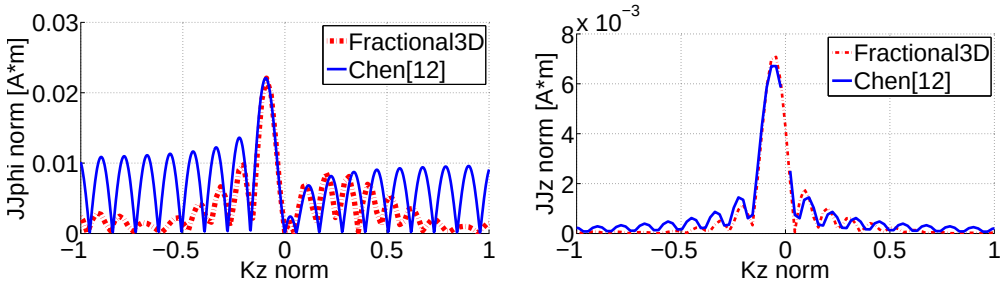

(a) J_ϕ *comparison with Chen[12] analytical formula with m=+1 for the Fractional Helix case.*

(b) J_z *comparison with Chen[12] analytical formula with m=+1 for the Fractional Helix case.*

Figure 4.40: Spectrum comparison with Chen's analytical formula with m=+1 for the Fractional Helix case.

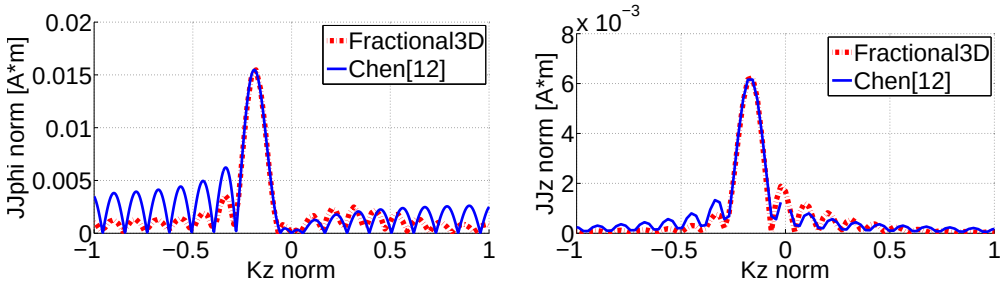

(a) J_ϕ *comparison with Chen[12] analytical formula with m=+3 for the Fractional Helix case.*

(b) J_z *comparison with Chen[12] analytical formula with m=+3 for the Fractional Helix case.*

Figure 4.41: Spectrum comparison with Chen's analytical formula with m=+3 for the Fractional Helix case.

and Fig.4.41, J_ϕ and J_z comparisons are represented for m=+1 and m=+3.

The behaviour for J_ϕ and J_z from both the methods are similar: there is a little difference in the period of the functions and the secondary amplitudes are higher for the curve obtained through the Chen's way.

4.5 CONCLUSIONS

Among the discharge parameters, the background pressure and the electron temperature are those which do not effect much either the real part of the antenna input impedance (which is related to the power deposition) or the spectral functions.

It must be said that there are variations in the same range of magnetic field intensity or plasma density for both the studies: the difference is emphasised when the analysis regards the antenna input impedance. Indeed, all the spectral plots for all the configurations had been magnified in order to highlight the 5% growth observed in certain cases.

This was predictable, though, since the voltage gap is the same for all the combinations of discharge parameters used for the analysis. The intensity of the antenna current density function does not vary drastically, as suggested in [24] (there is fluctuation of $\approx$ 10%) and the distribution is not uniform but neither arbitrary: the consequence is that only a variation on the intensity of the spectral functions could be expected.

Of course, the non uniform current led us to expect new azimuthal modes of excitation or difference in the phase with respect to the spectral functions used by Chen[12] for his analysis with the HELIC code.

For the Single-Loop, it must be said that a constant value was used for the HELIC code, while Eq.(3.4), which considers the surface of the antenna, is a complete different function.

A huge difference appears also for the Nagoya III case as visible in Fig.4.38a: it must be said though that in an interval near to $k_z = 0$ the two functions are close.

Finally, in the Fractional Helix antenna, the spectral functions derived in the two ways are really similar for k_z corresponding to the J_ϕ peak. Then, the effect of not considering the length w of the loops is evident looking at the high secondary oscillations respect to the ones which consider the whole geometry (Fig.4.40a.

In closing, the assumption of the current density as a solenoidal function is confirmed by all the comparisons in the plots which are related to J_z.

5

RADIAL POWER DEPOSITION

In this chapter, the radial power deposition profile into the plasma is the second variable to compare for the two approaches.

With the old one, the current was imposed constant and uniform on a thin-wire antenna; hence, the result is a global radial power deposition profile.

Thanks to the new approach, the complex spectral function of an antenna current density is available: through the SPIREs code, it is possible to analyse this variable considering only particular values for a specific $m - k_z$ pair. In this way it is possible to understand which azimuthal-axial excitation mode plays a major role in the power deposition into the plasma.

Before doing that, there is a brief introduction about the equations which govern the electromagnetic problem in order to understand which are the parameters that limit the spectral contribution for the power deposition into the plasma.

Successively, the radial power profiles of the three antennas considered until now are analysed and compared to each other: this is possible since the problem is transferred to the spectral domain and not in the geometrical one.

In this way it is possible to locate an ideal spectral function trend for a particular set of $m - k_z$: these considerations will lead to the next chapter with the analysis of new antenna configurations.

5.1 ELECTROMAGNETIC PROBLEM

In this section, the aim is to define the limits in which the waves propagate in the plasma: these constraints are linked to the axial wave number k_z.

The procedure is explained in AppendixB, in which the following hypothesis are considered:

- the electromagnetic fields are assumed to vary as $e^{i\,(m\theta + k_z\, z + w t)}$;
- the z axis is aligned with the dc magnetic field;
- the magnetic viscosity and the pressure terms are omitted from the electron fluid equation of motion;
- the ion motions are neglected;
- the displacement current is neglected.

In this way it is possible to determine the dispersion relation which can be factored into the following equation:

$$(\beta_1 - \vec{\nabla}\times)(\beta_2 - \vec{\nabla}\times)\vec{B} = 0 \tag{5.1}$$

with β_1 and β_2 the roots of

$$\delta\beta^2 - k_z\beta + k_w^2 = 0 \tag{5.2}$$

where k_w is the wave number of low-frequency whistler waves propagating along the magnetic field in free space.

It is possible to rearrange Eq.(B.21) as $k_z = \frac{\delta}{\beta}(\beta^2 + k_s^2)$; deriving it, the maximum and minimum value of the axial wave number k_z are determined:

$$k_{z\,min} = 2\delta k_s \tag{5.3}$$

$$k_{z\,max} = \sqrt{\frac{\delta}{\delta - 1}} k_s \tag{5.4}$$

with k_s the skin number and $\delta = \frac{w + i\nu}{w_c}$, in which ν is the collision rate and w_c the electron cyclotron frequency.

These two values define the interval in which the propagating waves are damped by the plasma and, consequently, they are important in the study of the radial power deposition, since the antenna current density spectra is defined by the combination of m and k_z modes.

5.2 ANALYSIS

In this section, the plots of the radial power deposition profiles for the Single-Loop, Nagoya III and Helix Fractional antennas are analysed in order to find the correlations with the values of J_ϕ, J_z, m and k_z.

Within the interval limited by $k_{z\,max}$ and $k_{z\,min}$, there will be used only few combinations of these variables as input for the SPIREs code. Through this FDFD electromagnetic solver, it is possible to calculate the electromagnetic fields and the deposited power into the plasma, which is determined thanks to the trapezoidal integration of all the contributions for a particular $m - k_z$ set: the analysis is focused on this intermediate step.

All the data gathered are derived from the following set of parameters:

- magnetic field intensity $B = 70mT$;
- background pressure $p = 15mTorr$;
- electron temperature $T = 7eV$;
- plasma density $n = 1 \cdot 10^{19}$.

5.2.1 *Single-Loop*

In Fig.5.1, it is possible to observe which are the spectra values analysed for a specific $m - k_z$ couple: since for the Single-Loop configuration only the $m = 0$ mode is excited, the other azimuthal modes will be not studied. Moreover, in Chapter 4 it was observed that the spectra function was symmetric along k_z, hence the decision to select only points with positive k_z.

In Fig.5.1a, J_ϕ values for the points chosen have the same intensity; despite this, in Fig.5.2 the five curves are well separated and the major contribute is given by the curve related to the mid-k_z-value point.

Finally, as noticed in all the previous studies, the plasma absorbs power mostly at the outer part of the cylinder, which means that TG waves are the main reason for this deposition mechanism, as described in [8].

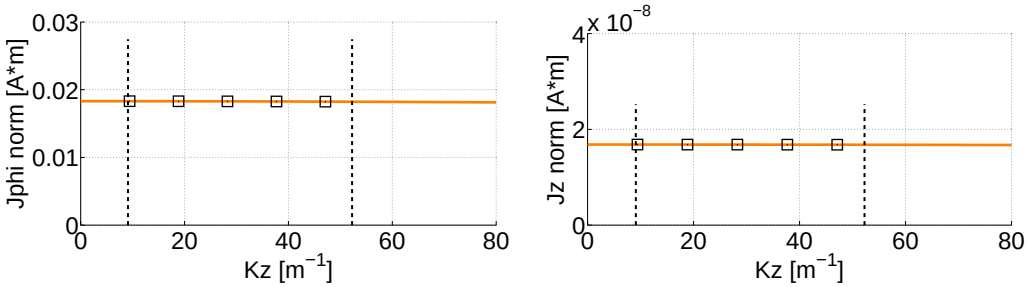

(a) J_ϕ *values chosen for the analysis.* (b) J_z *values chosen for the analysis.*

Figure 5.1: Overview on J_ϕ and J_z spectra curves for a Single-Loop antenna with m=0. The dashed lines delimit the plasma operating interval, whilst the square points are the values chosen for the analysis.

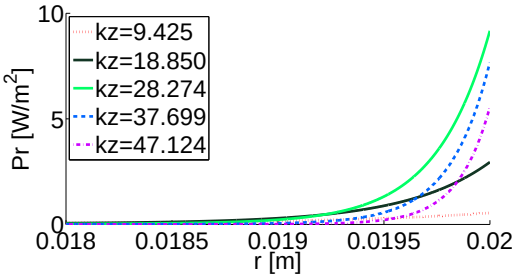

Figure 5.2: Radial deposition power profiles for a Single-Loop antenna with m=0: the spectra input has been varied in order to understand the influence of J_ϕ and J_z on the curve.

5.2.2 *Nagoya*

It must be remembered that J_ϕ and J_z are symmetric along k_z; hence, it is possible to analyse only the spectra for $k_z > 0$. In addition, only the $m = \pm 3$ and $m = \pm 1$ modes will be considered.

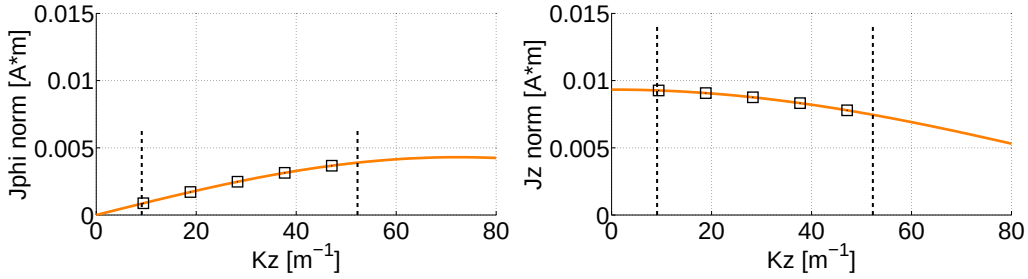

(a) J_ϕ *values chosen for the analysis.* (b) J_z *values chosen for the analysis.*

Figure 5.3: Overview on J_ϕ and J_z spectra curves for a Nagoya III antenna with m=-3. The dashed lines delimit the plasma operating interval, whilst the square points are the values chosen for the analysis.

For $m = \pm 3$, in Fig.5.3 and Fig.5.5, $J_\phi < J_z$ for the points considered ; in addition there is a different trend: J_ϕ grows whilst J_z decreases.

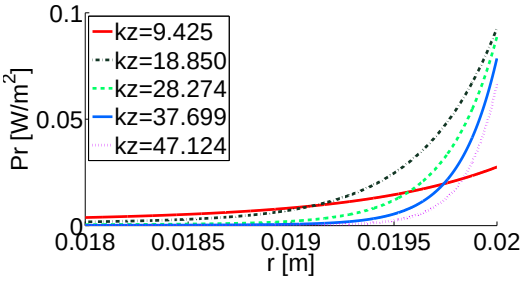

Figure 5.4: Radial deposition power profiles for a Nagoya III antenna with m=-3: the spectra input has been varied in order to understand the influence of J_ϕ and J_z on the curve.

The outputs for $m = \pm 3$ resulted from the SPIREs analysis are the same, as it is shown in Fig.5.4 and Fig.5.6.

All in all, these two figures highlight how the major contributions for $m = \pm 3$ come from the mid-k_z region of the plasma operative interval: although J_z is the highest value selected for $k_z \approx 9.2 m^{-1}$, the radial power profile is flat as compared to the others, probably because J_ϕ, on the contrary, is the lowest.

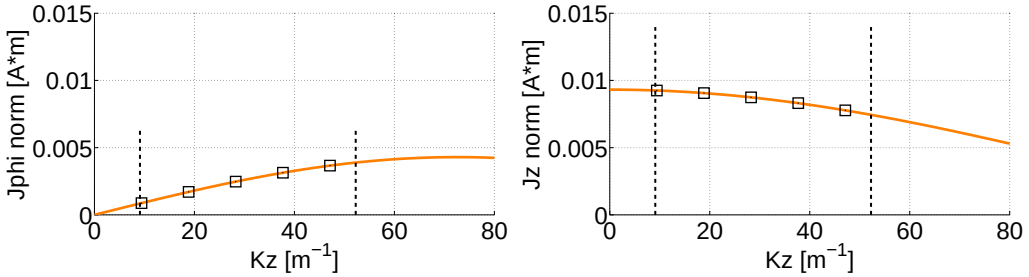

(a) J_ϕ *values chosen for the analysis.* (b) J_z *values chosen for the analysis.*

Figure 5.5: Overview on J_ϕ and J_z spectra curves for a Nagoya III antenna with m=+3. The dashed lines delimit the plasma operating interval, whilst the square points are the values chosen for the analysis.

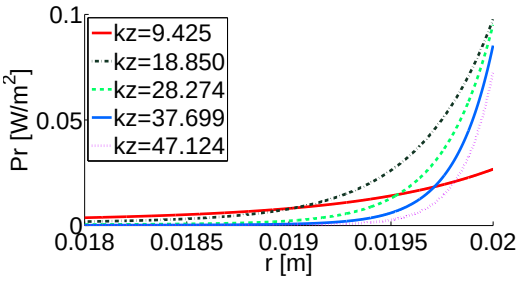

Figure 5.6: Radial deposition power profiles for a Nagoya III antenna with m=+3: the spectra input has been varied in order to understand the influence of J_ϕ and J_z on the curve.

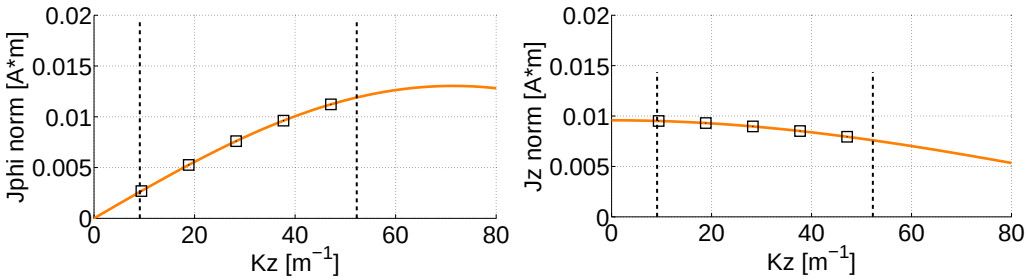

(a) J_ϕ *values chosen for the analysis.* (b) J_z *values chosen for the analysis.*

Figure 5.7: Overview on J_ϕ and J_z spectra curves for a Nagoya III antenna with m=-1. The dashed lines delimit the plasma operating interval, whilst the square points are the values chosen for the analysis.

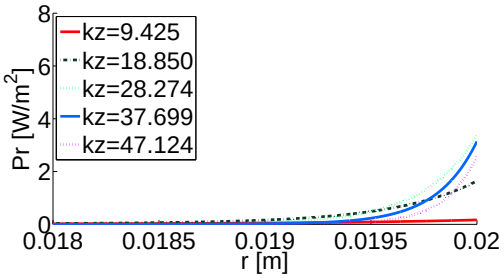

Figure 5.8: Radial deposition power profiles for a Nagoya III antenna with m=-1: the spectra input has been varied in order to understand the influence of J_ϕ and J_z on the curve.

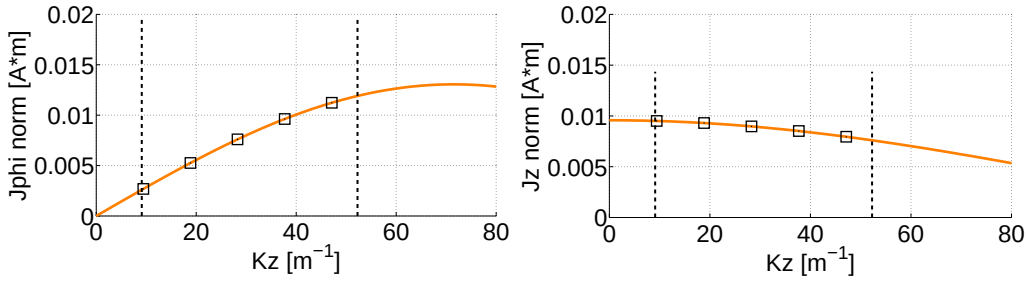

(a) J_ϕ *values chosen for the analysis.* (b) J_z *values chosen for the analysis.*

Figure 5.9: Overview on J_ϕ and J_z spectra curves for a Nagoya III antenna with m=+1. The dashed lines delimit the plasma operating interval, whilst the square points are the values chosen for the analysis.

As concerns $m = \pm 1$, the J_ϕ and J_z values analysed are similar. Looking at Fig.5.8 and Fig.5.10, it is possible to state the following observations:

- the profiles related to $m = +1$ are higher than the ones corresponding to $m = -1$, except for $k_z \approx 19 m^{-1}$;
- for $m = -1$, the curve related to $k_z \approx 19 m^{-1}$ is comparable with the ones related to the other axial wave numbers, whilst it is flat for $m = +1$;
- for $k_z \approx k_{z\,min}$, the profiles for both m modes are completely flat;
- the decay of the radial power profiles happen within the 5% of the plasma cylinder radius.

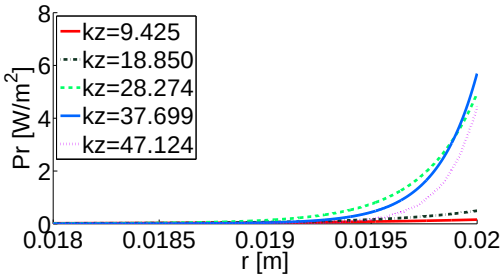

Figure 5.10: Radial deposition power profiles for a Nagoya III antenna with m=+1: the spectra input has been varied in order to understand the influence of J_ϕ and J_z on the curve.

All in all, paying attention to the y-axis of Fig.5.4, Fig.5.6, Fig.5.8 and Fig.5.10, the profiles related to $m = \pm 1$ are higher about 40 times than the $m = \pm 3$ ones, a conclusion similar to the one stated by B. McVey[15].

5.2.3 *Helix Fractional*

For the Helix Fractional antenna, it is necessary to analyse the spectrum for all values of $k_z > 0$, since there is no symmetry as it was for the previous case: 10 values of k_z will define the spectra points for the SPIREs input.

In Fig.5.11 and Fig.5.13, these values are shown for $m = \pm 3$ and it is clear how the curves are specular; moreover, the J_ϕ and J_z quantities are similar, although the latter ones are a bit greater than the former ones.

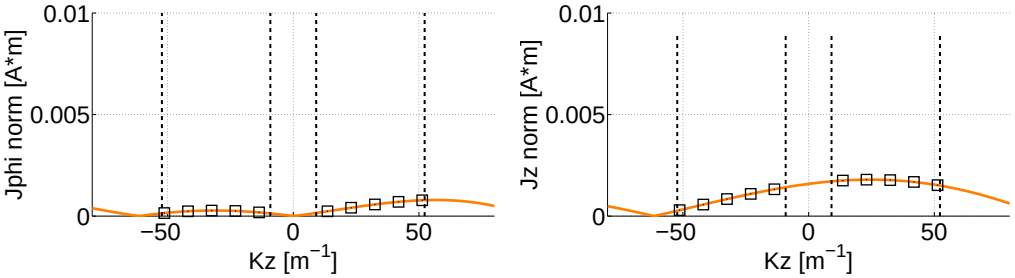

(a) J_ϕ *values chosen for the analysis.* (b) J_z *values chosen for the analysis.*

Figure 5.11: Overview on J_ϕ and J_z spectra curves for a Fractional Helix antenna with m=-3. The dashed lines delimit the plasma operating interval, whilst the square points are the values chosen for the analysis.

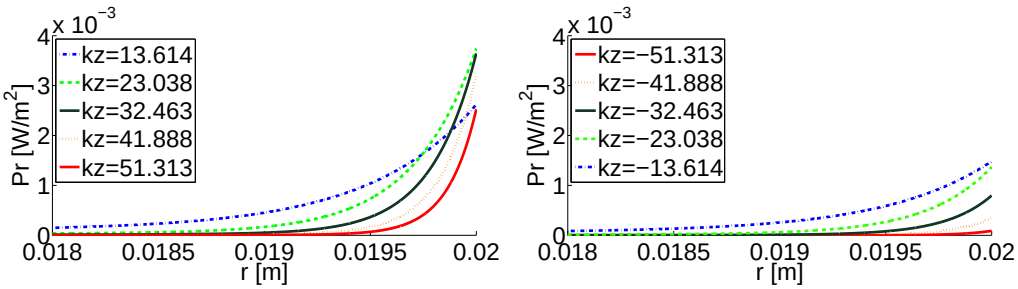

(a) *Complete radial deposition power profile for* $k_z >$ 0. (b) *Complete radial deposition power profile for* $k_z <$ 0.

Figure 5.12: Radial deposition power profiles for a Fractional Helix antenna with m=-3: the spectra input has been varied in order to understand the influence of J_ϕ and J_z on the curve, with separated plots according to k_z sign.

Looking at Fig.5.12 and Fig.5.14, it is possible to underline these characteristics:

- Fig.5.12a, Fig.5.12b, Fig.5.14a and Fig.5.14b are specular according to the sign of m and k_z;
- the most performing profiles are obtained with $k_z \approx k_{z\,min}$;
- for $m = -3 (m = +3)$ and $k_z > 0 (k_z < 0)$, all the profiles subtend a comparable area whilst, for $k_z < 0 (k_z > 0)$, there is a decay as k_z decreases(increases);
- contributions for $m = -3 (m = +3)$ and $k_z > 0 (k_z < 0)$ are higher(about 2 times) than the ones related to $k_z < 0 (k_z > 0)$;
- all the radial profiles decay within the 5% of the plasma cylinder radius, except at $k_z \approx k_{z\,min}$ for which the decay happens within the 10%.

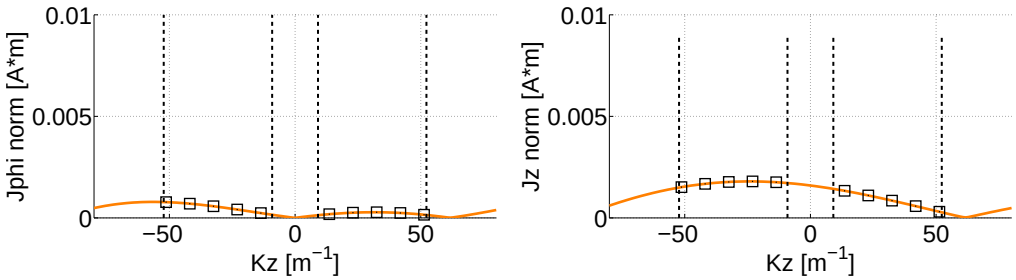

(a) J_ϕ *values chosen for the analysis.* (b) J_z *values chosen for the analysis.*

Figure 5.13: Overview on J_ϕ and J_z spectra curves for a Fractional Helix antenna with m=+3. The dashed lines delimit the plasma operating interval, whilst the square points are the values chosen for the analysis.

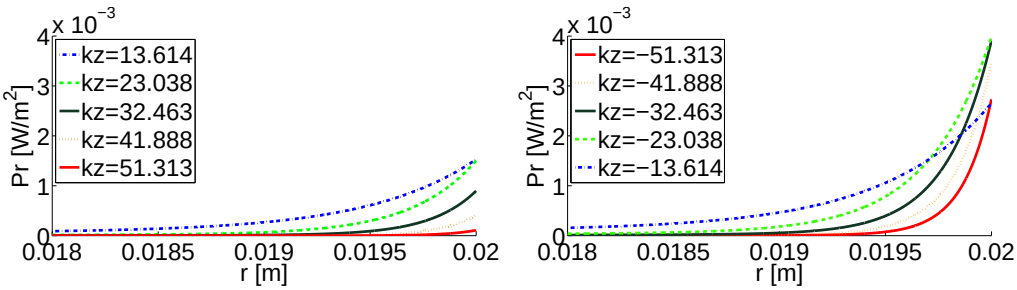

(a) *Complete radial power profile for* $k_z > 0$. (b) *Complete radial power profile for* $k_z < 0$.

Figure 5.14: Radial deposition power profiles for a Fractional Helix antenna with m=+3: the spectra input has been varied in order to understand the influence of J_ϕ and J_z on the curve, with separated plots according to k_z sign.

In Fig.5.15 and Fig.5.17, the J_ϕ and J_z spectral values are shown for $m = \pm 1$: the figures are specular to each other and the values analysed are also similar.

Looking at Fig.5.16 and Fig.5.18, the considerations are as follows:

- Fig.5.16a and Fig.5.18b present profiles of the same order but not specular as for the $m = \pm 3$; the same comment can be extended to Fig.5.16b and Fig.5.18a;

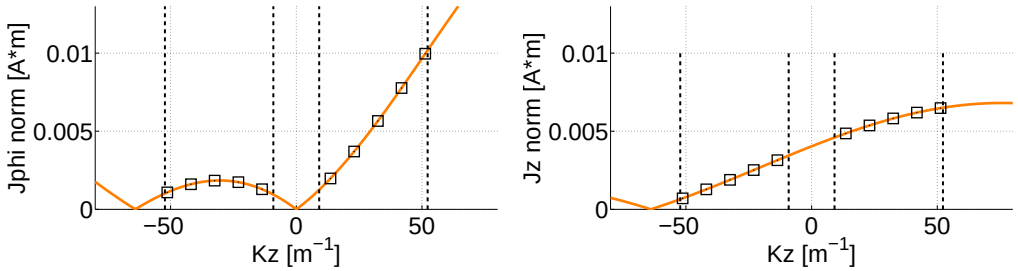

(a) J_ϕ *values chosen for the analysis.* (b) J_z *values chosen for the analysis.*

Figure 5.15: Overview on J_ϕ and J_z spectra curves for a Fractional Helix antenna with m=-1. The dashed lines delimit the plasma operating interval, whilst the square points are the values chosen for the analysis.

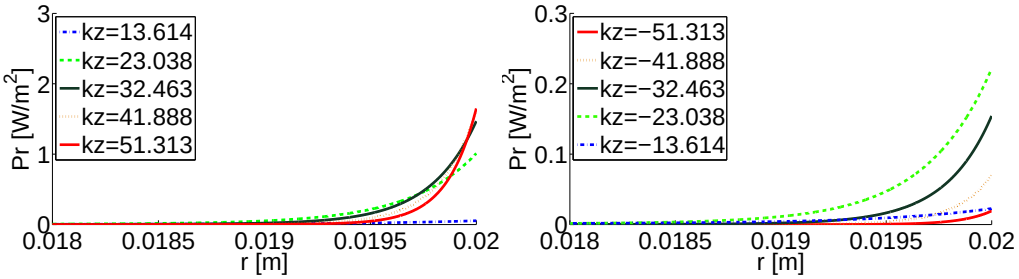

(a) *Complete radial power profile for* $k_z > 0$. (b) *Complete radial power profile for* $k_z < 0$.

Figure 5.16: Radial deposition power profiles for a Fractional Helix antenna with m=-1: the spectra input has been varied in order to understand the influence of J_ϕ and J_z on the curve, with separated plots according to k_z sign.

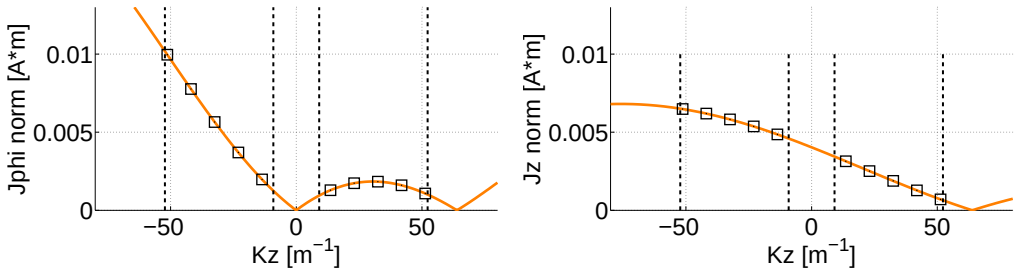

(a) J_ϕ *values chosen for the analysis.* (b) J_z *values chosen for the analysis.*

Figure 5.17: Overview on J_ϕ and J_z spectra curves for a Fractional Helix antenna with m=+1. The dashed lines delimit the plasma operating interval, whilst the square points are the values chosen for the analysis.

- the waves for $k_z < 0 (k_z > 0)$ and $m = +1 (m = -1)$ are absorbed better at the edge of the plasma cylinder than the ones for $k_z > 0 (k_z < 0)$ and $m = +1 (m = -1)$;
- the waves for $k_z < 0 (k_z > 0)$ and $m = +1 (m = -1)$ are absorbed better at the edge of the plasma cylinder than the ones for $k_z > 0 (k_z < 0)$ and $m = -1 (m = +1)$;

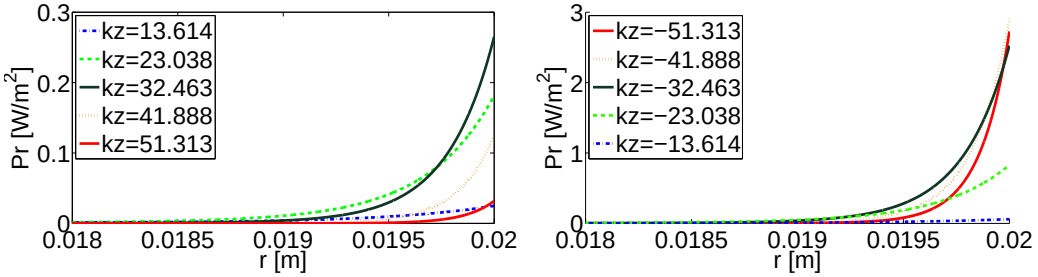

(a) *Complete radial power profile for* $k_z > 0$. (b) *Complete radial power profile for* $k_z < 0$.

Figure 5.18: Radial deposition power profiles for a Fractional Helix antenna with m=+1: the spectra input has been varied in order to understand the influence of J_ϕ and J_z on the curve, with separated plots according to k_z sign.

- only with k_z belonging to the mid region of the operative interval there significant contributions from the radial power profiles.

Finally, there is a huge difference between the $m = \pm 1$ and $m = \pm 3$ profiles: only comparing Fig.5.18b and Fig.5.14b, a factor of 1000 can be determined in favour of the former waves.

5.3 FINAL COMMENTS

Many observations can be made on this analysis; here the principal ones:

- thanks to the Single-Loop antenna radial power profiles, it is confirmed that the contributions for $m = 0$ are greater(about 3 times) than those relative to the other azimuthal modes although the spectra values are of the same order of magnitude;
- through the Nagoya III and the Helix Fractional antenna profiles, it is confirmed that the contributions related to $m = \pm 3$ are negligible respect to the ones related to $m = \pm 1$. For the former case, the order of magnitude is 40 times lower whilst for the latter one the difference is about 1000 times;
- the Nagoya III performs better than the Helix Fractional, which can be explained because of an higher and more constant spectral values in the operative interval;
- the best performances were obtained thanks to k_z belonging to the mid interval delimited by $k_{z\,min}$ and $k_{z\,max}$. For $k_z \approx k_{z\,min}$, the derived profiles are flat for all the cases studied;
- specular spectra functions cause the same characteristic also into the radial power profiles only for $m = \pm 3$. For $m = \pm 1$, there is a similar behaviour but the differences can be detected visibly;
- the combined profiles for all the antenna configurations decay rapidly within the $3 - 5\%$ of the plasma cylinder radius. From that distance to

the centre of the cylinder, are almost null. Following the considerations expressed by Chen[12], this is caused by the damping of the TG waves.

From these general considerations, an ideal antenna current density spectra function should have the highest values for k_z far from $k_{z\,min}$ and should excite the $m = 0$ and $m = \pm 1$ modes simultaneously: in the next chapter, an attempt will be done with new antenna configurations.

6 NEW CONFIGURATIONS

In this final part, two new antenna configurations will be analysed in order to test the observations made in the previous chapter.

In the first section there will be the description of the analytical relation of the antenna current density spectrum for such devices.

Then, the results from the ADAMANT code in combination with the new algorithm will be explained for a specific combination of parameters: not only the spectrum but also the power absorbed by the plasma is available.

Finally, through SPIREs, it is possible to obtain the radial power profiles in the plasma cylinder for these two configurations, using the the spectra functions determined meanwhile.

6.1 ANALYTICAL SPECTRA RELATION

The two new antennas are always considered as a 3D geometry and the process used for the determination of the closed form relation is the same as the one used in Chapter 3.

6.1.1 *Half-Double Loop*

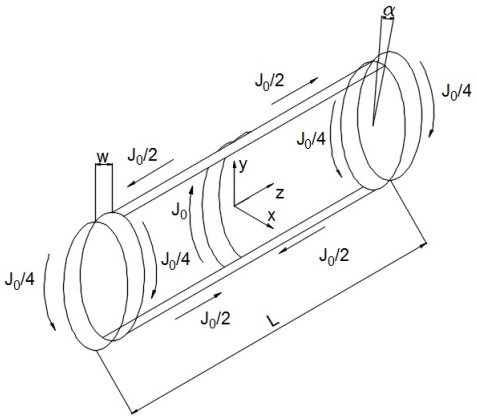

Figure 6.1: Scheme of the first configuration: two loops are connected to a half central loop through axial links.

Since the aim was to maximize the J_ϕ spectrum in an interval around $k_z = 0$, the Helix Fractional antenna was taken as an example: its helical links are the responsible for the shift of J_ϕ spectrum, leaving low values near k_z.

The idea was to leave the same current distribution around the two lateral loops as the ones for the Helix Fractional, but avoiding the shift: with the configuration illustrated in Fig.6.1, this is possible.

The current density functions, $\vec{J}_\phi(r,\phi,z)$ and $\vec{J}_z(r,\phi,z)$ have the following form:

$$\begin{aligned}\vec{J}_\phi =& \frac{J_0}{4}\delta(r-a)\left[u_\theta(-\frac{\pi}{2};\frac{\pi}{2})-u_\theta(\frac{\pi}{2};\frac{3}{2}\pi)\right]\\ &\left[u_z(\frac{L-w}{2};\frac{L+w}{2})+u_z(\frac{-L-w}{2};\frac{-L+w}{2})\right]+\\ &+J_0\delta(r-a)u_\theta(\frac{\pi}{2};\frac{3}{2}\pi)u_z(-\frac{w}{2};\frac{w}{2})\end{aligned} \tag{6.1}$$

$$\begin{aligned}\vec{J}_z =& \frac{J_0}{2}\delta(r-a)\left[u_z(\frac{w}{2};\frac{L-w}{2})-u_z(\frac{-L+w}{2};-\frac{w}{2})\right]\\ &\left[u_\theta(\frac{\pi}{2}-\alpha;\frac{\pi}{2}+\alpha)-u_\theta(\frac{3}{2}\pi-\alpha;\frac{3}{2}\pi+\alpha)\right]\end{aligned} \tag{6.2}$$

where a is the antenna radius and α is the angle subtended by half of the axial links.

The corresponding spectra equations, $\tilde{J}_\phi(m,k_z)$ and $\tilde{J}_z(m,k_z)$ can be easily expressed with the next relations:

$$\tilde{J}_\phi = \frac{4J_0 a}{k_z m}\cos\frac{k_z L}{2}+2\frac{J_0 a}{m}\,w\,\mathrm{sinc}(\frac{k_z w}{2})+\delta(m)J_0\pi\,a\,w\,\mathrm{sinc}(\frac{k_z w}{2}) \tag{6.3}$$

$$\tilde{J}_z = \frac{J_0}{2}\frac{4}{k_z}\sin\frac{k_z L}{4}\sin\frac{L-2w}{4}\;\;\frac{4\sin(m\alpha)}{m} \tag{6.4}$$

where $\tilde{J}_z$ is valid only for odd values of m.

From Eq.(6.3), it is possible to note that also the azimuthal mode $m=0$ contributes to the $\tilde{J}\phi$ component thanks to the half loop located at the middle of the antenna.

6.1.2 *Out-of-Phase Double Loop*

Another attempt can be done improving the contribution from $m=0$. In order to do so, the scheme in Fig.6.2 is proposed: the loops are excited out-of phase with respect to each other; precisely, the test consists on trying different phase values in order to find the most suitable configuration.

Since there are no axial contributions, only the antenna current density function $\vec{J}_\phi(r,\phi,z)$ is considered:

$$\vec{J}_\phi = J_0\delta(r-a)u_\theta(0;2\pi)\left[u_z(e^{i\beta}\frac{L-w}{2};\frac{L+w}{2})+u_z(\frac{-L-w}{2};\frac{-L+w}{2})\right] \tag{6.5}$$

with β as the desired phase.

The spectra function $\tilde{J}_\phi(m,k_z)$ will be:

$$\tilde{J}_\phi = 2J_0\delta(m)\pi\,a\,\left[2w\cos\frac{k_z L}{2}\,\mathrm{sinc}(\frac{k_z w}{2})+(e^{i\beta}-1)\frac{\sin(k_z\frac{L+w}{2})}{-i\,k_z}\right] \tag{6.6}$$

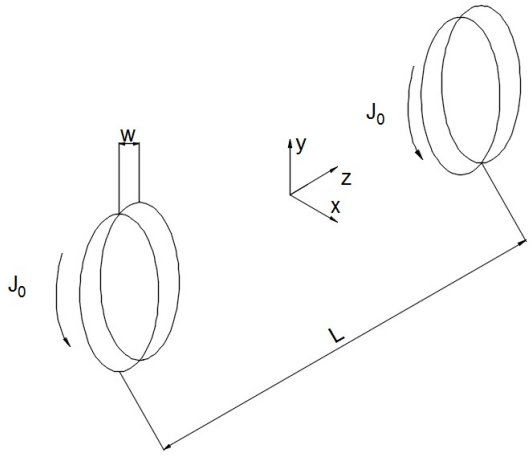

Figure 6.2: Scheme of the second configuration: two loops separated loops excited with two different ports.

6.2 POWER AND SPECTRAL ANALYSIS

For both the configurations, there is a first part in which the deposition power is compared to the antennas analysed previously: this was possible through ADAMANT. It must be remembered that the absorbed power is found through the following relation [18]

$$P = \frac{\omega}{2\epsilon_0} \mathrm{Im} \int_{V_p} \vec{D}_P^* \cdot \overleftrightarrow{\epsilon}_r^{-1} \cdot \vec{D}_P \tag{6.7}$$

where ω is the exciting frequency, $\overleftrightarrow{\epsilon}$ is the plasma permittivity dyadic relative to free space, V_p is the plasma volume and $\vec{D}_P$ is the the total electric flux density within the medium that fills V_p.

In the second part the spectral representation of the current density distribution will be observed in order to check if they correspond to the formulas determined before.

6.2.1 *Half-Double Loop*

Thanks to ADAMANT, it was possible to solve the electromagnetic problem for the antenna with the following combination of discharge parameters:

- magnetic field intensity B from 10 to 100mT;
- plasma density n from $1 \cdot 10^{17}$ to $5 \cdot 10^{19}$.

Comparing the power deposition into the plasma and with the support of Fig.6.3, it is possible to see how the Nagoya III antenna is the most efficient one for all the magnetic field range analysed; despite this, the new antenna seems to have good properties since it is always better than the Helix Fractional and the Single-Loop antenna; moreover, as the plasma density rises, the power absorbed by the plasma is greater than the one absorbed thanks to the Nagoya III type.

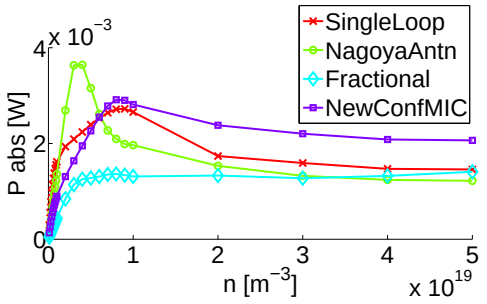

(a) *Deposition power for B=20mT.*

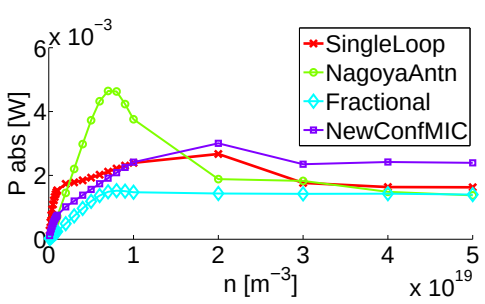

(b) *Deposition power for B=40mT*

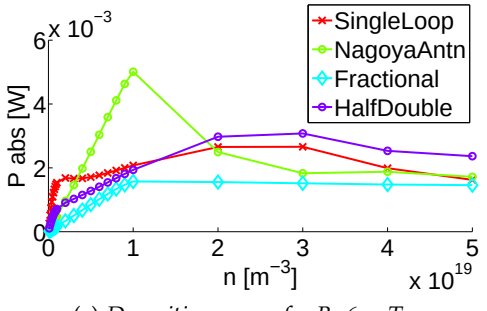

(c) *Deposition power for B=60mT.*

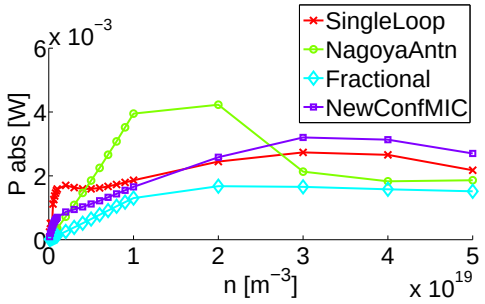

(d) *Deposition power for B=80mT*

Figure 6.3: Power deposition plot of a Half Double Loop for p=15mTorr and T=7eV.

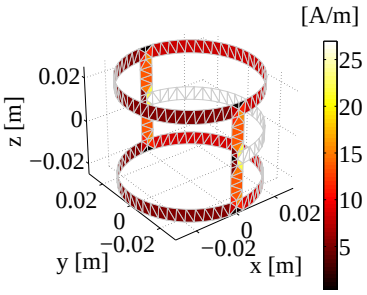

(a) *Antenna current density distribution on the antenna surface.*

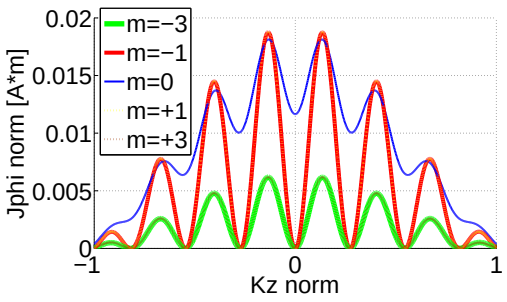

(b) *2D J_ϕ representation.*

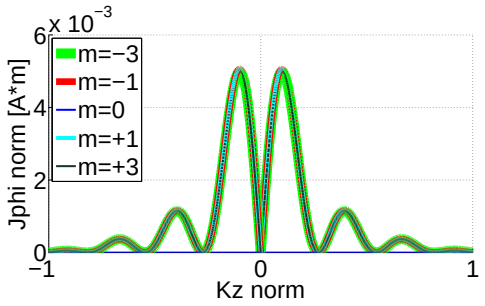

(c) *2D J_z representation.*

Figure 6.4: 2D representations of the spectra components and mesh plot of a Half Double Loop for p=15mTorr and T=7eV. $k_{z\,norm}$ corresponds to the axial wave number k_z divided by $\frac{L}{2\pi}$.

At this point, also the antenna current density is available among the ADAMANT outputs; therefore, after having run the program, it is possible to observe the spectral response of the antenna.

In Fig.6.4a, the antenna current density distribution is illustrated: the half loop is swept by all the current density; in addition, it seems that along the edge-loops, the density current is almost divided equally.

In Fig.6.4b, J_ϕ presents also an excitation mode for $m = 0$ as expected by Eq.(6.3). In addition, the spectra is symmetric along both m and k_z and the trend of the curves are those expected always by Eq.(6.3).

Proceeding with J_z, in Fig.6.4c there are no contribution for $m = 0$ and the curves for $m = \pm 1$ and $m = \pm 3$ are coincident: everything goes according to Eq.6.4. Another aspect to underline is that J_ϕ is greater about 3 times respect to J_z for $m = \pm 1$, whilst they are of the same order for $m = \pm 3$.

6.2.2 *Out-of-Phase Double Loop*

The study on this antenna was made for the same parameters as done for the previous case. The difference consists of the variation of the phase: the delay at which the second loop is excited can be an important factor of influence on the power deposition.

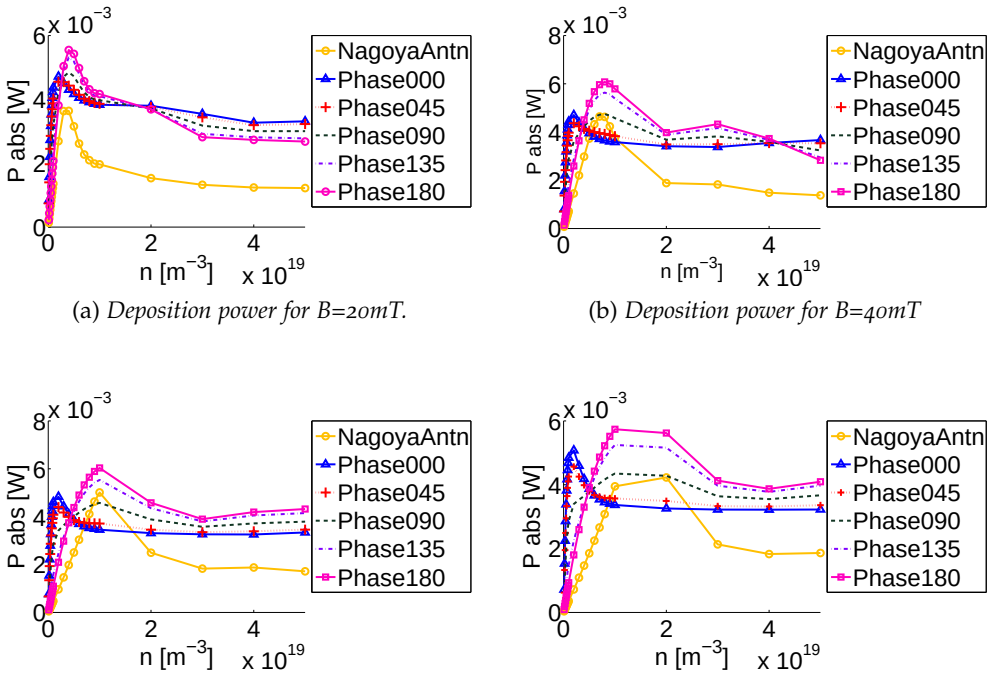

(a) *Deposition power for B=20mT.*

(b) *Deposition power for B=40mT*

(c) *Deposition power for B=60mT.*

(d) *Deposition power for B=80mT*

Figure 6.5: Power deposition plot of an Out-of-Phase antenna for p=15mTorr and T=7eV.

It is evident from Fig.6.5 how a great improvement has been made with respect to the other antennas: almost all the phases tested give better results than

the Nagoya III case, although 135° and 180° phase shifts are the best options in the wide magnetic field range analysed.

In addition, the peak values for the curves related to $\beta = 0°$ and $\beta = 45°$ are obtained for $n \approx 10^{17} m^{-3}$ whilst for the other phase values the peaks occur around $n = 10^{18} m^{-3}$.

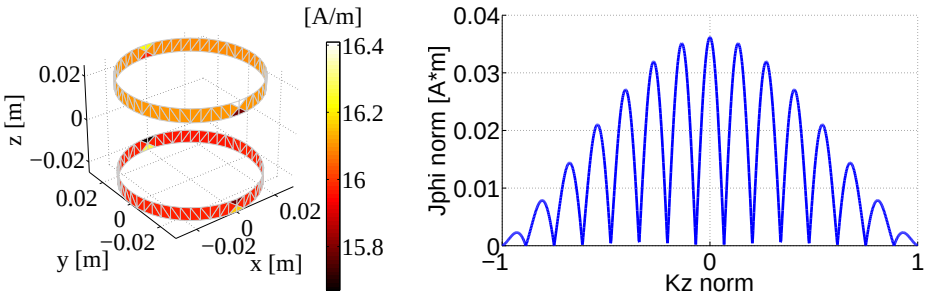

(a) *Antenna current density distribution on the antenna surface.*

(b) *2D J_ϕ representation.*

Figure 6.6: 2D representations of the spectra components and mesh plot of an Out-of-Phase Double Loop antenna for p=15mTorr and T=7eV: $\beta = 0°$. $k_{z\,norm}$ corresponds to the axial wave number k_z divided by $\frac{L}{2\pi}$.

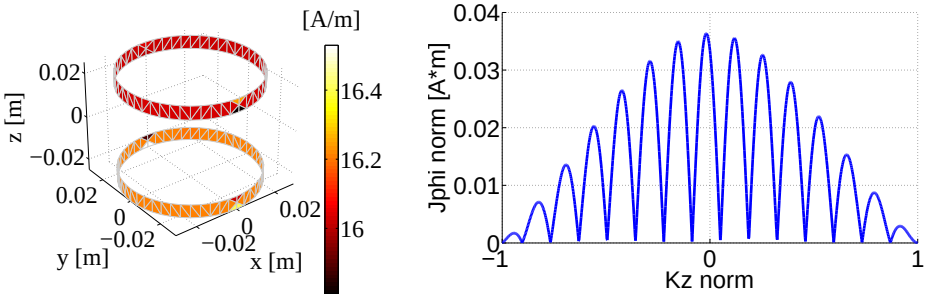

(a) *Antenna current density distribution on the antenna surface.*

(b) *2D J_ϕ representation.*

Figure 6.7: 2D representations of the spectra components and mesh plot of an Out-of-Phase Double Loop antenna for p=15mTorr and T=7eV: $\beta = 45°$. $k_{z\,norm}$ corresponds to the axial wave number k_z divided by $\frac{L}{2\pi}$.

The next step is to analyse the output from ADAMANT: Fig.6.6a, Fig.6.10a show a similar current density distribution since on the upper loop there is the highest current density; the opposite observation is valid for Fig.6.7a, Fig.6.8a and Fig.6.9a.

All in all, the spectra response is shown only for $m = 0$ since we are considering two separated loops. The form and the intensity of the curves in Fig.6.6b, Fig.6.7b, Fig.6.8b, Fig.6.9b and Fig.6.10b are the same: an interesting feature is that the curves shift to the left as β increases until 180°, where $J_\phi = 0$ for $k_z = 0$ whilst, for $\beta = 0°$, k_z is a point of maximum.

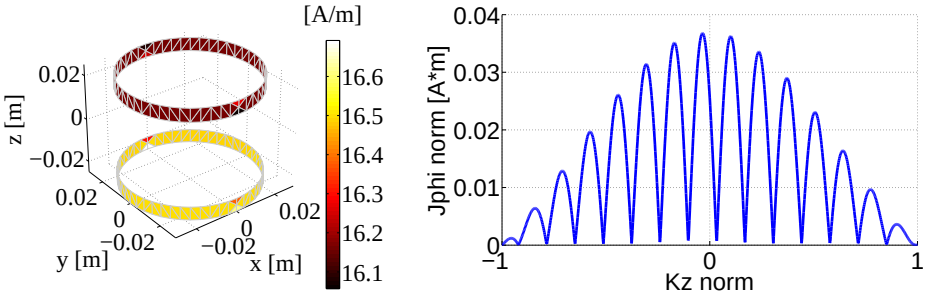

(a) *Antenna current density distribution on the antenna surface.*

(b) *2D* J_ϕ *representation.*

Figure 6.8: 2D representations of the spectra components and mesh plot of an Out-of-Phase Double Loop antenna for p=15mTorr and T=7eV: $\beta = 90°$. $k_{z\,norm}$ corresponds to the axial wave number k_z divided by $\frac{L}{2\pi}$.

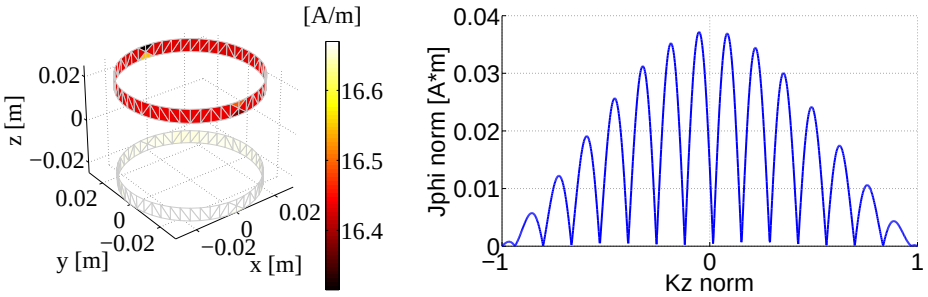

(a) *Antenna current density distribution on the antenna surface.*

(b) *2D* J_ϕ *representation.*

Figure 6.9: 2D representations of the spectra components and mesh plot of an Out-of-Phase Double Loop antenna for p=15mTorr and T=7eV: $\beta = 135°$. $k_{z\,norm}$ corresponds to the axial wave number k_z divided by $\frac{L}{2\pi}$.

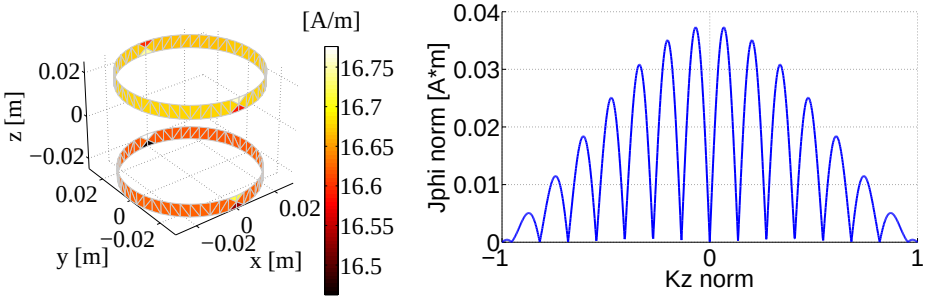

(a) *Antenna current density distribution on the antenna surface.*

(b) *2D* J_ϕ *representation.*

Figure 6.10: 2D representations of the spectra components and mesh plot of an Out-of-Phase Double Loop antenna for p=15mTorr and T=7eV: $\beta = 180°$. $k_{z\,norm}$ corresponds to the axial wave number k_z divided by $\frac{L}{2\pi}$.

6.3 RADIAL DEPOSITION POWER PROFILE

After having analysed the results obtained with ADAMANT and the new algorithm, it is possible to use SPIREs to elaborate the spectra in order to ob-

serve how the radial power deposition is influenced: the aim is to understand whether it was possible to define the ideal antenna current density spectral function with these new configurations.

Another goal is to validate the considerations made about the positive influence which have particular k_z values always on the radial power profile.

6.3.1 *Half-Double Loop*

Since in Chapter 5, we confirmed that the contributions related to $m = \pm 3$ were negligible respect to $m = \pm 1$, only the last ones and $m = 0$ will be analysed.

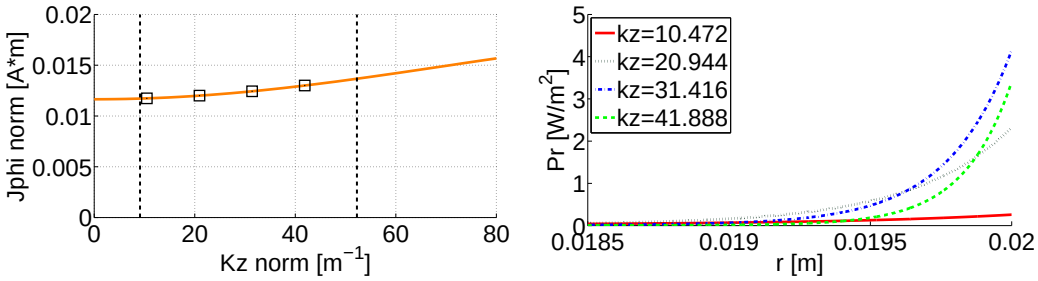

(a) J_ϕ *values chosen for the analysis.* (b) *Radial deposition power profile.*

Figure 6.11: Overview on J_ϕ spectra curve and radial power deposition profile for a Half-Double Loop antenna with m=0. The dashed lines delimit the plasma operating interval, whilst the square points are the values chosen for the analysis.

For $m = 0$, it was pointless to analyse the contribution derived from J_z since $J_\phi \gg J_z$. In Fig.6.11a, it is possible to note how all the values are similar among each other, although there is a slight increase: this trend can be seen also in Fig.6.11b, where the curves are well separated emphasizing this correlation. The only exception is the curve related to $k_z \approx 31 m^{-1}$: this curve subtends the highest area among those considered, supporting the theory that for mid k_z values the plasma absorbs more power.

In Fig.6.12, the values of the spectra components for a particular $m - k_z$ pair are shown: they are the same for $m = \pm 1$, as it was expected since the symmetry along m. In this particular case, J_ϕ and J_z increase as k_z raises; in addition, it is visible how $J_\phi \gg J_z$ as already written before.

Despite the symmetry, Fig.6.13 shows how the contributions are different according to the sign of m: for $m = +1$, the curves related to the two greatest k_z demonstrate an absorption near the edge of the plasma cylinder about 2 times greater than the profiles related to $m = -1$. As for the lines for the remaining k_z, there are no particular differences: for $k_z \approx k_{z\,max}$, the wave is not damped leaving a flat radial profile.

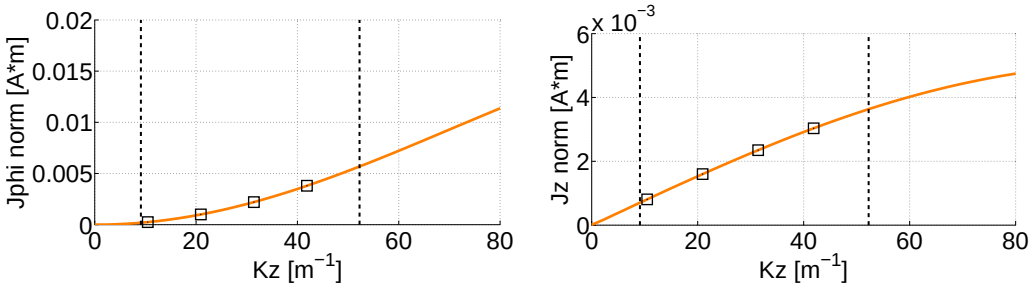

(a) J_ϕ *values chosen for the analysis.* (b) J_z *values chosen for the analysis.*

Figure 6.12: Overview on J_ϕ and J_z spectra curves for a Half-Double Loop antenna with $m = \pm 1$. The dashed lines delimit the plasma operating interval, whilst the square points are the values chosen for the analysis.

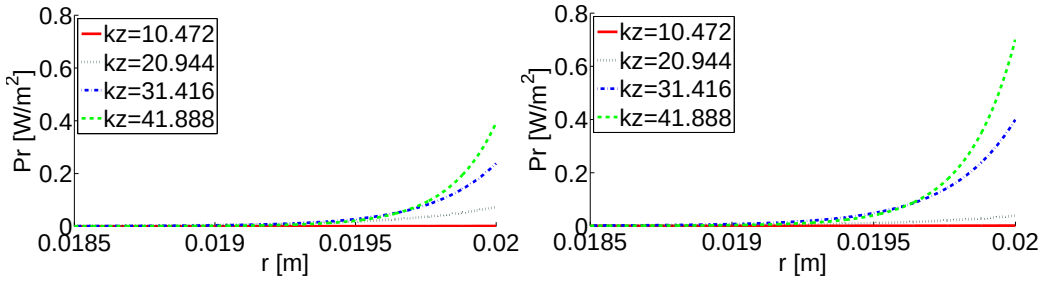

(a) *Complete radial deposition profile for* $m = -1$. (b) *Complete radial deposition profile for* $m = +1$

Figure 6.13: Radial power deposition profiles for a Half-Double Loop antenna with $m = \pm 1$.

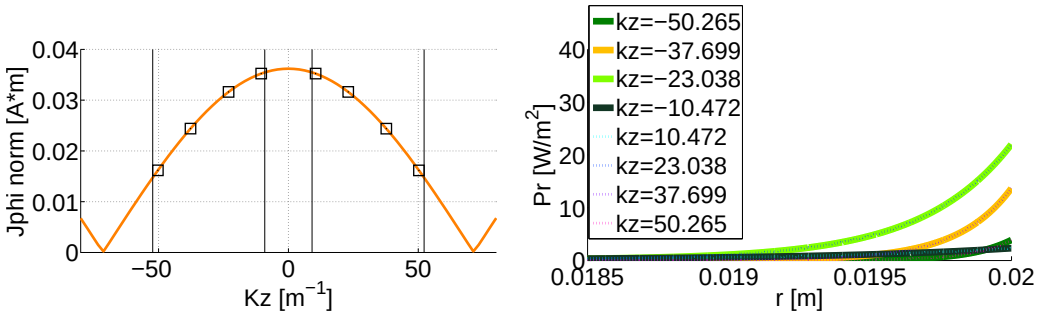

(a) J_ϕ *values chosen for the analysis.* (b) *Radial deposition power profile.*

Figure 6.14: Overview on J_ϕ spectra curve and radial power deposition profile for a Half-Double Loop antenna with m=0 and $\beta = 0°$. The dashed lines delimit the plasma operating interval, whilst the square points are the values chosen for the analysis.

6.3.2 *Out-of-Phase Double Loop*

The first observation concerns the symmetry: in Fig.6.14 and Fig.6.18, that is for $\beta = 0°$ and $\beta = 180°$, there is no difference between the profiles derived from

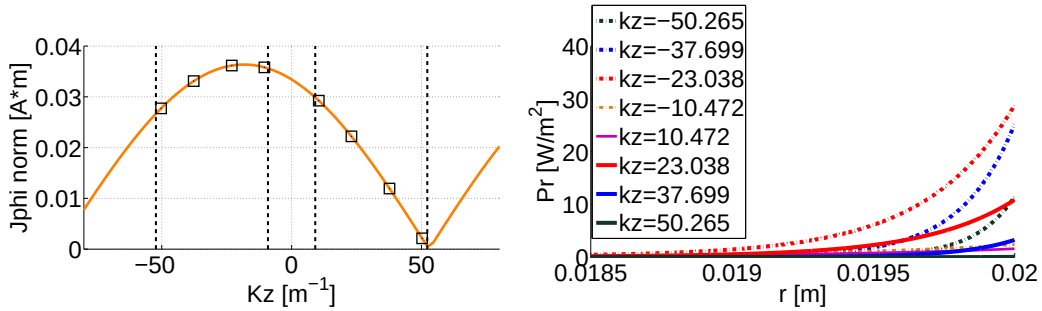

(a) J_Φ *values chosen for the analysis.* (b) *Radial deposition power profile.*

Figure 6.15: Overview on J_Φ spectra curve and radial power deposition profile for a Half-Double Loop antenna with m=0 and $\beta = 45°$. The dashed lines delimit the plasma operating interval, whilst the square points are the values chosen for the analysis.

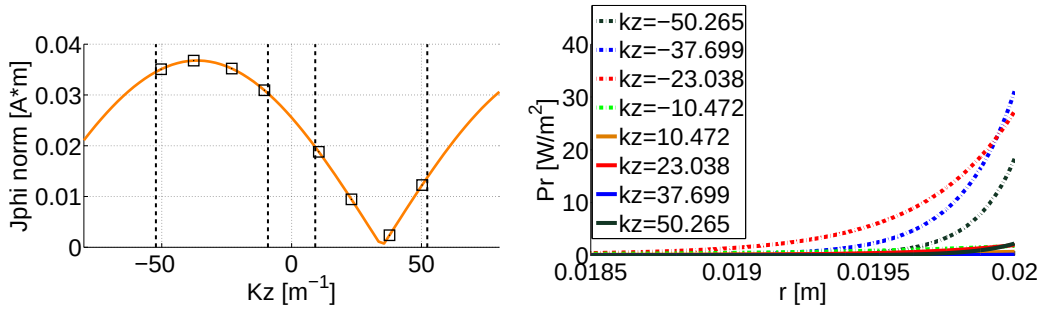

(a) J_Φ *values chosen for the analysis.* (b) *Radial deposition power profile.*

Figure 6.16: Overview on J_Φ spectra curve and radial power deposition profile for a Half-Double Loop antenna with m=0 and $\beta = 90°$. The dashed lines delimit the plasma operating interval, whilst the square points are the values chosen for the analysis.

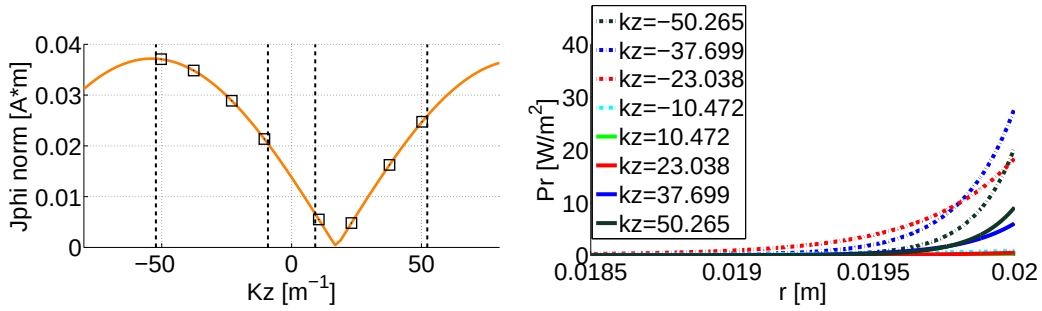

(a) J_Φ *values chosen for the analysis.* (b) *Radial deposition power profile.*

Figure 6.17: Overview on J_Φ spectra curve and radial power deposition profile for a Half-Double Loop antenna with m=0 and $\beta = 135°$. The dashed lines delimit the plasma operating interval, whilst the square points are the values chosen for the analysis.

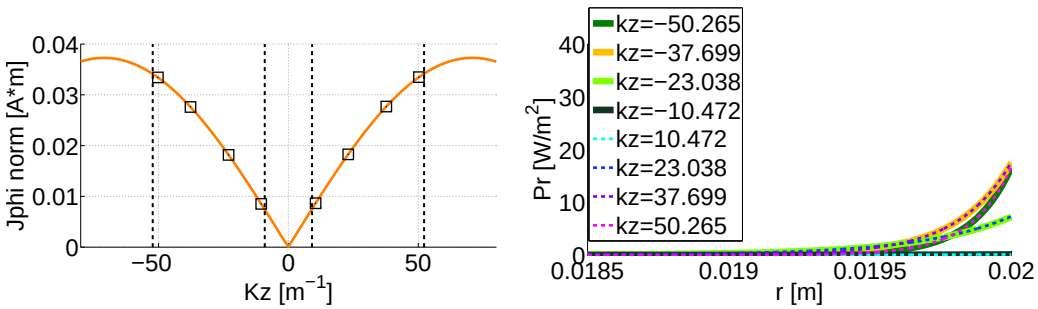

(a) J_ϕ *values chosen for the analysis.* (b) *Radial deposition power profile.*

Figure 6.18: Overview on J_ϕ spectra curve and radial power deposition profile for a Half-Double Loop antenna with m=0 and $\beta = 180°$. The dashed lines delimit the plasma operating interval, whilst the square points are the values chosen for the analysis.

k_z of opposite sign, in contrast with what it was observed for the other antennas: the only explanation is that we are considering an even azimuthal number and that the phase of the spectral complex values considered are similar.

A general observation is that, for k_z near $k_{z\,min}$, the radial profile is really flat as if the corresponding wave is not damped, typical behaviour of an H wave.

On the other hand, for k_z near $k_{z\,max}$, the radial profile rises as the spectra value interested increases: it is a regular trend since the curve is always below to the other ones although these are derived with minor J_ϕ. Another conclusion is that the mid-k_z region is an amplification area for the reasons just described.

In closing, the power deposited into the plasma for this set of discharge parameters is the highest for $\beta = 180°$: according to the previous figures, the best configuration should have been for $\beta = 90°$ since they reach the maximum peak compared to the other cases. It must be said, though, that only three curves on eight contribute to the radial deposition power and this is not enough to overcome the performances obtained through constant profiles observable in Fig.6.18b for $\beta = 180°$.

6.4 CONCLUSIONS

The two configurations investigated helped to understand the absorption mechanism of the power by the plasma. Moreover, they resulted in really efficient devices, comparable, if not better, than the Nagoya III antenna type.

Thanks to ADAMANT the power absorbed by the plasma was available for both the configurations. For the Half-Double Loop antenna, the power is the highest for the high values of the plasma density, but it never reaches the peaks observable for the Nagoya III.

On the other hand, with the Out-of-Phase Double Loop, it is possible to adapt the phase according to the plasma density range considered: for low values, the configurations for $\beta = 0°$ or $\beta = 45°$ show the highest absorbed power, whilst, for high n values, the remaining configurations present the same characteristics.

As for SPIREs outputs, an important confirmation is made about the influence the spectrum intensity in the interval delimited by $k_{z\,max}$ and $k_{z\,min}$: for $m = 0$, the Out-of-Phase Double Antenna spectrum was higher than the one relative to the Half-Double antenna and the consequence was a more performing set of radial profiles of power deposition into the plasma.

Furthermore, the contributions from the $m = \pm 1$, regarding the Half-Double antenna, were not enough to match the radial profiles obtained with only the $m = 0$ mode of the Out-of-Phase antenna.

About the ideal antenna current density spectrum, Fig.6.14b and Fig.6.18b could help a lot in its definition: the cases with $\beta = 0°$ and $\beta = 180°$ present the most constant and highest spectral values; however, the configuration which causes the best performing profiles is the second one.

The explanation is always that far from $k_z = k_{z\,min}$, the radial profiles derived are not flat: in the $\beta = 180°$ case, the spectral function has a decreasing(growing) trend for $k_z < 0 (k_z > 0)$, leaving no other interpretation on the results.

In closing, another option that can improve the antenna performances could be inside the equations which define $k_{z\,min}$ and $k_{z\,max}$: the plasma density n and the magnetic field intensity B are variables which might optimize the operative interval for a particular antenna current density spectrum in order to maximize the deposition power into the plasma.

7

CONCLUSIONS

The HPS is the frame in which the plasma is produced. Its components consist of a gas feeding system, a RF antenna, a plasma cylinder and a magnetic coil. In this thesis, the interaction of the antenna with the plasma has been analysed with a new approach: the results have been then compared with the ones obtained through the studies on HPS conducted so far.

The old approach on the electromagnetic problem is based on considering the antenna as a thin-wire device; in addition, the electric current is assumed rather than computed and it is considered as uniform. In this way, it is possible to study only the response of the plasma. The problem is simplified by the application of the TF to the Maxwell's equations: these are reduced to a coupled set of ordinary equation which have a unique solution if boundary conditions are provided: ANTENA[15], HELIC[11][12] and SPIREs[13] codes, although are different solvers, work with these assumptions.

On the contrary, the new approach do not assume the antenna electric current as a known variable but it studied the mutual interaction between the RF device and the plasma. Another difference is the antenna geometry considered: the thin-wire approximation is discarded and a 3D configuration with a finite surface along the z-axis is considered. With the ADAMANT[18] tool, it is possible to implement these hypothesis and to solve the electromagnetic problem through a system of surface and volume integral equations: specifically, the unknown variables are the antenna current density distribution and the volume polarization current within the plasma.

In order to ascertain the soundness of this new approach, it is necessary to compare similar physical quantities from both the studies. The problem is transferred, therefore, to the spectral domain, precisely to the comparison between the spectral functions of the antenna current density.

As concerns the old approach, this function is already available since the TF already transfer the problem to the spectral domain. On the other hand, only the current density distribution on a 3D surface antenna is available among ADAMANT outputs: this is why an algorithm was developed in order to apply the TF to this function, which is defined with the RWG functions.

Several tests have been conducted on simple antenna geometries on which a uniform current was imposed, allowing the opportunity to compare the outputs with an analytical expression: all the analysis validated the algorithm.

From a previous work[24], the results for the Single-Loop, Nagoya III and Fractional Helix antennas showed that the current density function, distributed on a surface and not on a thin-wire, was not as uniform as thought with the previous approach.

The following step was to apply this code to the ADAMANT outcomes determined by Melazzi and Lancellotti[24] for three antenna configurations: Single-Loop, NAgoya III and Fractional Helix.

Successively, a comparison has been made between the spectral functions obtained by our approach and the ones used by Chen[12] for the HELIC code.

For the Single-Loop, the HELIC code elaborated a constant value, whilst the spectral function of the current density of 3D antenna is a $sinc$ function modulated by a cosine.

Regarding the Nagoya III type, the spectral function in Chen's[12] case has a sin form, whilst, with the new algorithm, we obtained a $sinc$ function modulated by a sine.

Then, with the Fractional Helix antenna, we observed that the two functions were really similar, although the one derived with the new code is subjected to a greater decay respect to the Chen's[12] one.

Finally, despite the non perfect uniformity observed in the antenna current density distribution, the azimuthal modes excited are the same as the ones considered for the HELIC simulations.

As it has been done by D. Melazzi and V. Lancellotti[24] for the antenna input impedance, an investigation about the influence of the discharge parameters on the spectral functions has been carried on. The electron temperature and the background pressure do not make the antenna current density spectrum change, as was noticed for the antenna input impedance. About the magnetic field intensity, there are little variations only for high plasma density values in the order of $2-3\%$. Concerning the plasma density, the spectral intensity of the function rises as n increases, and this behaviour is emphasized for high values of the magnetic field intensity; the variations, though, go from 2% to 7%. These results are a consequence of the little fluctuations registered in the current density distribution on the antenna surface through ADAMANT.

At this point, it was possible to use the antenna current density spectral functions as inputs for the SPIREs code in order to obtain the radial power profile in the plasma cylinder: this analysis regards only the contribution for a particular set of $m-k_z$ pairs and not the contribution of the global spectrum.

The aim was to understand the correlations between the spectrum intensity, the azimuthal and axial modes and the radial power profiles within the operative interval in which the waves propagate: the limits are imposed by two axial wave numbers, $k_{z\,min}$ and $k_{z\,max}$ defined by Eq.(5.3) and Eq.(5.4).

The first consideration confirms that the major contributes can be obtained with the $m = 0$ mode: the radial power profiles for the Single-Loop subtend areas which outmatch those subtended by the curves related for the other antennas, which excite modes different from zero.

Secondly, observing the results regarding the Nagoya III and the Fractional Helix, the curves for $m = \pm 3$ are identical, whilst for $m = \pm 1$ this does not happen: in both cases, the most performing curves are those related to $m = +1$. A possible explanation could be the phase of the values considered since the spectrum is a complex function.

Moreover, it was observed that the profiles related $k_z \approx k_{z\,min}$ are really flat; on the contrary, for mid-k_z values, the profiles subtend always a great area even though with low spectral values.

Finally, for all the antenna configurations, the profiles decay rapidly within the $3-5\%$ of the plasma cylinder radius, a sign that TG waves are the responsible for the deposition power for these cases.

Thanks to these considerations, it was possible to think about an ideal spectral function in order to optimize the radial power profiles: two antenna configurations are proposed for this purpose and they have been analysed first with ADAMANT and then with SPIREs.

The first one is similar to a Nagoya III type, but the voltage gap is applied to a half-loop located in the middle of the antenna and which is linked to the two edge loops by means of straight axial connections. The aim was to obtain an antenna current density distribution on the two edge loops similar to the one registered for the Fractional Helix, deleting the shift in the spectral function caused by the helical links and maximizing in this way the values in the operative interval.

With ADAMANT, the power deposited into the plasma has been determined for a range of discharge parameters, showing that the performances are better than the ones related to the other antennas, although it cannot reach the peak values noted for the Nagoya III type. The spectral function of this configuration current density has contributions for both $m = 0$ and $m = \pm 1$, which can explain the high performances: the problem is that the peak values of the spectral function are not inside the operative interval.

The other configuration is composed of two loops placed along the z-axis and excited with a different phase β, for a total of 5 examples: β is an important factor since can shift the spectral function of the current density along the k_z axis, maximizing the spectral intensities involved in the power absorption.

The power deposited into the plasma with $\beta = 0°$ and $\beta = 45°$ is higher compared to the other antennas in the low plasma density range, whilst the same consideration can be done for the remaining values of the phase in the high plasma density range.

Although the antenna current density distribution determined with ADAMANT is different for every phase considered, the intensity of the spectrum is the same; instead, the effect of the phase is a shift along k_z as predicted.

The best case is for $\beta = 180°$ and the spectrum highlights how the intensity values, selected as inputs for the SPIREs, increase as k_z grows: this behaviour was possible thanks precisely to the shift caused by the phase imposed between the excitation of the loops.

In closing, since the phase can be varied during a mission, it is possible to adapt the double loop configuration to the power needed or to the plasma density range interested, making this device really versatile.

Part I

APPENDIX

A

CODE BENCHMARK

There is the necessity to test the code with a known reference example in order to prove that it is reliable: in order to do that we impose a constant current density on the antenna surface.

First, it is good to remember that $\vec{J} = \sum_n \vec{f}_n(\vec{r})\ I_n$ with $r \in S$, the surface delimited by the couple of triangles.

Taking the dot product with an m^{th} RWG function for both sides of the equation and integrating on the surface, the following expression is determined:

$$\underbrace{\int_{S_m} dS \vec{f}_m(\vec{r}) \cdot \vec{J}}_{[n \times 1]} = \sum_n \underbrace{\int_{S_m} dS \vec{f}_n(\vec{r}) \cdot \vec{f}_m(\vec{r})\, I_n}_{G_{mn}} \tag{A.1}$$

where G_{mn} is the Gram matrix, which is derivable by a sub-routine already available. The current coefficients I_n are the unknown variables, whilst the $[n \times 1]$ vector $\vec{H}$ is more complexed to be determined.

The first hypothesis is that $\vec{J}$ is parallel to $\vec{\tau}$ for every surface S_m considered and its module must be equal to $1\frac{A}{m}$. All the subsequent passages concern only the surface of the positive triangle T^+ in order to lighten the reading: despite this, the relative algebra for T^- is the same but with the opposite sign.

Recalling the definition of an RWG function in [18] and looking at Fig.A.1, the first step is as follows:

$$\begin{aligned} H_{m_+} &= \int_{S^+} dS \vec{f}_m(\vec{r}) \cdot \hat{\tau} = \hat{\tau} \cdot \int_{T^+} dS \vec{f}_m(\vec{r}) = \\ &= \hat{\tau} \int_{T^+} dS\ \frac{l_{3m}}{2A^+}\ (\vec{r} - \vec{r}_3^+) \end{aligned} \tag{A.2}$$

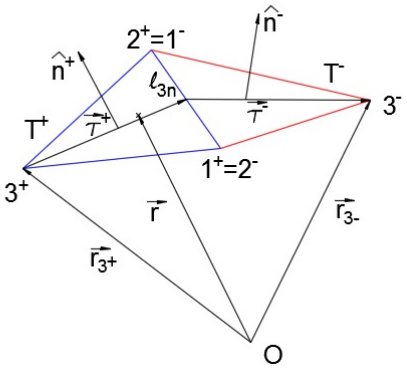

Figure A.1: Nomenclature on a couple of triangles for RWG definition

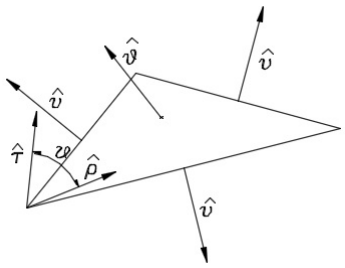

Figure A.2: $\hat{\rho}\cdot\hat{\tau}$ and Green theorem application: $\hat{\rho}$ and $\hat{\tau}$ are on the same plane of the triangle, whose perpendicular versor is $\hat{\theta}$.

in which a new variable $\vec{\rho} = (\vec{r} - \vec{r}_3^{+})$ can be introduced.

Excluding the constant terms which don't influence the integration, only $\int_{T^+} dS\ \ \vec{\rho}\cdot\hat{\tau}$ needs to be solved. The aim is to find a function $\vec{F}$ such that $\rho\ \hat{\rho}\cdot\hat{\tau} = \vec{\nabla}_t\cdot\vec{F}$, with $\hat{\rho}$ unit vector of $\vec{\rho}$ and $\vec{\nabla}_t$ is the vector differential operator.

Knowing that $\vec{\nabla}_t\cdot\vec{F} = \frac{1}{\rho}\frac{\delta}{\delta\rho}(\rho F_\rho) + \frac{1}{\rho}\frac{\delta F_\theta}{\delta\theta} + \frac{\delta F_z}{\delta z}$ and that $F_\theta = F_z = 0$, it is possible to affirm that $F_\rho = \frac{\rho^2}{3}$ and, hence, that:

$$\begin{aligned}\rho\ \hat{\rho}\cdot\hat{\tau} =& \vec{\nabla}_t\cdot(\frac{\rho\vec{\rho}}{3}\hat{\rho}\cdot\hat{\tau}) = \\ =& \vec{\nabla}_t\cdot(\frac{\rho\vec{\rho}}{3}\hat{\rho}\cdot\hat{\tau}) - \frac{\rho\vec{\rho}}{3}\cdot\vec{\nabla}_t(\hat{\rho}\cdot\hat{\tau})\end{aligned} \tag{A.3}$$

From Fig.A.2 it is clear that $\hat{\rho}\cdot\hat{\tau} = \cos\theta$ and, all in all, that $\vec{\nabla}_t\cdot(\hat{\rho}\cdot\hat{\tau} = -\hat{\theta}\sin\theta$. In this way, the last part of Eq.(A.3) is null, since $\vec{\rho}\cdot\hat{\theta} = 0$.

Now, the Green theorem can be applied:

$$\begin{aligned}\int_{T^+}\hat{\rho}\cdot\hat{\tau}\ dS =& \int_{T^+}\vec{\nabla}_t\cdot(\frac{\vec{\rho}\ \vec{\rho}\cdot\hat{\tau}}{3})dS = \\ =& \oint_{\delta T^+} ds\hat{\nu}\vec{\rho}\frac{\rho\cdot\hat{\tau}}{3}\end{aligned} \tag{A.4}$$

and, since the only component different to zero is along l_3, the final form is:

$$\int_{T^+}\hat{\rho}\cdot\hat{\tau}\ dS = \int_{\delta T_3^+} ds\ h\frac{\vec{\rho}}{3}\cdot\hat{\tau} \tag{A.5}$$

where h is the height of the triangle, as a result of the dot product between ρ and ν.

Looking at Fig.A.3, recalling Eq.(A.2) and knowing that $h = \frac{2A}{l_3}$, it is simple to understand the following development:

$$\vec{\rho}\cdot\hat{\tau} = (\vec{\rho}_{13} + s\hat{s})\cdot\hat{\tau} = \vec{\rho}_{13}\cdot\hat{\tau} + s\ \hat{s}\cdot\hat{\tau} \tag{A.6}$$

$$\int_{T^+}\hat{\rho}\cdot\hat{\tau}\ dS = \frac{h}{3}[\vec{\rho}_{13}\cdot\hat{\tau}l_3 + \frac{l_3^2}{2}\ \hat{s}\cdot\hat{\tau}] \tag{A.7}$$

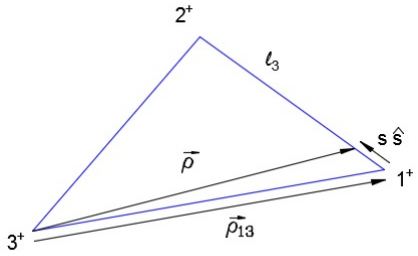

Figure A.3: Integration reference system: $\vec{\rho}$ can be seen as a vector sum of $\vec{\rho}_{13}$ and $s\hat{s}$, the variable which must be integrated.

$$H_{m_+} = \frac{l_3 \hat{\tau}}{3}[\vec{\rho}_{13} + \vec{\rho}_{21}] \tag{A.8}$$

The whole m^{th} component of the vector $\vec{H}$ must have also the part relative to the negative triangle; therefore, the final expression is:

$$\vec{H}_m = \frac{l_3 \hat{\tau}}{3}[\vec{\rho}_{1^+3^+} + \frac{\vec{\rho}_{2^+1^+}}{2} - (\vec{\rho}_{1^-3^-} + \frac{\vec{\rho}_{2^-1^-}}{2})] \tag{A.9}$$

As it was already said before, the aim is to find the density current coefficients I_n in the subsequent problem:

$$\begin{Bmatrix} H_1 \\ \vdots \\ H_N \end{Bmatrix} = \begin{pmatrix} \\ G \\ \\ \end{pmatrix} \begin{Bmatrix} I_1 \\ \vdots \\ I_N \end{Bmatrix} \tag{A.10}$$

Once G and H are defined, it is possible to determine I as:

$$I = G^{-1}\, H \tag{A.11}$$

B

k_z OPERATIVE INTERVAL DETERMINATION

The following proceeding is taken from a work done by Chen[11]. The first assumption is that the electromagnetic fields are assumed to vary as $e^{i(m\theta + k_z z + wt)}$, where m and k_z are the azimuthal and axial wave-numbers and w is the operative frequency.

The problem is studied through the Maxwell's equations

$$\vec{\nabla} \cdot \vec{B} = 0 \tag{B.12}$$

$$\vec{\nabla} \times \vec{E} = iw\vec{B} \tag{B.13}$$

$$\vec{\nabla} \times \vec{B} = \mu_0(\vec{j} - iw\epsilon_0\vec{E}) = -iw\epsilon_0\mu_0\vec{\epsilon} \cdot \vec{E} \tag{B.14}$$

and the electron fluid equation of motion

$$-iwm_e\vec{v} = -e(\vec{E} + \vec{v} \times \vec{B}_0) - m_e\nu\vec{v} \tag{B.15}$$

where:

- $\vec{E}$ and $\vec{B}$ are the electric and magnetic field vectors;
- ϵ_0 and μ_0 are the permittivity and permeability of free space;
- $\vec{\epsilon}$ is the electromagnetic tensor;
- e, m_e and $\vec{v}$ are, respectively, the charge, mass and velocity of the electron;
- ν is the collision rate which contains all the dissipation mechanisms;
- $\vec{B}_0 = B_0\hat{z}$ is the dc magnetic field aligned with the z axis;
- $\vec{j}$ is the plasma current.

It must be remembered that in Eq.(B.15), the magnetic viscosity and pressure terms are omitted. In addition, the ion motions are neglected, that is the plasma current can be considered as $\vec{j} = -en_0\vec{v}$, with n_0 the electron density.

With the following definitions

$$w_c = \frac{eB_0}{m_e}, \quad \delta_r = \frac{w}{w_c}, \quad \delta = \frac{w + i\nu}{w_c} \tag{B.16}$$

$$w_p^2 = \frac{ne^2}{\epsilon_0 m_e}, \quad k_s = \frac{w_p}{c}, \quad \delta k_s^2 = \frac{wn_0\mu_0 e}{B_0} = k_w^2 \tag{B.17}$$

Eq.(B.15) can be expressed as:

$$\vec{E} = -\frac{B_0}{en_0}(i\delta\vec{j} + \hat{z} \times \vec{j}). \tag{B.18}$$

Neglecting the displacement current, that is Eq.(B.14) can be written as $\vec{\nabla} \times \vec{B} = \mu_0 \vec{j}$, together with the previous definitions and using Eq.(B.18), it is possible to define Eq.(B.13) as

$$\delta \vec{\nabla} \times \vec{\nabla} \times \vec{B} - k_z \vec{\nabla} \times \vec{B} + k_w^2 \vec{B} = 0. \tag{B.19}$$

Eq.(B.19) can be factored into[25]

$$(\beta_1 - \vec{\nabla} \times)(\beta_2 - \vec{\nabla} \times)\vec{B} = 0 \tag{B.20}$$

with β_1 and β_2 the roots of

$$\delta\beta^2 - k_z\beta + k_w^2 = 0. \tag{B.21}$$

For $\delta k_w^2 \ll k_z^2$ and not neglecting the electron mass, it is possible to define the two roots of Eq.B.21 as:

$$\beta_1 \approx \frac{k_w^2}{k_z} \quad \beta_2 \approx \frac{k}{\delta}. \tag{B.22}$$

These two values correspond to the two particular waves mode of excitation, namely β_1 for the H wave and β_2 for the TG wave.

Aside for this, it is possible to rearrange Eq.(B.21) as $k_z = \frac{\delta}{\beta}(\beta^2 + k_s^2)$; deriving it, the maximum and minimum value of the axial wave number k_z are determined:

$$k_{z\,min} = 2\delta k_s \tag{B.23}$$

$$k_{z\,max} = \sqrt{\frac{\delta}{\delta - 1}} k_s. \tag{B.24}$$

These two variable define the interval in which the propagating waves are damped by the plasma and, consequently, they are important in the study of the radial power deposition since the antenna current density spectra is defined by the combination of m and k_z modes.

BIBLIOGRAPHY

[1] J. Navarro-Cavallè, E. Ahedo, M. Merino, V. Gòmez, M. Ruiz, J. A. G. del Amo, "Helicon Plasma Thrusters: prototypes and advances on modeling", *International Electric Propulsion Conference*, The George Washington University, Washington, D.C., USA, October 2013

[2] A. Petro, "VASIMR Plasma Rocket Technology", *Advanced Space Propulsion Laboratory*,NASA JSC Houston, Texas, May 2002

[3] D. Pavarin, F. Ferri, M. Manente, D. Curreli, Y. Guclu, D. Melazzi, "Helicon Plasma Hydrazine: COmbined Micro project overview and development status", *Proc. Space Propulsion Conf.*, San Sebastian, Spain, May 2010

[4] IEPC-2013-153 Presented at the 33rd F. Trezzolani, A. Lucca Fabris, D. Pavarin, A. Selmo, "Low Power Radio-Frequency Plasma Thruster Development and Testing", in 33^{rd} *International Electric Propulsion Conference*, The George Washington University, USA, October 2013

[5] D. Pavarin, F. Ferri, M. Manente, A. L. Fabris, F. Trezzolani, M. Faenza, L. Tasinato, "Development of plasma codes for the design of mini-Helicon thrusters", 32^{nd} *International Electric Propulsion Conference*, Wiesband, Germany, September 2011

[6] R. W. Boswell, "Very efficient plasma generation by Whistler waves near the lower hybrid frequency Plasma, *Plasma Physics and Controlled Fusion*, Vol. 26, No. 10, pp. 1147-1162, 1984

[7] F. F. Chen, I. D. Sudit,M. Light, "Downstream physics of the helicon discharge", *Plasma Sources Science Technology*, Vol. 5, pp.173–180, 1996

[8] D. Arnush, "The role of Trivelpiece-Gould waves in antenna coupling to helicon waves", *Physics of Plasmas*, Vol. 7, No. 7, pp. 3042-3050, 2000

[9] F. F. Chen, "Helicon Plasma Sources", in O.A. Popov (ed.), *High Density Plasma Sources* (1996), Science Direct:1-75

[10] Y. Mouzouris, J. E. Scharer, "Modeling of profile effects for inductive helicon plasma sources", *IEEE Transactions on Plasma Science*, Vol.24, No.1, 1996

[11] D. Arnush, F. F. Chen, "Generalized theory of helicon waves. I. Normal modes", *Physics of Plasmas*, Vol.4, No. 9, 1997

[12] D. Arnusha, F. F. Chen, "Generalized theory of helicon waves. II. Excitation and absorption", *Physics of Plasmas*, Vol.5, No. 5, 1998

[13] D. Melazzi, D.Curreli, M.Manente, J. Carlsson, D. Pavarin, "SPIREs: A Finite-Difference Frequency-Domain electromagnetic solver for inhomogeneous magnetized plasma cylinders", *Computer Physics Communications*, Vol.183, pp.1182–1191, 2012

[14] B. D. McVey, "ANTENA user guide", *Plasma Fusion Controlled*, MIT, Rep. PFC/RR-84-13, 1984

[15] B. D. McVey, "ICRF antenna coupling theory for a cylindrically stratified plasma", *Plasma Fusion Controlled*, MIT, Rep.PFC/RR-84-12, 1984

[16] T. H. Stix, "Waves in Plasmas", New York, American Institute Physics, 1992

[17] V. Lancellotti, D. Milanesio, R. Maggiora, G. Vecchi and V. Kyrytsya, "TOPICA: an accurate and efficient numerical tool for analysis and design of ICRF antennas", *Institute of Physics Publishing and International Atomic Energy Agency*, Nuclear Fusion, Vol.46 , pp.476–499, 2006

[18] D. Melazzi V. Lancellotti, "ADAMANT: A surface and volume integral-equation solver for the analysis and design of helicon plasma sources", *Computer Physics Communications*, Vol.185, pp.1914–1925, 2014

[19] A. F. Peterson, S. L. Ray, R. Mittra, "Computational Methods for Electromagnetics", Piscataway, IEEE Press, 1998

[20] S. M. Rao, D. R. Wilton, A. W. Glisson, "Electromagnetic scattering by surfaces of arbitrary shape", *IEEE Transactions Antennas and Propagation*, Vol.30, No.3, pp.409–418, 1982

[21] D. H. Schaubert, D. R. Wilton, A. W. Glisson, "A tetrahedral modeling method for electromagnetic scattering by arbitrarily shaped inhomogeneous dielectric bodies", *IEEE Transactions Antennas and Propagation*, Vol.32, No.1, pp.77–85, 1984

[22] R. F. Harrington, "Field Computation by Moment Methods", New York, MacMillan, 1968

[23] G. Kobidze, B. Shanker, "Integral equation based analysis of scattering from 3-D inhomogeneous anisotropic bodies", *IEEE Transactions Antennas and Propagation*, Vol.52, No.10, pp.2650–2658, 2004

[24] D. Melazzi, V. Lancellotti, "A comparative study of radiofrequency antennas for Helicon plasma sources", *Plasma Sources Science Technology*, Vol.24, 2015

[25] J.P. Klozenberg, B. McNamara and P.C. Thonemann, *J. Fluid Mech.*, Vol.21, No.545, 1965